

NORTHWESTERN UNIVERSITY

Multi-scale Functional Structure Engineering with Soft Materials

A DISSERTATION

SUBMITTED TO THE GRADUATE SCHOOL  
IN PARTIAL FULFILLMENT OF THE REQUIREMENTS

for the degree

DOCTOR OF PHILOSOPHY

Field of Chemistry

By

EunBi Oh

EVANSTON, ILLINOIS

September 2021

© Copyright by EunBi Oh 2021

All Rights Reserved

## ABSTRACT

### Multi-scale Functional Structure Engineering with Soft Materials

EunBi Oh

Soft functional materials are fundamentally interesting from a chemistry standpoint and have exciting applications in robotics, chemical and biomolecule sensing, and biomedical engineering. In addition, soft materials are also useful in lithography, particularly cantilever-free scanning probe lithography (CFSPL). Because of their low modulus, biocompatibility, stimuli responsiveness, malleability, and other characteristics, soft materials can be used to enhance the capabilities of CFSPL, which has been primarily used to synthesize inorganic and hard materials thus far. Indeed, soft materials-enabled CFSPL approaches can be used to pattern soft substrates and organic structures, including biological ones useful for studying bio-relevant surface cellular interactions.

Three key factors must be considered in performing CFSPL techniques: the pen array that delivers the ink, the types of substrates that are being patterned, and the chemistry of the ink material. Herein, findings are presented that advance aspects of each of these factors. First, a new CFSPL technique termed electrochemical polymer pen lithography is introduced, where the pen arrays are comprised of hydrogel materials. Indeed, more than 10,000 hydrogel pen tips served as the electrolyte, allowing high-throughput localized electrodeposition of electroactive materials (e.g., metal ions) with precise spatial control. By taking advantage of the hydrogel's ability to absorb large volumes of aqueous solutions and facilitate ion diffusion, compositional gradients of bi-metallic features were generated across a single substrate. Such a technique could be used in high-throughput combinatorial screening to identify ideal catalysts for energy applications. Second,

photo-responsive hydrogels were used as substrates to generate patterns of well-defined soft and stiff domains (as dictated by the local hydrogel chemistry) with sizes ranging from the sub-cellular to cell scale. These patterns were used to examine and program cellular behavior. In particular, the soft domains dictated the formation of focal adhesions and were specifically designed to be commensurate with a target cell size to maximize cell migration speed (by as much as two-fold compared to the unpatterned surfaces). The relative contribution of topography and mechanics on cell migration was also examined; it was found that cells respond to stiffness heterogeneity more than topographical variations encoded by surface patterns, contributing to our understanding of how cells differentiate physical cues in heterogeneous landscapes. Finally, small organic molecules or monomers were used as ink materials in conjunction with the polymer pen lithography (PPL) platform to synthesize covalent organic frameworks (COFs). Using this approach, the nucleation and growth mechanisms of imine-linked COFs were probed. The evaporation rate of the patterned nanoreactors was identified as the critical determining factor in synthesizing single crystal COFs, which have enhanced electronic properties compared with conventionally formed powders or amorphous aggregates. In addition, this new one-step synthetic approach does not require harsh reaction conditions, long reaction times, and multi-step processes, as do many other current synthetic methods, and enables the site-selective growth of COF crystallites with tunable sizes and morphologies that are important in the context of optoelectronic devices.

---

Thesis Advisor: Prof. Chad A. Mirkin

*EunBi Oh*

---

EunBi Oh

## ACKNOWLEDGEMENTS

In anyone's life, there are periods of adversity and unknowns that often lead to a hardship. It is people, however, who can turn these unexpected and surprising moments into exciting times. When I think back to when I began my Ph.D. program, I was clueless. Without amazing and incredible peers, friends, collaborators, and colleagues around me, this dissertation would not have been possible. Therefore, I am very honored to acknowledge these individuals who have been through this wonderful journey with me and provided endless support, care, inspiration, and encouragement while I became the researcher I am today.

First and foremost, I would like to express my sincere gratitude to my advisor, Prof. Chad A. Mirkin. Thank you so much for giving me this awesome opportunity to explore science with the exceptional researchers and fully reach my potential. Our discussions have always challenged me to think creatively and critically. Your incredible guidance, encouragement, and patience have allowed me to continuously push myself and grow as a better scientist. I will always remember my time here in your group with affection and appreciation. In addition, I thank my committee members, Prof. Milan Mrksich, Prof. Emily A. Weiss, and Prof. Nathan C. Gianneschi, all of whom provided insightful suggestions and critical feedback to my work and helped me perform scientifically meaningful research. Thank you for being on my committee. I am also truly grateful for the continued help and support from my undergraduate advisor, Prof. James F. Cahoon who provided me an opportunity to do research in the first place.

My dissertation would not have been possible without my collaborators, especially, Dr. Rustin Golnabi, Prof. Brian Meckes, and Donghoon Shin. It has been my greatest pleasure to collaborate and work with you all. I have learned so much and always enjoyed brainstorming the

next steps and discussing scientific problems. I also want to thank one of my mentors, Dr. Maria D. Cabezas who first introduced me to the world of patterning and taught me all the skills that I have used to complete my thesis. I also thank Dr. David A. Walker, another brilliant mentor who helped me immensely, from my qualifying exam document editing to weekly one-on-one meetings where he provided feedback on my progress and discussed project ideas with me. Finally, to my hard-working and intelligent undergraduate mentee, Jinyoung Chang—I greatly appreciate your help and effort; without you, my cell project would not have progressed as smoothly as it did.

During my time at Northwestern, I was tremendously fortunate to have met phenomenal colleagues and friends, who always encouraged me to move forward. From the Mirkin group, I thank Liban Jibril, Namrata Ramani, Prof. Soyoung (Eileen) Seo, Dr. Seungkyu Lee, Jungsoo Park, Dr. Taegon Oh, Prof. Sarah S. Park, and Dr. Youngeun Kim. It has been a privilege to have met and become friends with you all. You made my time here both enjoyable and unforgettable. Thank you for making the lab a fun place to work. Furthermore, without the help of the excellent staff members in the Mirkin lab, Dr. Sara Rupich, Dr. Sarah H. Petrosko, Pam Watson, Elizabeth Forest, and Dr. Tanushri Sengupta, I would not have been able to complete and present work that I have accomplished during my Ph.D. To my best friend outside of my research lab, Dr. Priscilla Choo: thank you so much for bearing with me all these years, listening to my complaints, and letting me vent. To Prof. Woongkyu Lee, Sunghwan Park, Dr. Dongjoon Rhee, Dr. Woojung Ji, Dr. Yongjin Shin, Dr. Jieun J. Park, Tae-Ung Choi, Bowon Kim, Taeyoon Kim, Jinhyeong Bae, JunHee Lee, Boyoung Kang, Prof. Eojin Han, Dr. Gyeongwon K. Kang, Wonmin Choi, and HanByul Chang: I will always cherish the amazing memories of coffee breaks, lunch times, discussions, social events,

outings, and everything that we have done together. Thank you for supporting me throughout my time at Northwestern.

It is impossible to conclude these acknowledgements without thanks to my family and friends outside of Northwestern. Foremost, I cannot express how thankful I am to my husband (soon to be a Dr.), Wooje Chang. Meeting you was the greatest thing that ever happened to me. You are my best friend, biggest cheerleader, inspiration, dream, sunshine, life, world, and everything. I truly admire your passion towards science, and you always motivate me to become a better person and scientist. I especially thank my dad, mom, and sister: without your endless support and love, I would not have been able to finish my Ph.D. Thank you so much for believing in me, listening to my nonsense, and giving me everything. I love you all so much. Thank you to all the other family members including my beloved aunt, EunIm Jang, and families-in-law. To my best friends from my undergraduate years, Meena Park, Eunyoung Oh, Hannah Kim, and Hannah Choi—thank you for your love, friendship, inspiration, and encouragement.

Last, but not least, I want to thank God for giving me a chance to be at Northwestern and for everything.

-EunBi

July 2021

## LIST OF ABBREVIATIONS

AFM	Atomic force microscopy
BPL	Beam pen lithography
CFSP	Cantilever free scanning probe lithography
COF	Covalent organic frameworks
CV	Cyclic voltammetry
DMD	Digital micromirror device
DPN	Dip pen nanolithography
ECM	Extracellular matrix
EDS	Energy-dispersive x-ray spectroscopy
ePPL	Electrochemical polymer pen lithography
hMSCs	Human mesenchymal stem cells
ITO	Indium tin oxide
MHA	16-mercaptohexadecanoic acid
PDMS	Polydimethylsiloxane
PEGA	Polyethylene glycol monoacrylate
PEGdiPDA	Polyethylene glycol photodegradable diacrylate
PPL	Polymer pen lithography
RIE	Reacting ion etching
SEM	Scanning electron microscopy
XPS	X-ray photoelectron spectroscopy

## **DEDICATIONS**

To my family, friends, and my love, Woo Je Chang who supported and believed in me  
throughout this journey

## TABLE OF CONTENTS

ABSTRACT.....	3
ACKNOWLEDGEMENTS.....	5
LIST OF ABBREVIATIONS.....	8
DEDICATIONS.....	9
TABLE OF CONTENTS.....	10
LIST OF FIGURES .....	13
LIST OF TABLES .....	19
<b>Chapter 1 Introduction.....</b>	<b>20</b>
1.1. Background.....	21
1.2. Cantilever-Free Scanning Probe Lithography .....	22
1.2.1. Polymer Pen Lithography .....	22
1.2.2. Beam Pen Lithography .....	27
1.3. Thesis Overview and Objectives .....	30
<b>Chapter 2 Electrochemical Polymer Pen Lithography .....</b>	<b>32</b>
2.1. Introduction.....	33
2.2. Results and Discussions.....	35
2.2.1. Electrochemical Pen Arrays.....	35
2.2.2. Single Metal Patterning.....	37
2.2.3. Multimetallic Patterning .....	41
2.2.4. Feature Size Control and 3-Dimensional Printing .....	45
2.3. Experimental Details.....	48
2.3.1. Preparation of Metal Deposition Solutions.....	48
2.3.2. Fabrication of Pen Array Masters .....	49
2.3.3. Preparation of Polyacrylamide Hydrogel Pen Arrays.....	49
2.3.4. Assembly of a Three Electrode Cell .....	50
2.3.5. Patterning Procedure .....	50
2.3.6. Characterization of Patterns .....	51
2.4. Conclusion .....	52

<b>Chapter 3 Micropatterned Hydrogels for Controlled Cancer Cell Migration .....</b>	<b>53</b>
3.1. Introduction.....	54
3.2. Fabrication and Characterization of Patterned Hydrogel Matrices.....	56
3.3. Cellular Migratory Behavior on the Patterned Hydrogels .....	60
3.4. Deconvolution of Confinement and Stiffness.....	66
3.5. Cell Alignment Control <i>via</i> Stiffness Heterogeneity .....	69
3.6. Methods.....	73
3.6.1. Photodegradable monomer synthesis.....	73
3.6.2. Hydrogel film formation.....	73
3.6.3. Pattern design and generation .....	74
3.6.4. Pattern imaging and stiffness characterization .....	74
3.6.5. Cell culture and seeding.....	75
3.6.6. Immunofluorescence imaging.....	75
3.6.7. Statistical Analysis.....	76
3.7. Summary and Outlook .....	76
<b>Chapter 4 Nanoscale Patterning to Probe and Control Cell-Matrix Interactions.....</b>	<b>78</b>
4.1. Introduction.....	79
4.2. Using Beam Pen Lithography to Control Physical Cues .....	82
4.3. Spatially Encoded Chemical Cues <i>via</i> Polymer Pen Lithography.....	86
4.3.1. Patterns of Varying Sizes and Dimensions.....	86
4.3.2. Patterns with Compositional Gradients .....	89
4.4. Experimental Details.....	93
4.4.1. Fabrication of Beam Pen Arrays.....	93
4.4.2. Fabrication of Polymer Pen Arrays.....	93
4.5. Summary and Outlook .....	94
<b>Chapter 5 Tip-assisted Synthesis of Covalent Organic Frameworks .....</b>	<b>95</b>
5.1. Introduction.....	96
5.2. Results and Discussion .....	97
5.3. Summary and Outlook .....	101
<b>Chapter 6 Conclusions and Outlook .....</b>	<b>102</b>
6.1. Summary and Future Opportunities.....	103
REFERENCES .....	105

CURRICULUM VITAE..... 116

ORIGINAL RESEARCH PROPOSAL..... 119

## LIST OF FIGURES

- Figure 1.1.** Illustration of PPL platform. The pen array is attached to the piezo scanner, enabling the pens to print arbitrary features with control over all x, y, and z directions. When pens are in contact with the substrate, the ink is transferred and form a meniscus on the surface. Figure adapted from ref. 7. Reprinted with permission from AAAS. .... 23
- Figure 1.2.** Optical images of logos printed with PPL. (a) ~15, 000 duplicates of the Beijing Olympic logo and (b) identical replicas of the WIPO logos on Au-coated substrate. Panel **a** adapted from ref. 7. Reprinted with permission from AAAS. .... 25
- Figure 1.3.** Pattern designs and fluorescence micrographs of hMSCs' actin cytoskeleton on the respective pattern. Reprinted with permission from Ref. 10. Copyright (2019) American Chemical Society..... 26
- Figure 1.4.** a) Confocal images of two different polymer domes containing fluorophores patterned with compositional and size gradients using a spray-coated PPL array. Average fluorescence intensity was measured across the substrate and plotted against (b) composition and (c) size. Reprinted with permission from ref. 11; Copyright (2019) National Academy of Sciences. .... 27
- Figure 1.5.** a) Schematic diagram of BPL, illustrating the patterning process where light is going through a transparent PDMS tip and exposes a surface of the substrate coated with light-responsive photoresist. b) A Chicago skyline patterned with BPL. Figure adapted from ref. 13. Reprinted with permission from AAAS. .... 28
- Figure 1.6.** SEM images of beam pen arrays with apertures of varying sizes. Deposited gold at the tip of the pen array is chemically etched to allow light to pass through and delivered onto the surface of the substrate..... 29
- Figure 1.7.** a) Gold serpentine resistors patterned in centimeter-scale *via* BPL using 3 to 15 actuated pen tips. Scale bar is 100  $\mu\text{m}$ . b) The resistance was measured and plotted against the resistor length. Reprinted with permission from ref. 14; Copyright (2013), Nature Publishing Group. .... 29
- Figure 2.1.** Schematic illustration of electrochemical polymer pen lithography. .... 34
- Figure 2.2.** Experimental setup of ePPL. (a) Schematic of a three-electrode cell designed to hold the hydrogel array, electrolyte, and reference and counter electrodes in place during patterning. (b) Optical image of fabricated polyacrylamide hydrogel pen arrays, which were prepared by curing the hydrogel within a silicon master (scale bar = 30  $\mu\text{m}$ ). Images on the right show a pen array during the patterning process, highlighting how contact was determined: pens (top) out-of-contact and (bottom) in-contact with the substrate (working electrode) (scale bars = 15  $\mu\text{m}$ ) (c) Photograph of the experimental setup in a Park AFM, showing the cell, electrodes, electrical leads, and optical microscope used for leveling. Inset shows an image of the hydrogel pen array mounted within the cell..... 36

**Figure 2.3.** CV scans for a Ni-embedded hydrogel 3-electrode cell at three different scan rates, indicating both reduction and oxidation potential peaks. .... 37

**Figure 2.4.** Patterning capabilities of ePPL. Optical micrographs of patterns of (a) Ni on a Au substrate (scale bar = 100  $\mu\text{m}$ ), (b) Ag on an ITO substrate (scale bar = 20  $\mu\text{m}$ ), and (c) Pt on a Au substrate (scale bar = 100  $\mu\text{m}$ ). The Pt pattern consists of an array of 13 dots arranged as the letter 'N' at each pen location. AFM images of (d) a single 'N' (scale bar = 10  $\mu\text{m}$ ) and (e) a single Pt particle (scale bar = 500 nm). (f) The associated line scan of one of the particles in panel d. .... 38

**Figure 2.5.** Optical images of a substrate with Ni features before and after extensive rinsing indicating the presence of reduced metal. A Au-coated Si wafer was patterned with an array of 3 Ni features from each tip (a), washed thoroughly with water (b), and then sonicated for 30 s in water (c). While the features faded after agitation, this experiment shows that the patterned features are reduced metal on the substrate and not salt residue. Scale bars = 30  $\mu\text{m}$ . .... 39

**Figure 2.6.** Control patterning experiment shows that an applied voltage is needed for metal deposition to occur. A Au-coated Si wafer was scratched with a cross and imaged before (a) and after (b) typical Ni patterning with 0 V applied. No patterned features are observed. Scale bars = 50  $\mu\text{m}$ . .... 39

**Figure 2.7.** XPS patterns of the patterned samples confirm the presence of metal on the respective substrates. (a) Ni features on a Au-coated Si wafer. The peaks at 856 eV and 873 eV (left) are expected Ni 2p peaks. Au 4f peaks are observed at 84 eV and 87.7 eV (right). (b) The peak at 73 eV (left) indicates Pt on Au-coated Si substrate with Au 4f peak at 84 eV (right). (c) The presence of the Ag is confirmed by the peaks at 367 eV and 373.6 eV (left) and the peaks at 486 eV and 494.5 eV (right) are assigned to Sn 3d from the indium tin oxide (ITO) coated glass slide. The main peaks in the deposited features are all oxides due to rapid oxidation upon exposure to ambient conditions. .... 40

**Figure 2.8.** Deposition of Ni-Co alloys. (a) Optical micrograph of a large-area pattern of >10  $\mu\text{m}$  Ni-Co features. The large feature size enables accurate elemental characterization. Inset shows a single feature. (b) XPS characterization of these patterns indicates that both the Ni and Co are present mainly as oxides. Auger peaks have been subtracted for clarity. .... 42

**Figure 2.9.** Optical micrograph of Ni-Co particles patterned on a Au substrate. Scale bar = 50  $\mu\text{m}$ . .... 42

**Figure 2.10.** (a) AFM height profile of a large Ni-Co feature, and (b) AFM line scan across the large feature in (a), location indicated by dashed line. Scale bar = 3  $\mu\text{m}$ . .... 43

**Figure 2.11.** EDS characterization of a Ni-Co feature indicates the presence of both Ni and Co in the deposited region. Ni-Co was patterned on a Au-coated SiO<sub>2</sub> wafer with a chromium adhesion layer. Corresponding metal peaks are labeled. Scale bar = 5  $\mu\text{m}$ . .... 44

**Figure 2.12.** Scanning electron micrographs of patterned Pt features on Au-coated Si wafer, highlighting the high-resolution capability of ePPL. The black features indicate Pt particles with diameters ranging from ~210 nm to 280 nm. Scale bars = 500 nm. .... 46

**Figure 2.13.** Feature dimensions are controlled by deposition time and layering. (a) Optical and AFM images of a pattern consisting of 4 Ni features where height was controlled by varying the deposition time. (b) Optical and AFM images of a pattern with 2 Ni features here size is controlled by depositing multiple layers of Ni, 60 s at a time. Features shown are 10 vs. 1 layer. Scale bars = 5  $\mu\text{m}$ . ..... 46

**Figure 2.14.** Schematic depicting the hypothesized mechanism of ePPL deposition. (1) First, metal reduction occurs preferentially from the meniscus that forms between the tip and the substrate upon contact. (2) Once ions are depleted from the meniscus, reduction occurs directly from the hydrogel, at the tip-substrate interface. (3) When the tip is lifted, the shape and size of the resulting structure corresponds to the shape of the tip-substrate interface, along with a very thin layer from the meniscus..... 47

**Figure 2.15.** Feature size (diameter) measured as a function of deposition time, from features in Figure 3a. Horizontal feature size decreases slightly with increased deposition time because of the proposed mechanism wherein material deposits from a meniscus at first, followed by the deposition directly from the hydrogel pen, which is smaller than the meniscus (Figure S6). The height, nonetheless, is directly related to deposition time, as shown in Figure 2.13a. .... 47

**Figure 2.16.** AFM height profile of the features with (a) 5 and (b) 15 layers. Each layer was printed at 60 s deposition time, and the pen array was lifted each time by 100 nm in z-direction. (c) A plot of average feature height versus number of printed layers. The height increases with increased number of layers, demonstrating the potential of ePPL technique towards 3D printing..... 48

**Figure 3.1.** a) Illustration of the fabrication process of a cellular matrix with heterogeneous stiffness and topography at the sub-cellular to cellular level: (i) synthesis of photodegradable cross-linker, PEGdiPDA, (ii) hydrogel film formation using two glass slides spaced apart by a rubber spacer, (iii) pattern generation using the DMD system with 405-nm LED, and (iv) cellular analysis and control with patterned hydrogels. b) Schematic examples of pattern designs, where the green areas were locally exposed to light, (i) and representative AFM images of patterned hydrogels (ii) of 5  $\mu\text{m}$ -edge length square patterns with 5  $\mu\text{m}$  interpattern spacing (left) and 10  $\mu\text{m}$ -edge length square patterns with 10  $\mu\text{m}$  interpattern spacing (right). ..... 57

**Figure 3.2.**  $^1\text{H}$  NMR spectrum of a photodegradable cross-linker (PEGdiPDA). The peaks are color-coded and labeled with letters a – m with the protons in the molecule as shown in the inset. Solvent impurities are also indicated where  $\text{H}_2\text{O}$  and DMSO are used for water and dimethylsulfoxide, respectively. All the peaks matched those of the reported spectrum. .... 58

**Figure 3.3.** A plot of substrate stiffness versus input energy. As input energy increases, the substrate stiffness decreases..... 59

**Figure 3.4.** AFM images of the hydrogel films with  $15 \times 15 \mu\text{m}^2$  (a) and  $20 \times 20 \mu\text{m}^2$  (b) square patterns. Left: Elasticity map with mechanical variation encoded using DMD arrays. The dark brown regions indicate an area that was exposed to light, degraded, and became softer as a result. Right: The height profiles of the respective substrates. .... 59

**Figure 3.5.** Live/dead fluorescence assay of U87 glioma cells seeded and grown on patterned hydrogels on day three. Live and dead cells are indicated in green and red, respectively. Scale bars = 200  $\mu\text{m}$ . ..... 60

**Figure 3.6.** a) Bright-field images overlaid with fluorescence micrographs of U87 cells labeled with Cell Tracker Orange on patterned hydrogels. The edge length of the square patterns ranges from 5  $\mu\text{m}$  to 50  $\mu\text{m}$  with the same respective interpattern spacings. b) A plot delineating the effect of pattern size and spacing on the migration speed of cells, where controls are the bulk substrates without patterns (mean  $\pm$  SE; \*\*\*\* $p \leq 0.0001$ , \*\* $p \leq 0.01$ , ns  $p > 0.05$  based on one-way ANOVA;  $n \geq 3$  with over 30 cells analyzed for each sample). c) Confocal images of a single cell confined between 10  $\mu\text{m} \times 10 \mu\text{m}$  (top) and 15  $\mu\text{m} \times 15 \mu\text{m}$  (bottom) patterns. The nuclei (panel 1) and vinculin (panel 2) in the cells are fluorescently labeled, and their representative images are overlaid with differential interference contrast (DIC) images (panel 3), which are shown in panel 4. .... 62

**Figure 3.7.** Patterned hydrogels with increased nominal background stiffness. a) Representative stiffness (left) and height (right) profiles of a 10  $\times$  10  $\mu\text{m}^2$  square patterned substrate. b) Comparison of the migration speed of cells on a substrate with stiffness difference of either 8 kPa or 18 kPa between the patterned and unpatterned areas (mean  $\pm$  SE; ns  $p > 0.05$  based on one-way ANOVA; over 30 cells analyzed). ..... 65

**Figure 3.8.** Impact of pattern size on cell morphology: a) cell sizes, b) minor axis, c) aspect ratio, and d) circularity (mean  $\pm$  SE; \*\* $p \leq 0.01$ , \* $p \leq 0.05$  and ns  $p > 0.05$  based on one-way ANOVA;  $n \geq 3$  with over 50 cells analyzed for each sample). ..... 66

**Figure 3.9.** Steps for making topographical templates for hydrogel films. 1) S1805 photoresist (MicroChem Inc.) was spincoated on a Si wafer with a 500-nm thermal oxide layer (Nova Electronic Materials) at a spin speed of 500 rpm for 5 s and at 4,000 rpm for 40 s. It was then baked at 115  $^{\circ}\text{C}$  for 80 s. 2) The photoresist-coated Si wafer was exposed with a 405-nm laser for 60 s using a maskless aligner (Heidelberg MLA150). The desired patterns were pre-designed *via* AutoCAD software. 3) The pattern was developed in MF-319 developer for 60 s. 4) Height differences were selectively defined by deep reactive ion etching (DRIE, STS LpX Pegasus) with a 3kW RF Generator. The topological mold was made by alternately flowing  $\text{C}_4\text{F}_8$  (deep) and  $\text{SF}_6$  and  $\text{O}_2$  (etch) gas. The templates were etched for 6-8 mins, cycling with a depth for 2 s and an etch for 3 s. 5) The residual photoresist layer was removed using acetone. .... 67

**Figure 3.10.** AFM analysis of a hydrogel film with topographical features of uniform stiffness. a) Height profile of 5  $\times$  5  $\mu\text{m}^2$  square patterns spaced 5  $\mu\text{m}$  apart, and b) Stiffness map of the respective sample. .... 67

**Figure 3.11.** a) Height profile of the topographically patterned hydrogels. b) Representative Young's modulus map, depicting the uniform stiffness of the hydrogel. c) Effect of topographical variations on the migration speed of cells. Control samples are hydrogels without height features. Over 30 cells were analyzed for each condition. .... 68

**Figure 3.12.** Durotactic migratory behavior of cells. a) U87 cells cultured on topographically encoded substrates with heterogeneous (i) and uniform stiffness (ii). Confined cells are indicated in yellow. b) A plot representing the percentage of cells confined between the patterns as a function of the total cell count at each sample type..... 69

**Figure 3.13.** Schematic diagram of isotropically (a) and anisotropically (b) patterned substrates. For an isotropic sample, square patterns are equally distributed in both x and y directions whereas they are more closely spaced in one direction for an anisotropic sample..... 70

**Figure 3.14.** Characterization of the anisotropically patterned hydrogel using AFM. Darker brown regions in the stiffness profile (a) indicate soft spots where light has been exposed and caused swelling, which also correspond to lighter regions in the height profile (b). ..... 70

**Figure 3.15.** a) Fluorescence image of cells seeded on a hydrogel substrate patterned in an anisotropic manner ( $10 \times 10 \mu\text{m}^2$  patterns spaced  $5 \mu\text{m}$  and  $10 \mu\text{m}$  apart respectively in x- and y-direction). The image is overlaid with a bright-field micrograph. The cells aligned to the x-axis (horizontal direction) are indicated in yellow and those to the y-axis in purple. b) Magnified images of a cell indicated by the highlighted area in (a) at different time points, showing the cell alignment driven by durotaxis. c) The migration speed of cells grown on either control (no patterns), isotropic, or anisotropic substrates (mean  $\pm$  SE; \*\*\*\*p  $\leq 0.0001$  and ns p  $> 0.05$  based on one-way ANOVA;  $n \geq 2$  with over 30 cells analyzed for each sample). d) The percentage of cells aligned in the x-axis and y-axis for isotropic and anisotropic patterns. The confocal image for the isotropic sample is shown in **Figure 3.16**. ..... 71

**Figure 3.16.** Fluorescence image of cells seeded and grown on an isotropically patterned hydrogel. The cells aligned in the x-axis are labeled in red and those aligned in the y-axis are blue, and the respective cell count is 45 and 47, respectively. .... 72

**Figure 4.1.** AFM elasticity map of patterned hydrogel's surface using BPL arrays. (a) The pens with an aperture size of  $1 \mu\text{m}$  were used to locally expose hydrogel for 5 min. The sizes of the features are denoted, and the smallest features are indicated with dotted circles. (b) The capability of x and y patterning using BPL is demonstrated. Any changes in local stiffness are indicated with dotted circles. .... 84

**Figure 4.2.** Height (left) and modulus (right) profiles of patterned hydrogels without light exposure with  $\sim 1000$  mN (a) and  $\sim 2000$  mN (b) applied forces..... 85

**Figure 4.3.** HMSCs seeded and grown on the surface of uniformly degraded PEGdiPEA hydrogel. Green and red colors indicate live and dead cells, respectively. Scale bar =  $100 \mu\text{m}$ . ..... 86

**Figure 4.4.** Schematic diagram of PPL patterning for making molecular patterns..... 88

**Figure 4.5.** LFM friction images for MHA patterned Au substrates backfilled with EG3. The yellow dots represent MHA features, and the background is EG3. Samples with (a)  $5 \mu\text{m}$  and (b)  $2 \mu\text{m}$  pitch distance. .... 88

**Figure 4.6.** Movement of HUVEC cells on patterned surfaces. (a) Fluorescently labeled cells monitored were with confocal microscopy and analyzed with ImageJ software. The yellow line indicates the pathway of a cell, which is marked with a purple circle. (b) The plot of the average speed of cell migration for control, 5  $\mu\text{m}$ , and 2  $\mu\text{m}$  samples. .... 89

**Figure 4.7.** Expected gradient using the dual spray coating method. The compositional gradient is generated using two different inks, EG3-disulfide and maleimide-disulfide. More percentage of maleimide ink is expected in the horizontal direction as indicated here with an arrow. On the far left, only EG3 ink should be transferred to the substrate..... 90

**Figure 4.8.** Stitched confocal images of patterned EG3 and maleimide over a large area. The maleimide groups are functionalized with fluorescently labeled thiolated-single stranded DNA for visualization. .... 91

**Figure 4.9.** (a) Chemical structures of maleimides (50% and 25%) functionalized on Au surfaces *via* Au-S linkage. (b) The migration speed of HUVEC cells seeded on control samples where the surface of Au-coated substrates is functionalized with different percentages (50%, 25%, and 5%) of maleimides. These maleimides were coupled to the RGD peptides for cell attachment..... 92

**Figure 5.1.** Schematic illustration of PPL patterning steps for synthesizing nanocrystals. Figure adapted from ref. 124. Reprinted with permission from AAAS..... 98

**Figure 5.2.** a) SEM images of COF-1 polymers synthesized using the PPL approach. (i) a  $4 \times 3$  dot pattern on a fluoropolymer treated Si-wafer, with magnified images (ii) and (iii), displaying the particle formation. b) TAPB monomers patterned in a  $5 \times 5$  matrix. .... 99

**Figure 5.3.** COF-1 monomers patterned on Si-wafer without (a) and with (b) sulfolane in the precursor inks. The nanoreactors containing sulfolane take a longer time to evaporate. .... 99

**Figure 5.4.** SEM image of COF-1 feature patterned using the precursor ink with the increased amount of sulfolane..... 100

**Figure 5.5.** A  $3 \times 3$  dot matrix of COF-1 patterns synthesized with an aniline modulator. In each dot, large COF crystals were observed. .... 100

## LIST OF TABLES

<b>Table 2.1.</b> Chemical composition of Ni–Co deposited alloys as obtained by XPS. ....	44
<b>Table 2.2.</b> Applied voltages and minimum deposition times used for each metal deposition. ....	51
<b>Table 3.1.</b> Aspect ratio, circularity value, and directionality ratio of the cells seeded on control, isotropic, and anisotropic samples. Control samples are substrates with uniform stiffness (~6, ~16, and ~30 kPa) without stiffness and height heterogeneities.....	72

# **Chapter 1**

## **Introduction**

## 1.1. Background

In nanoscience and nanotechnology, the fabrication of multi-functional architectures with precise control over morphology and properties at a wide range of length scales, from the nanoscale to the macroscale, is a grand challenge.<sup>1-3</sup> These materials will possess unique and non-natural behaviors in chemical, mechanical, optical, thermal, and electronic properties that differ from those observed only at bulk scale.<sup>4</sup> In addition, having such spatial control will allow one to design materials with locally tunable physicochemical properties and reconfigurable capability, enabling the development of smart materials that can respond to external stimuli, including light, temperature, pH, voltage, and pressure. The creation of stimuli-responsive structures presents major opportunities and breakthroughs in fields including biotechnology, nanoelectronics, robotics, and sensing.

In an effort to design and fabricate these multi-scale functional materials, there has been a surge of interest in the development of new printing methods and approaches. A particularly promising platform is the cantilever-free scanning probe lithography (CFSPL).<sup>1, 2</sup> This method is developed based on a technique called dip-pen lithography (DPN)<sup>5, 6</sup>, which utilizes AFM tip to directly deliver the desirable materials or inks (i.e., molecules, polymers, liquids) onto the target substrates with high spatial precision without a harsh post-processing step. By using a 2D array of massively parallel pen tips (up to 11 million pens) composed of an elastomer, CFSPL-based techniques can overcome the throughput and scalability limitation of DPN and other conventional lithographic techniques, including electron beam lithography, near-field optical lithography, two-photon lithography, and focused ion beam lithography. These CFSPL pen tips are elastic and shaped in square pyramids, which allows one to easily generate features with sizes ranging from

nanometer to micrometer in mask-free fashion over square centimeter areas. Additionally, these techniques do not require vacuum conditions, making them desktop printer tools capable of nanofabrication at a low cost.

Despite recent advances, current CFSPL methods have been limited to mostly printing hard materials and 2D architectures. To construct a complex, multi-functional structure and go beyond two-dimensional printing, however, it is necessary to develop a material-versatile system that can deposit both hard and soft substances and pattern onto those materials. Compared to hard matter, soft materials can provide more flexibility and adaptability in terms of shape, texture, and configurations. Therefore, integration of soft materials in these printing systems is crucial to pattern a vast variety of materials and give more functionalities to the printed features and structures. These soft materials can be used as an ink, substrate, or printing tool itself.

This chapter provides a comprehensive review of CFSPL techniques, highlighting some of the important studies and work done using polymer pen lithography (PPL) and beam pen lithography (BPL). The current limitations in each technique are also outlined, explaining the motivation behind this dissertation and laying out the groundwork for the other chapters.

## **1.2. Cantilever-Free Scanning Probe Lithography**

### *1.2.1. Polymer Pen Lithography*

Polymer pen lithography (PPL) is one of the cantilever-free scanning probe lithographic techniques developed by the Mirkin group at Northwestern University in 2008.<sup>7</sup> This printing approach combines dip pen lithography (DPN) and microcontact printing, taking advantage of each method—feature size control and large-area printing, respectively. As one of the massively

parallel printing methods that allow high-throughput patterning over a large area, PPL allows for a rapid generation of arbitrary uniform patterns with feature sizes ranging from micro to nanoscale.

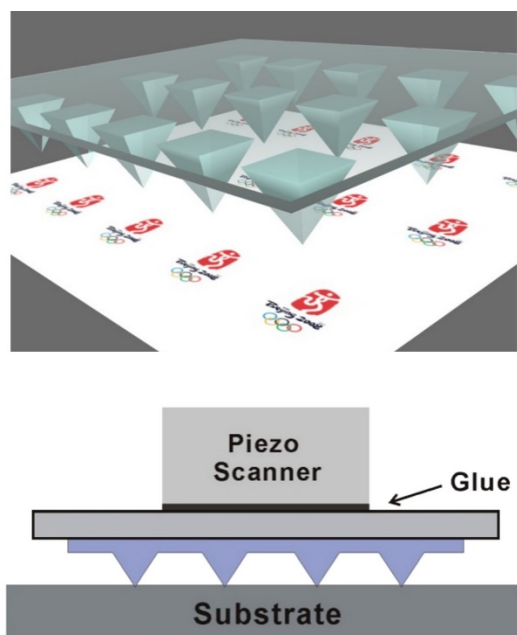


**Figure 1.1.** Illustration of PPL platform. The pen array is attached to the piezo scanner, enabling the pens to print arbitrary features with control over all  $x$ ,  $y$ , and  $z$  directions. When pens are in contact with the substrate, the ink is transferred and form a meniscus on the surface. Figure adapted from ref. 7. Reprinted with permission from AAAS.

PPL uses the 2D array of pyramidal-shaped pen tips made from a soft elastomeric material such as polydimethylsiloxane (PDMS). These pens are molded in a Si master with pre-designed pyramidal-shaped wells fabricated *via* conventional photolithographic technique. A typical pen array consists of as many as 11 million pen tips mounted on a rigid transparent backing layer (e.g., glass or quartz). Unlike DPN and micro-contact printing methods, this technique allows arbitrary features and patterns to be printed in a mask-free and cantilever-free fashion.

There are three basic steps in the patterning process of PPL: (i) inking of the pen array (ii) alignment of the pen tips with the substrate and (iii) delivery of the inks to generate pre-designed patterns.<sup>8</sup> In theory, any transferable materials can be used as inks, but it is important that they

have a higher affinity for the target substrate than for PDMS. Most commonly, alkanethiols, proteins, and lipids have been used as inks. Before patterning, the alignment step is crucial for controlled and consistent patterning. The pen tips need to be in parallel in order to generate features with size control over multiple length scales. The pen array can be leveled to be co-planar with the substrate using either optical or force feedback. Once the pen array is in contact, the ink is delivered from the pen tip to the substrate's surface by forming a meniscus, which enables the transport and diffusion of molecules. The feature size can be controlled by either how long the pen stays in contact with the surface (dwell time) or how much the pens are pressed against the substrate (contact size). One particular advantage of PPL is the precise placement of the features. The pen array is controlled by x,y, and z-piezo controllers, and the features are printed in a 'dot-matrix' manner where the pen array is raised after the contact and moved in x or y direction to generate the next dot. With this controllability, any arbitrary features can be designed and fabricated with PPL. For example, logos for the 2008 Beijing Olympic<sup>7</sup> and World Intellectual Property Organization (WIPO) were printed on Au-coated substrates using alkanethiols (16-mercaptohexadecanoic acid or MHA) as an ink (**Figure 1.2**). In the Olympic logo, the size of the dot representing the letters or numbers and the Olympic rings is respectively ~90 nm and ~600 nm. The patterned features can be confirmed by chemically etching the Au that is not bound to the thiol and visualized using the optical microscope.

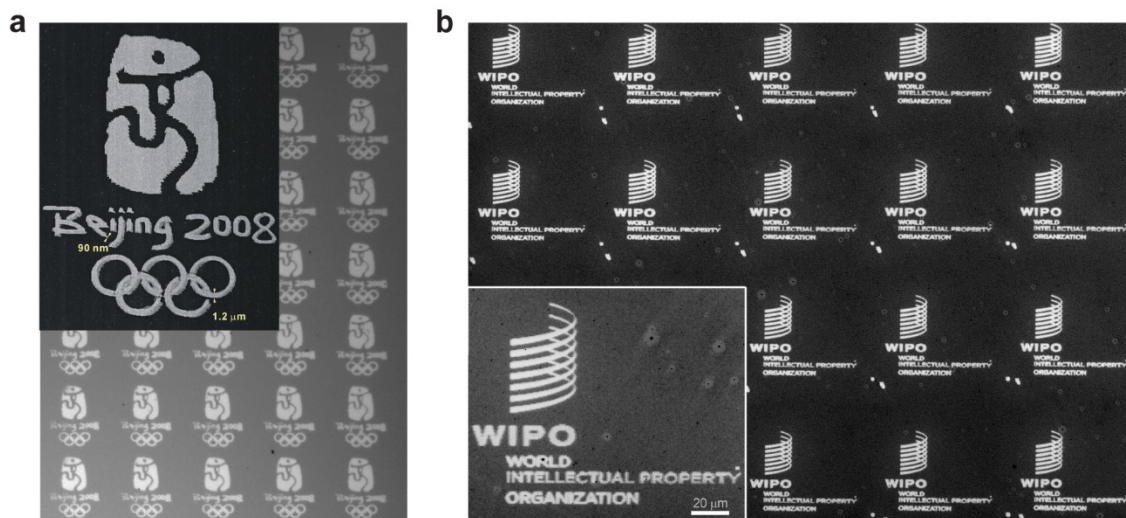


**Figure 1.2.** Optical images of logos printed with PPL. (a) ~15, 000 duplicates of the Beijing Olympic logo and (b) identical replicas of the WIPO logos on Au-coated substrate. Panel **a** adapted from ref. 7. Reprinted with permission from AAAS.

PPL is emerging as a new powerful lithographic technique that can print patterns of a wide variety of materials, including magnetic nanoparticles, metal nanoparticles, polymers, and biomolecules, such as oligonucleotides and proteins, that are commonly used in the semiconductor industry, biotechnology, catalysis, and electronics.<sup>9-11</sup> Recently, the PPL patterned features were used to modulate the organization of cell's cytoskeletal and control stem cell differentiation.<sup>10</sup> The actin fiber orientation was controlled using nanoscale adhesion patterns in a confined space independent of the overall shape of the pattern, which programmed stem cells to undergo differentiation to a different fate. For instance, human mesenchymal stem cells differentiate into adipogenic lineage when they adapt a circular shape. In this study, however, they underwent osteogenesis due to the anisotropically patterned underlying nanofeatures. Because PPL can pattern molecular features on the scale of individual focal adhesions, it enables a systematic study of cell-ECM interactions, which can provide new insights for tissue engineering and regenerative medicine and help to address some fundamental questions in biology and life sciences.

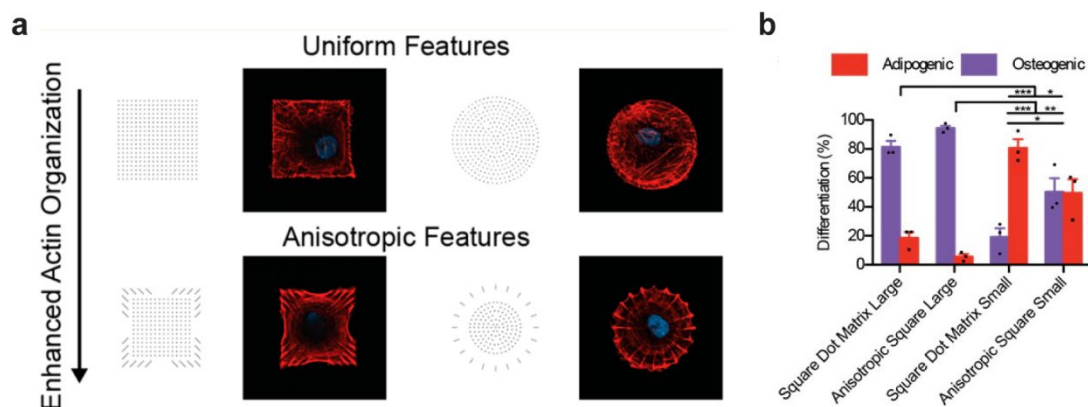


**Figure 1.3.** Pattern designs and fluorescence micrographs of hMSCs' actin cytoskeleton on the respective pattern. Reprinted with permission from Ref. 10. Copyright (2019) American Chemical Society.

Combining the ink spray-coating method, which sprays two different inks in a compositional gradient, with the PPL technique, a combinatorial library of a target material with compositional and size gradients can be synthesized (**Figure 1.4**).<sup>11</sup> For example, the compositional gradients of Au-Cu alloy nanoparticles were fabricated in a single substrate to screen and identify the most active composition for carbon nanotube growth. The PPL pen array was inked in a linear gradient with two aqueous solutions of PEO-*b*-P2VP containing either auric acid or cupric nitrate. This gradient was then transferred onto the substrate during the patterning. The size gradient was also generated by varying the amount of ink loaded on each pen. By tilting the pen array, the same size gradient can be generated in place of ink loading approach.

One major limitation of the current PPL platform is that the ink will deplete after 2-3 times of patterning and cannot be continuously replenished.<sup>12</sup> The pens are usually inked by drop-casting, sping-coating, or spray-coating, which can only deposit a small amount of ink material on the surface of the pen array. Also, the PDMS elastomer that is used to fabricate the pens cannot store the ink materials inside, making the reinking and realignment process inevitable. To address this

problem, a highly absorbent soft material that can maintain the defined shape, such as hydrogel can be used as the replacement of PDMS. The work towards this goal is described more in the following chapter.

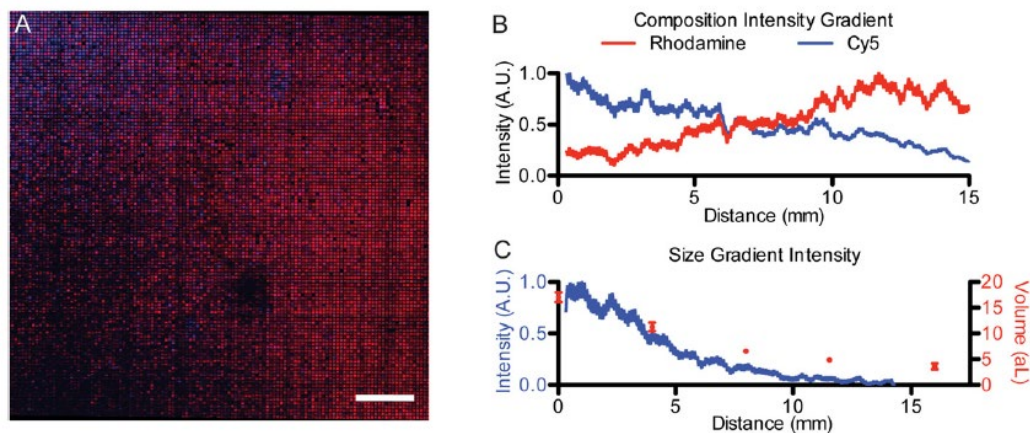


**Figure 1.4.** a) Confocal images of two different polymer domes containing fluorophores patterned with compositional and size gradients using a spray-coated PPL array. Average fluorescence intensity was measured across the substrate and plotted against (b) composition and (c) size. Reprinted with permission from ref. 11; Copyright (2019) National Academy of Sciences.

### 1.2.2. Beam Pen Lithography

Beam pen lithography (BPL) is another cantilever-free scanning probe lithographic technique reported by the Mirkin group in 2010 that can effectively perform highly localized photochemistry from nano- to microscale in a systematic manner.<sup>13</sup> BPL is the advanced platform of PPL combined with the near-field scanning optical microscopy (NSOM)-based lithography. This method operates by delivering light through a metal-coated elastomeric array that consists of millions of pyramidal pens with apertures at the pen apex (**Figure 1.5a**). BPL can generate features with sizes as small as 100 nm using 400 nm light, overcoming the diffraction limit. Like PPL, BPL is also connected to an x, y, and z-piezo controller, allowing the patterning of arbitrary features on a surface. For example, ~15,000 replicas of the Chicago skyline can be printed on a Si-wafer coated

with a photoresist (**Figure 1.5b**). After the light exposure, gold metal was deposited, and the photoresist was lift off. Each gold dot feature in the image is about  $450 \pm 70$  nm in diameter and was created using a BPL array with a 500 nm aperture size.

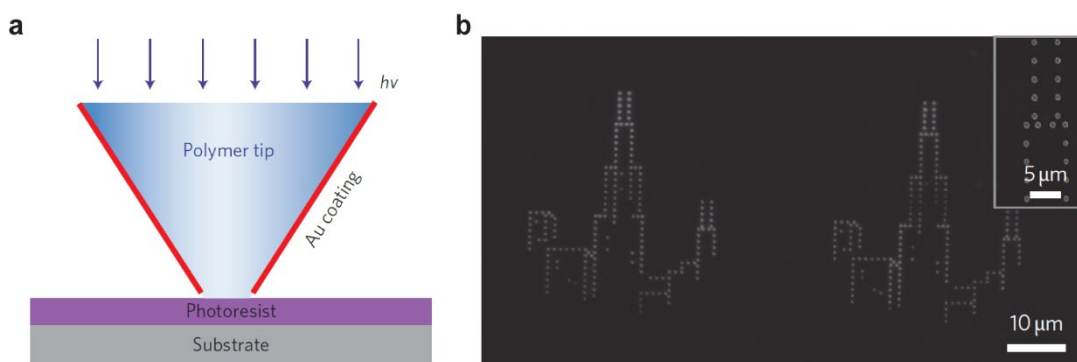


**Figure 1.5.** a) Schematic diagram of BPL, illustrating the patterning process where light is going through a transparent PDMS tip and exposes a surface of the substrate coated with light-responsive photoresist. b) A Chicago skyline patterned with BPL. Figure adapted from ref. 13. Reprinted with permission from AAAS.

The key to controlling the size of the patterned feature in BPL is to vary the aperture size at each pen tip (**Figure 1.6**). Using a pen array with various sizes of apertures, patterns with the feature size that spans a dynamic range of length scales can be printed on the surface of the substrate. Such property allows high-throughput and arbitrary patterning on any light-responsive materials at high resolution.

One of the advantages of BPL is that the actuation of individual pen tips is feasibly achievable; selective illumination can be achieved by using a digital micromirror device (DMD).<sup>14</sup> Controllability over individual pens enables the patterning of a single centimeter-scale image instead of replicas of predesigned patterns. Using the actuated arrays, Au serpentine resistors in continuous lines were printed, and the ability of BPL to fabricate functional devices has been demonstrated.

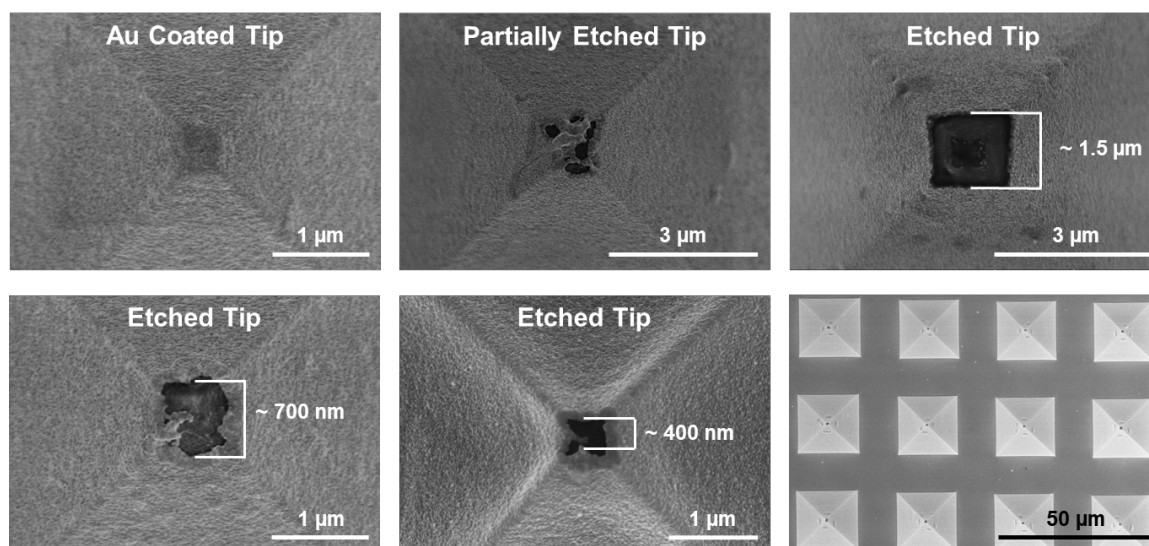


**Figure 1.6.** SEM images of beam pen arrays with apertures of varying sizes. Deposited gold at the tip of the pen array is chemically etched to allow light to pass through and delivered onto the surface of the substrate.

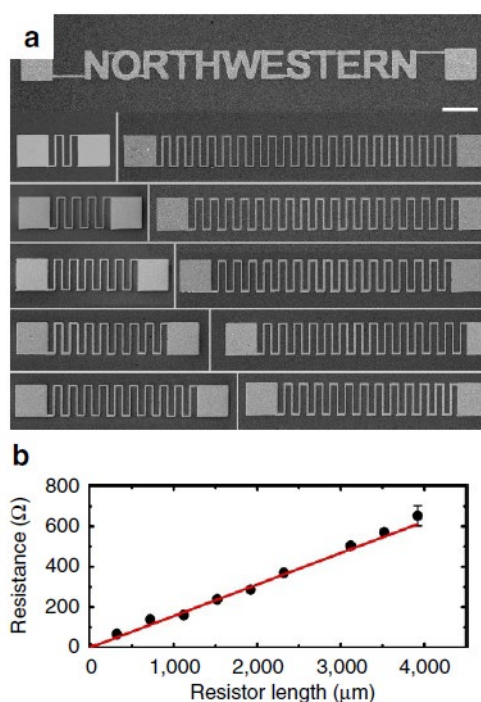


**Figure 1.7.** a) Gold serpentine resistors patterned in centimeter-scale *via* BPL using 3 to 15 actuated pen tips. Scale bar is 100  $\mu\text{m}$ . b) The resistance was measured and plotted against the resistor length. Reprinted with permission from ref. 14; Copyright (2013), Nature Publishing Group.

So far, BPL patterning has been mainly demonstrated on rigid substrates, especially on a Si-wafer coated with a thin layer of a photoresist. However, the structural aspect of the BPL can enable it to effectively pattern on soft materials: the elastic mechanical properties of PDMS allows to gently make contact with the surface without severely damaging the substrate. Combining the capability of BPL with soft materials can overcome the limitations that exist at the interface between nanotechnology and soft materials. Current conventional lithographic techniques cannot reliably pattern and fabricate soft materials and are incompatible with existing ones. In the later chapter of this thesis, the efforts to integrate the BPL system with one of the kinds of soft materials, hydrogel, are described.

### 1.3. Thesis Overview and Objectives

Herein, the basic concepts of CFSPL techniques, polymer pen lithography and beam pen lithography, were introduced and described. To generate dynamic and functional structures with multi-scale controllability, the capability of CFSPL needs to be expanded to print both hard and soft materials over large areas. The strategies used and chemistries developed to integrate soft materials with BPL and PPL platforms are outlined in this thesis. The use of hydrogel as the printing medium to deliver metal ion inks *via* an electrochemical approach is described in **Chapter 2**. Here, a novel printing approach termed electrochemical polymer pen lithography (ePPL) is described. **Chapter 3** and the part of **Chapter 4** focus on using photo-responsive hydrogels as substrate to probe and control cellular behavior. Using light, the local chemistry (e.g., crosslinking density) of these gel substrates is modified, changing the mechanics and topographical properties. These variations in the substrates' physical properties are used as physical cues (or factors) to

control cell migration and differentiation. Specifically, in **Chapter 4**, the strategies for using BPL to generate sub-micron features on the hydrogel-based matrices are depicted. In addition, the methods to encode chemical cues using PPL on 2D substrates are described. A compositional gradient of two different bioinks can be generated and used to control directional cell migration. **Chapter 5** reports a new synthetic approach for synthesizing crystalline polymeric networks and covalent organic frameworks using PPL. Small organic molecules and monomers are used as inks and delivered onto the substrate, where each patterned dome serves as a nanoreactor. Lastly, **Chapter 6** concludes this dissertation by summarizing the advancements and work described in the previous chapters, outlining their outlook, and proposing new future directions for further development.

## Chapter 2

### Electrochemical Polymer Pen Lithography

This chapter describes a novel printing method where soft material is utilized as a medium or a tool to deliver the inks needed to build 2D to 3D functional materials. We report the development of a massively parallel lithographic technique called electrochemical polymer pen lithography (ePPL). Pyramidal pen arrays, consisting of more than 10,000 hydrogel pens loaded with metal salts, are integrated into a three-electrode cell and used to reduce ions at each pen tip locally. This system enables high-throughput patterning of a variety of metallic inks (e.g.,  $\text{Ni}^{2+}$ ,  $\text{Pt}^{2+}$ ,  $\text{Ag}^+$ ) on the nanometer to micrometer length scale. By incorporating a z-direction piezo actuator, the extension length and dwell time can be used to precisely define feature dimensions (210 nm to 10  $\mu\text{m}$  in width, and up to 900 nm in height, thus far). Furthermore, by controlling the potential and precursor concentrations, more than one element can be simultaneously deposited, creating a new tool for the synthesis of alloy features, such as Ni-Co, which are relevant for catalysis. Importantly, this methodology enables fine control over feature size and composition in a single pattern, which may make it ultimately useful for rapid, high-throughput combinatorial screening of metallic features.

---

Materials in this chapter is based upon published work (with permission from Wiley):

**E. Oh**, R. Golnabi, D. Walker, C. A. Mirkin. *Small Accepted* (2021)  
DOI:10.1002/sml.202100662

## 2.1. Introduction

Metal micro- and nano-structures have widespread applications in the fields of electrocatalysis, electronics, plasmonics, and magnetism.<sup>15-18</sup> In order to synthesize, prototype, and discover structures with enhanced activity, methods for printing libraries of materials with control over their size, composition, and location on a single substrate have been developed,<sup>11, 15, 19, 20</sup> including conventional metal printing approaches such as direct metal laser sintering (DMLS), selective laser melting (SLM), selective heat sintering (SHS), and electron beam melting (EBM). However, these methods often require an inert atmosphere and vacuum conditions, high temperatures to melt the material, and post-processing steps, all of which make them expensive and labor intensive.<sup>21, 22</sup> Inkjet printing is another common metal printing approach, but it requires thermal annealing or chemical treatments, and the resolution of printed features is usually limited to the micrometer range.<sup>23</sup> In a departure from these methods, electrochemical deposition possesses many benefits, including independent control over the volume and composition of deposited metal features with high-resolution and without the need for vacuum conditions or post-processing.<sup>24-26</sup> While electrochemistry is a fast, inexpensive, and highly versatile technique for depositing metals, it is typically used for conventional thin-film electroplating, template-based nanoparticle and wire synthesis, or serial single nanostructure deposition.<sup>27-34</sup>

Scanning probe electrochemical deposition techniques are attractive because they can be used for site-specific nanoscale 2 and even 3D metal printing onto a conducting substrate.<sup>21, 28, 32, 35-44</sup> For example, researchers have used nanopipettes or atomic force microscopy (AFM) tips loaded with metal salt solutions to locally plate metals directly onto cathodic surfaces.<sup>21, 28, 32, 37, 38, 41, 42, 44</sup> In another technique, a metal ion-embedded hydrogel was molded into a pyramidal shape

and used for electrodeposition *via* the diffusion of metals ions through the hydrogel and reduction on a surface.<sup>39, 40</sup> However, in all cases, the use of only one or two tips makes patterning large-areas cost- and time- prohibitive, thus limiting their scope of use.

A scalable approach may be possible through an existing large-area patterning technique: polymer pen lithography (PPL). PPL is a scanning probe method that relies on an array of elastomeric pyramidal polydimethylsiloxane (PDMS) tips coated with an aqueous “ink” to physically deposit material onto a substrate.<sup>7</sup> With PPL, up to millions of pens act in parallel, allowing users to make many replicas of structures, or when coated with ink gradients, complex libraries of structures with positionally encoded features, termed megalibraries.<sup>11</sup>

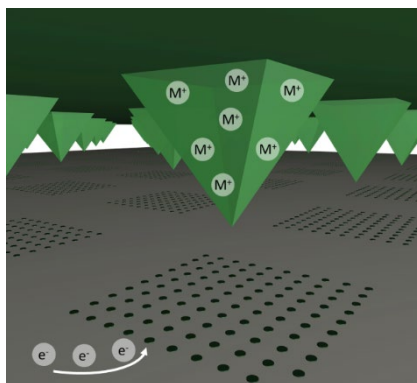


**Figure 2.1.** Schematic illustration of electrochemical polymer pen lithography.

Here, we report the development of a new method for the massively parallel, localized electrodeposition of metallic features on substrates (**Figure 2.1**). A variant of PPL, this technique, termed electrochemical polymer pen lithography (ePPL), utilizes a hydrogel pen array as the patterning tool and ink reservoir. ePPL combines the scanning probe capabilities of PPL with the flexibility of electrochemical deposition by integrating a metal salt-loaded hydrogel pen array with a three-electrode electrochemical cell. This architecture allows for the parallel deposition of a variety of metals with control in the x, y, and z directions using >10,000 pens over cm-scale areas.

In addition, ePPL does not require solution-phase surfactants, cleanrooms, or vacuum environments. Importantly, the technique can be used to generate single or polyelemental features, opening the possibility for generating material thin film libraries in a manner complementary to nanoparticle megalibraries.

## 2.2. Results and Discussions

### 2.2.1. *Electrochemical Pen Arrays*

To perform electrochemical deposition with the existing PPL platform and architecture, a pen array was fabricated with a polyacrylamide hydrogel because it is easily cured into a mold, can be chemically affixed to a stiff conductive substrate through an acrylate monolayer, and absorbs and transmits aqueous solutions through its polymer network. The gel can be also loaded with metal ions while still retaining its fidelity (i.e., stiffness and sharp tips). A pre-polymer solution was prepared as described in the experimental section, poured into a silicon master through a custom-designed, three electrode cell and covered with an acrylated functionalized indium tin oxide (ITO)-coated glass slide. As the hydrogel cured into the form of a cm-scale pen array, it adhered to the surface of ITO. The ITO slide not only functions as the counter electrode, but also provides planarity of the array and optical transparency, which allow the pens to uniformly make contact with the substrate during the patterning process. The pen arrays were then loaded with metal salt solution, thus functioning as the electrolyte and the source of the metal ions. this hydrogel was incorporated into a three-electrode fluid cell (**Figure 2.2a and c**) for a precise and consistent electrodeposition. With this cell, the pen array can be attached to the piezo while remaining hydrated and connected to a reference electrode. An Ag/AgCl reference electrode is

used to monitor the applied voltage and current, and a conductive substrate (i.e., Au-coated Si-wafer) serves as the working electrode. In a typical experiment, the pen array is brought into contact with a conductive substrate using an AFM (**Figure 2.2b**), and an appropriate voltage is applied which reduces the metal ions at each pen location.

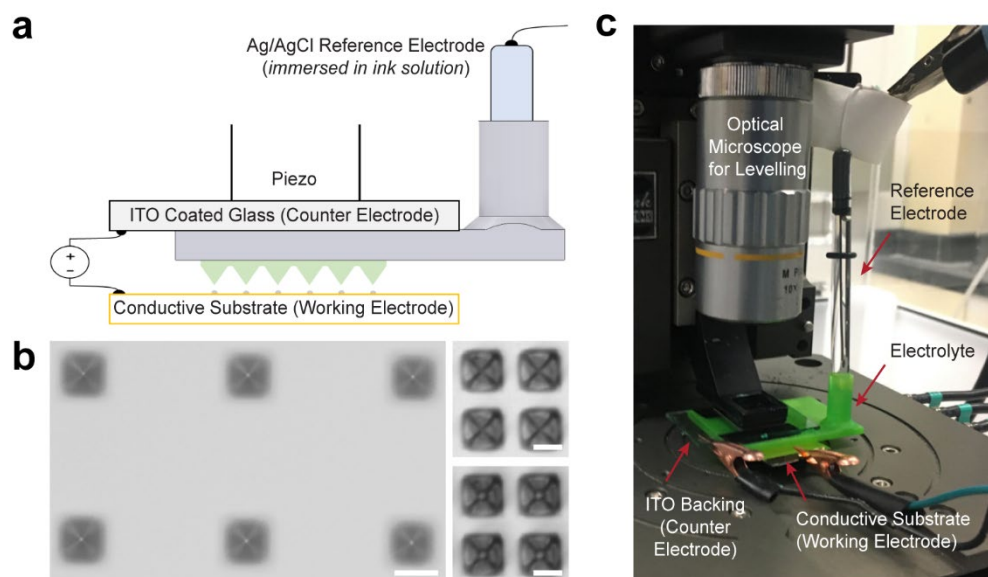


**Figure 2.2.** Experimental setup of ePPL. (a) Schematic of a three-electrode cell designed to hold the hydrogel array, electrolyte, and reference and counter electrodes in place during patterning. (b) Optical image of fabricated polyacrylamide hydrogel pen arrays, which were prepared by curing the hydrogel within a silicon master (scale bar = 30  $\mu\text{m}$ ). Images on the right show a pen array during the patterning process, highlighting how contact was determined: pens (top) out-of-contact and (bottom) in-contact with the substrate (working electrode) (scale bars = 15  $\mu\text{m}$ ) (c) Photograph of the experimental setup in a Park AFM, showing the cell, electrodes, electrical leads, and optical microscope used for leveling. Inset shows an image of the hydrogel pen array mounted within the cell.

In order to determine the potential needed to reduce metal ions through this hydrogel pen array, cyclic voltammetry (CV) experiments were performed. Both reduction and oxidation peaks were observed in the duck-shaped CV scans at three different scan rates (**Figure 2.3**), indicating that our ePPL platform behaves similarly to a general diffusion-limited system. The experimentally determined  $E_{1/2}$  is  $-0.453 \pm 0.004$  V (vs. Ag/AgCl), consistent with the reduction potential of  $\text{Ni}^{2+}$

to Ni(s), which is  $-0.459$  V (vs. Ag/AgCl) for a  $1.32$  M solution. While  $-0.453$  V is sufficient to deposit Ni, the rate of deposition at this potential is low. To increase the rate of deposition, a much more negative potential of  $-0.95$  V was applied. Higher potential than  $-1.0$  V was avoided, however, because the formation of bubbles from hydrogen evolution reaction was observed and disrupted a clean Ni deposition.

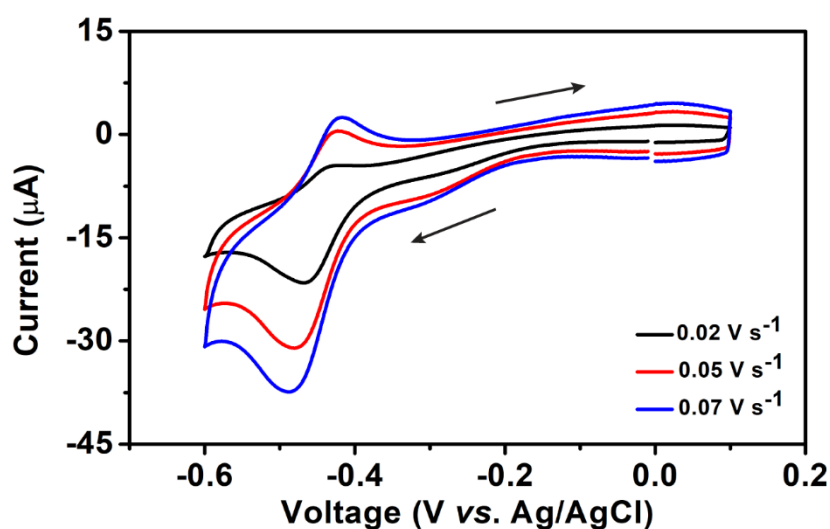


**Figure 2.3.** CV scans for a Ni-embedded hydrogel 3-electrode cell at three different scan rates, indicating both reduction and oxidation potential peaks.

### 2.2.2. Single Metal Patterning

Using a hydrogel pen array loaded with a nickel sulfamate electroplating solution ( $\sim 1.32$  M), a proof-of-concept experiment was performed on an Au-coated Si-wafer substrate (or working electrode). The hydrogel with the counter and reference electrodes was loaded into an AFM, and the contact point of each tip across the array with the substrate was determined optically as the color of center of the pyramidal tip changes from dark black to white upon contact (**Figure 2.2b**). To verify the consistency of patterning with the three-electrode cell, a pattern of three Ni features

in a line was printed; a reduction potential of -950 mV was applied for 60 s at the point of contact for each pen in a single array, moving  $8\ \mu\text{m}$  between points at  $0.1\ \mu\text{m/s}$  (**Figure 2.4a**). The resulting features had an average width of  $4.5 \pm 0.7\ \mu\text{m}$ , indicating the relative uniformity of the patterning across the substrate.

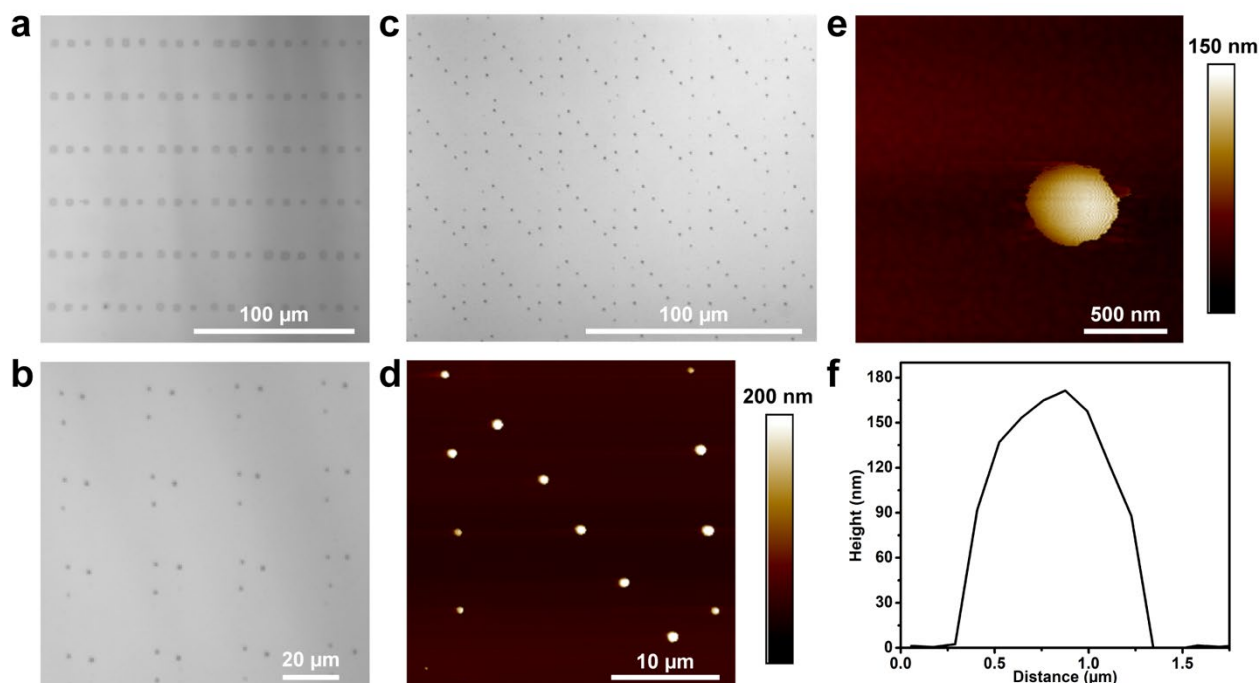


**Figure 2.4.** Patterning capabilities of ePPL. Optical micrographs of patterns of (a) Ni on a Au substrate (scale bar =  $100\ \mu\text{m}$ ), (b) Ag on an ITO substrate (scale bar =  $20\ \mu\text{m}$ ), and (c) Pt on a Au substrate (scale bar =  $100\ \mu\text{m}$ ). The Pt pattern consists of an array of 13 dots arranged as the letter ‘N’ at each pen location. AFM images of (d) a single ‘N’ (scale bar =  $10\ \mu\text{m}$ ) and (e) a single Pt particle (scale bar =  $500\ \text{nm}$ ). (f) The associated line scan of one of the particles in panel d.

To confirm that the observed metal features were electrochemically deposited rather than physically transferred from the hydrogel, control experiments were carried out (**Figure 2.5**). First, Ni patterning was performed without an applied voltage. As expected, no features were observed. For the other control test, voltage was applied, and the resulting patterned substrate was thoroughly rinsed with water and then sonicated to remove any residual salt from the substrate (**Figure 2.6**).

Even after this aggressive washing, the patterns remained visible, indicating that the observed features are not salt or liquid residue from the hydrogel, but rather metallic features adhered to the substrate. The resulting patterns were also characterized *via* x-ray photoelectron spectroscopy (XPS) and atomic force microscopy (AFM) (Figure 2.4b-d, Figure 2.7).

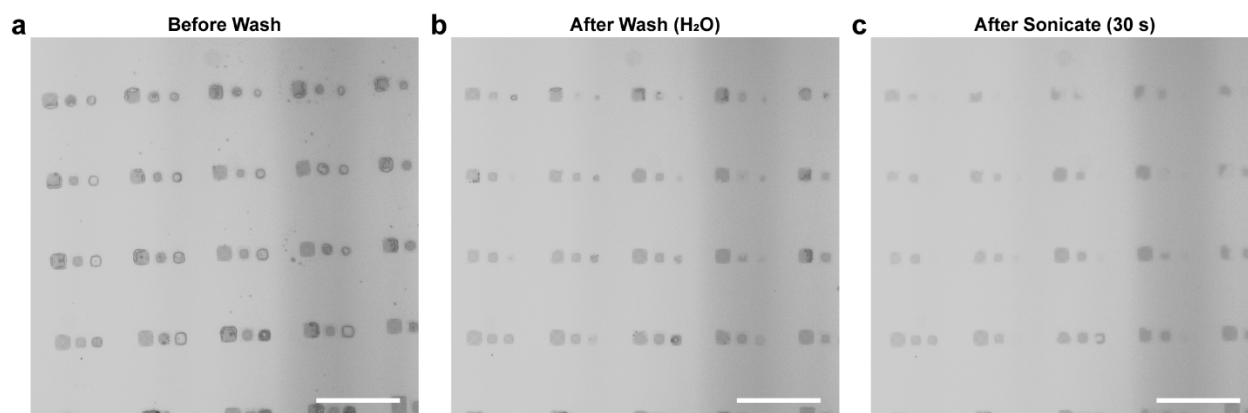


**Figure 2.5.** Optical images of a substrate with Ni features before and after extensive rinsing indicating the presence of reduced metal. A Au-coated Si wafer was patterned with an array of 3 Ni features from each tip (a), washed thoroughly with water (b), and then sonicated for 30 s in water (c). While the features faded after agitation, this experiment shows that the patterned features are reduced metal on the substrate and not salt residue. Scale bars = 30  $\mu\text{m}$ .

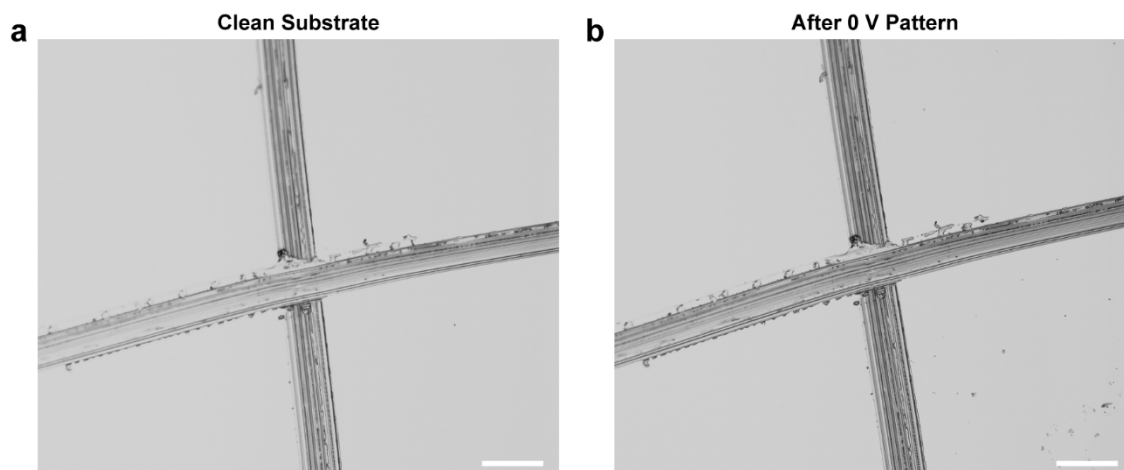


**Figure 2.6.** Control patterning experiment shows that an applied voltage is needed for metal deposition to occur. A Au-coated Si wafer was scratched with a cross and imaged before (a) and after (b) typical Ni patterning with 0 V applied. No patterned features are observed. Scale bars = 50  $\mu\text{m}$ .

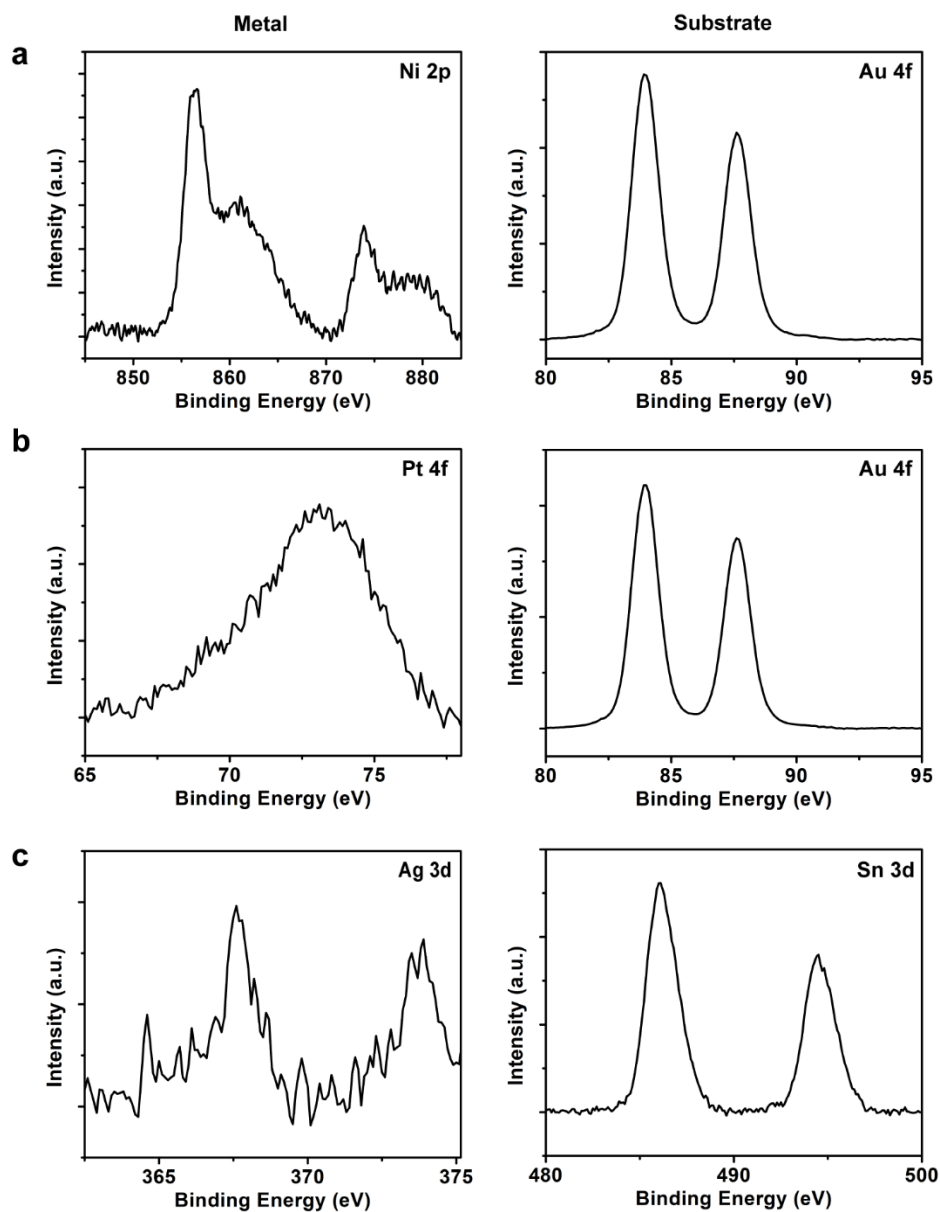


**Figure 2.7.** XPS patterns of the patterned samples confirm the presence of metal on the respective substrates. (a) Ni features on a Au-coated Si wafer. The peaks at 856 eV and 873 eV (left) are expected Ni 2p peaks. Au 4f peaks are observed at 84 eV and 87.7 eV (right). (b) The peak at 73 eV (left) indicates Pt on Au-coated Si substrate with Au 4f peak at 84 eV (right). (c) The presence of the Ag is confirmed by the peaks at 367 eV and 373.6 eV (left) and the peaks at 486 eV and 494.5 eV (right) are assigned to Sn 3d from the indium tin oxide (ITO) coated glass slide. The main peaks in the deposited features are all oxides due to rapid oxidation upon exposure to ambient conditions.

The arbitrary patterns of different metals such as Pt and Ag were generated in addition to Ni (**Figure 2.4c-f** and **Figure 2.5**, respectively) to test the ink versatility of this lithographic tool. For instance, the letter "N" comprised of 13 dots was printed per pen on an Au-coated Si-wafer using Pt (**Figure 2.4c** and **d**) where a reduction potential of -500 mV was applied for 10 s. The average diameter and height of these individual features were respectively  $777 \pm 247$  nm (CV = 0.32) and  $166 \pm 32$  nm (CV = 0.19) as characterized *via* AFM (**Figure 2.4e and f**). The variation in size among these small features is a result of manual contact point detection at each feature location and is expected to improve through automation of the contact point detection during patterning. The Ag features (-950 mV for 10s) were successfully patterned on an ITO-coated glass slide (**Figure 2.4b**), further confirming the substrate versatility of this ePPL system. The elemental analysis of these printed features was performed using XPS (**Figure 2.7**).

### 2.2.3. *Multimetallic Patterning*

In addition to single metal structures, multimetallic features, as long as they have comparable reduction potentials, can be printed over large areas using ePPL as this technique is diffusion-based; multiple metals may be absorbed by the hydrogel at once. A hydrogel pen array was saturated with a 10:1 nickel-cobalt salt solution and used to pattern Ni-Co alloys, one of the well-known hydrogel evolution reaction (HER) catalysts,<sup>45</sup> on an Au coated silicon wafer at -550 mV. Relatively larger features were patterned for characterization purposes and in order to determine the composition of the deposited features using a surface-sensitive technique like XPS that requires sufficient signal from the substrate (**Figure 2.8a**). The formation of smaller features around 2  $\mu$ m is, however, possible as evident in **Figure 2.9**. The AFM image (**Figure 2.10a**)

indicates that the Ni-Co feature also has an initial base layer like the single Ni pattern. As metal ions are delivered and reduced from the hyper-extended pen tips (extension height  $\sim 8.5 \mu\text{m}$ ), they form a pyramidal structure that corresponds to the shape of the pen tip (Figure 4a inset). The AFM line scan shows that these patterned features are  $\sim 80 \text{ nm}$  tall, with the base layer of  $\sim 12.5 \times 12 \mu\text{m}^2$  and  $10 \text{ nm}$  in height (Figure 2.10b).

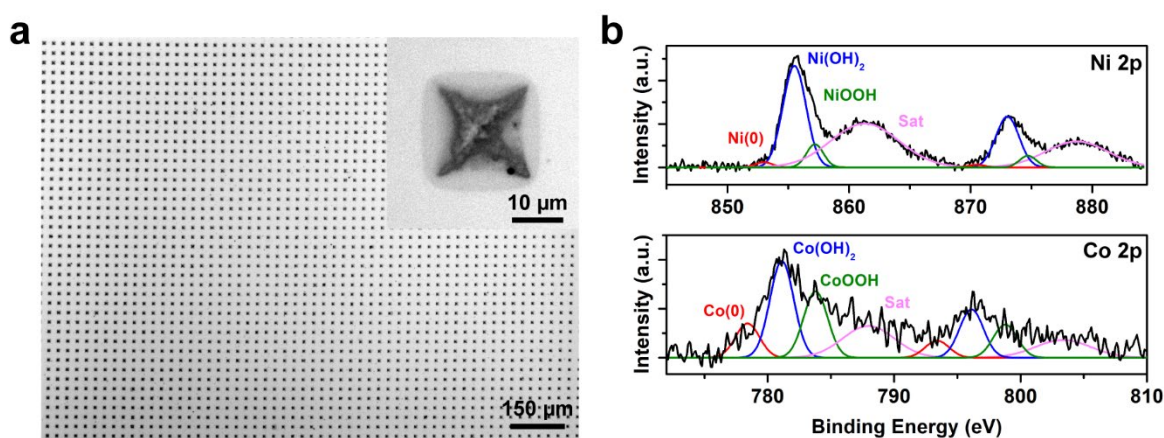


**Figure 2.8.** Deposition of Ni-Co alloys. (a) Optical micrograph of a large-area pattern of  $>10 \mu\text{m}$  Ni-Co features. The large feature size enables accurate elemental characterization. Inset shows a single feature. (b) XPS characterization of these patterns indicates that both the Ni and Co are present mainly as oxides. Auger peaks have been subtracted for clarity.

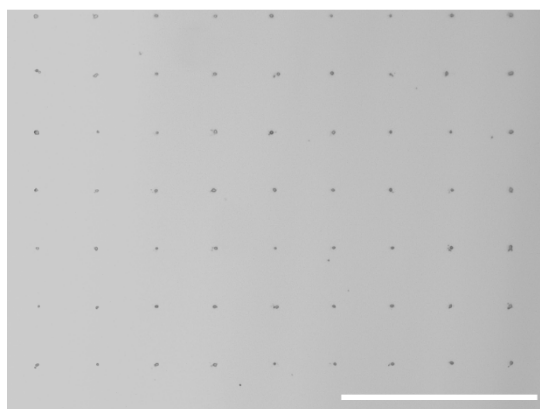


**Figure 2.9.** Optical micrograph of Ni-Co particles patterned on a Au substrate. Scale bar =  $50 \mu\text{m}$ .

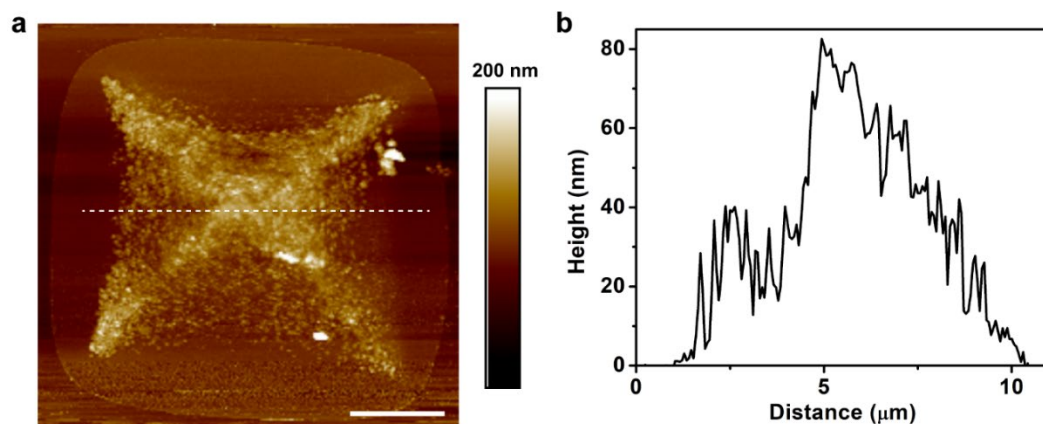


**Figure 2.10.** (a) AFM height profile of a large Ni-Co feature, and (b) AFM line scan across the large feature in (a), location indicated by dashed line. Scale bar = 3  $\mu\text{m}$ .

To confirm the presence of reduced Ni and Co, XPS analysis was performed (**Figure 2.8b**). The Ni 2p and Co 2p spectra show two major peaks corresponding to  $2p_{3/2}$  and  $2p_{1/2}$ , each followed by a satellite peak. Spin-orbit coupling constants of 17.4 eV and 15.0 eV were observed for the Ni and Co 2p peaks, respectively. As shown in Figure 4b, the 2p peaks are best fit with three gaussian curves for both Ni and Co suggesting the presence of three different chemical environments. For Ni, the appearance of a peak at 852.6 eV reveals that some of the patterned Ni is in the fully reduced Ni(0) state. However, the major peak is at 855.6 eV, indicating that most of Ni features exists as Ni(OH)<sub>2</sub>. Because the patterning process was performed in ambient condition and the ink solution itself contained H<sub>2</sub>O, the oxidation of Ni metal is expected and occurred post deposition. In the presence of water, Ni(OH)<sub>2</sub> is easily oxidized to oxyhydroxide (NiOOH), thus explaining the minor peak at 857.2 eV.<sup>46</sup> Similar behavior is expected for Co, and this explains the peak at 783.7 eV for Co from CoOOH.<sup>47</sup> Additionally, while there is clear indication of metallic Co, as evidenced by the peak at 778.4 eV, the majority of the feature is in hydroxide form as suggested by the primary peak at 781.1 eV. In order to improve the catalytic or electronic properties of the

oxide features patterned using ePPL, conventional methods for thin-film or nanoparticle reduction may be employed such as high-temperature annealing in a hydrogen environment.<sup>48, 49</sup>

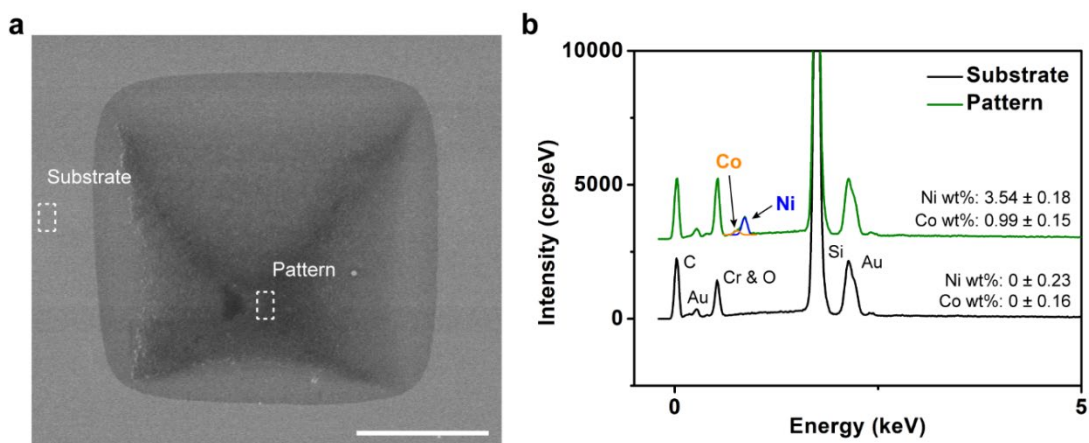


**Figure 2.11.** EDS characterization of a Ni-Co feature indicates the presence of both Ni and Co in the deposited region. Ni-Co was patterned on a Au-coated SiO<sub>2</sub> wafer with a chromium adhesion layer. Corresponding metal peaks are labeled. Scale bar = 5  $\mu$ m.

**Table 2.1.** Chemical composition of Ni-Co deposited alloys as obtained by XPS.

Ratio Ni:Co	Applied Potential (mV)	Ni% at/at	Co% at/at
10:1	-525	77.3	22.7
10:1	-550	79.4	20.6
10:1	-575	81.1	18.9
1:1	-525	38.5	61.5
1:1	-550	40.9	59.1
1:1	-575	41.7	58.3

The composition ratio of Ni-Co was analyzed using both energy-dispersive X-ray spectroscopy (EDS) and XPS. As shown in **Figure 2.11**, EDS data shows 3.56:1 of Ni:Co (atomic %) in the printed structures. The ratio was further confirmed by XPS where the % of Ni to Co calculated based on the area of the 2p<sub>3/2</sub> peaks is 3.86:1. Due to the different reduction

potentials of Ni and Co, the composition ratio can be controlled by changing the applied voltage as indicated in **Table 2.1**, which shows the composition of Ni-Co patterns generated at three different voltages, -525 mV, -550 mV, and -575 mV, and at two different initial concentrations (10:1 and 1:1 Ni:Co). Generally, an increase in Ni content is observed as more negative potential is applied.

#### *2.2.4. Feature Size Control and 3-Dimensional Printing*

In order to use ePPL for high-throughput printing of 3-dimensional metallic structures, both the width and height of printed features must be able to be precisely controlled. The width of each feature is adjusted by changing the force applied, and therefore the pen-substrate contact area, where the smallest diameter achieved was  $\sim 210$  nm (**Figure 2.12**). This corresponds approximately with twice the radius of curvature of each tip. Two methods were used to successfully control feature height: (i) varying the deposition time and (ii) layer-by-layer deposition.

In the first case, we found that, as expected, the height of a Ni feature increased linearly as the deposition time increased (**Figure 2.13a**). It is important to note that a thin base layer was observed for all deposition times, and is particularly clear at 5 s and 20 s. We hypothesized that during patterning, as with dip-pen nanolithography,<sup>5, 50, 51</sup> an electrolyte meniscus is initially formed as the pens are brought into contact with the substrate, and the ions in the meniscus are reduced first, resulting in a very thin layer (**Figure 2.14**). As the deposition time is increased and the ions in the meniscus are depleted, however, reduction occurs directly from the hydrogel as it becomes the only source of metal ions. Because the contact area of the hydrogel-substrate is

smaller than that of the meniscus, the size of the subsequent layers is smaller in width as shown in the later time points (**Figure 2.15**).

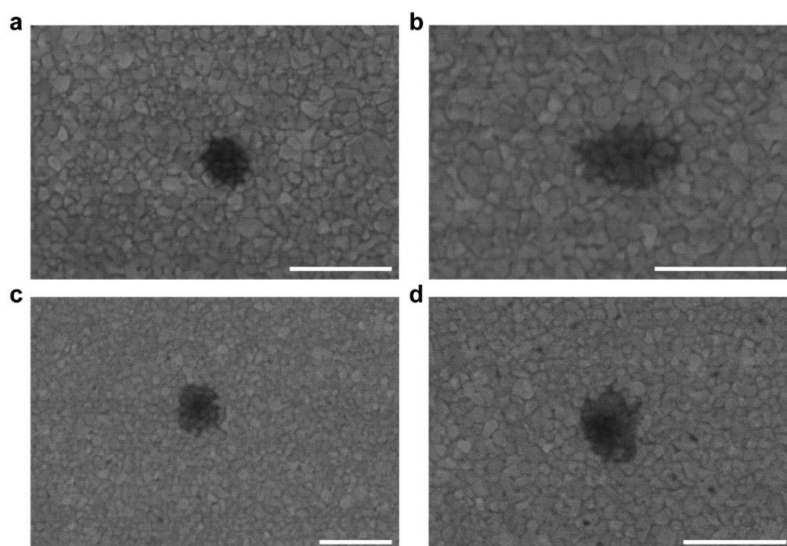


**Figure 2.12.** Scanning electron micrographs of patterned Pt features on Au-coated Si wafer, highlighting the high-resolution capability of ePPL. The black features indicate Pt particles with diameters ranging from  $\sim 210$  nm to 280 nm. Scale bars = 500 nm.

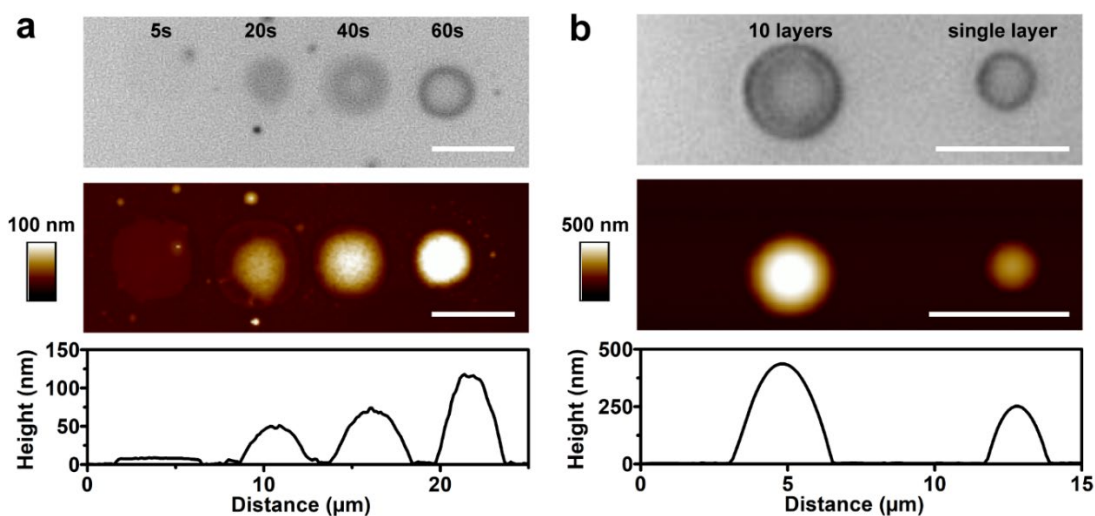


**Figure 2.13.** Feature dimensions are controlled by deposition time and layering. (a) Optical and AFM images of a pattern consisting of 4 Ni features where height was controlled by varying the deposition time. (b) Optical and AFM images of a pattern with 2 Ni features where size is controlled by depositing multiple layers of Ni, 60 s at a time. Features shown are 10 vs. 1 layer. Scale bars = 5  $\mu\text{m}$ .

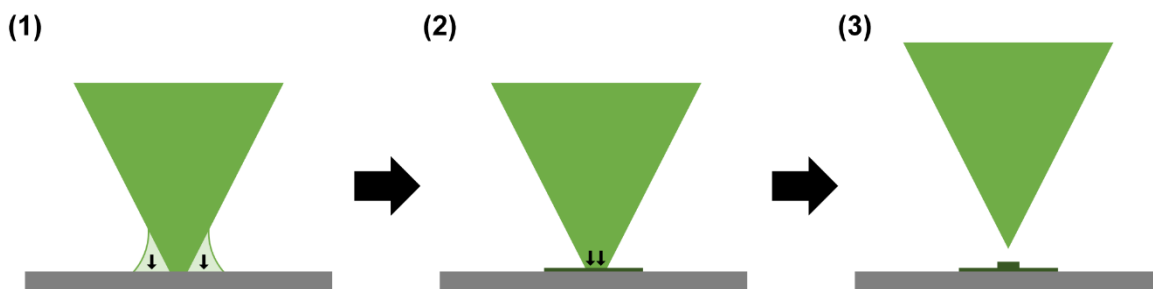


**Figure 2.14.** Schematic depicting the hypothesized mechanism of ePPL deposition. (1) First, metal reduction occurs preferentially from the meniscus that forms between the tip and the substrate upon contact. (2) Once ions are depleted from the meniscus, reduction occurs directly from the hydrogel, at the tip-substrate interface. (3) When the tip is lifted, the shape and size of the resulting structure corresponds to the shape of the tip-substrate interface, along with a very thin layer from the meniscus.

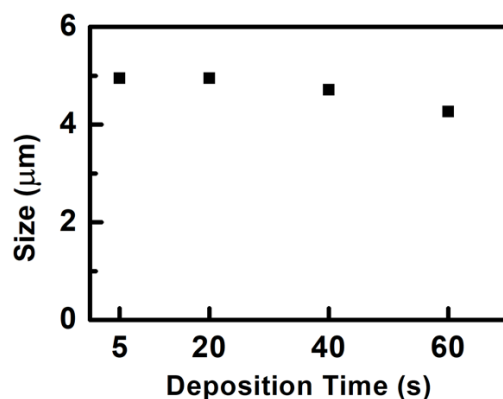


**Figure 2.15.** Feature size (diameter) measured as a function of deposition time, from features in Figure 3a. Horizontal feature size decreases slightly with increased deposition time because of the proposed mechanism wherein material deposits from a meniscus at first, followed by the deposition directly from the hydrogel pen, which is smaller than the meniscus (Figure S6). The height, nonetheless, is directly related to deposition time, as shown in Figure 2.13a.

Feature height can also be controlled by depositing metals in a layer-by-layer fashion. As evident in **Figure 2.13b** and **Figure 2.16**, the overall height of the Ni features increased with the number of layers, and a nearly two-fold increase in height was observed for a feature with 10 layers versus that of a single layer. The pen arrays were raised 100 nm in the z-direction after deposition of each layer. In this case, growth occurred in both the width and the height of the features, and

the height increase was not linear. The deposition occurred outwards over time because each layer was overlaid on top of each other; it is difficult to locate the exact height of the previously deposited feature, and the hydrogel pen is most likely acting as a physical barrier to increasing feature height. This may be overcome by more precise tuning of each layer height with corresponding z-movement. Nonetheless, by increasing the number of layers, we expect to achieve taller structures. Therefore, using this layer-by-layer method in combination with control over the deposition time, this ePPL technique can be used to generate 3D metallic structures of various sizes in a high-throughput manner.

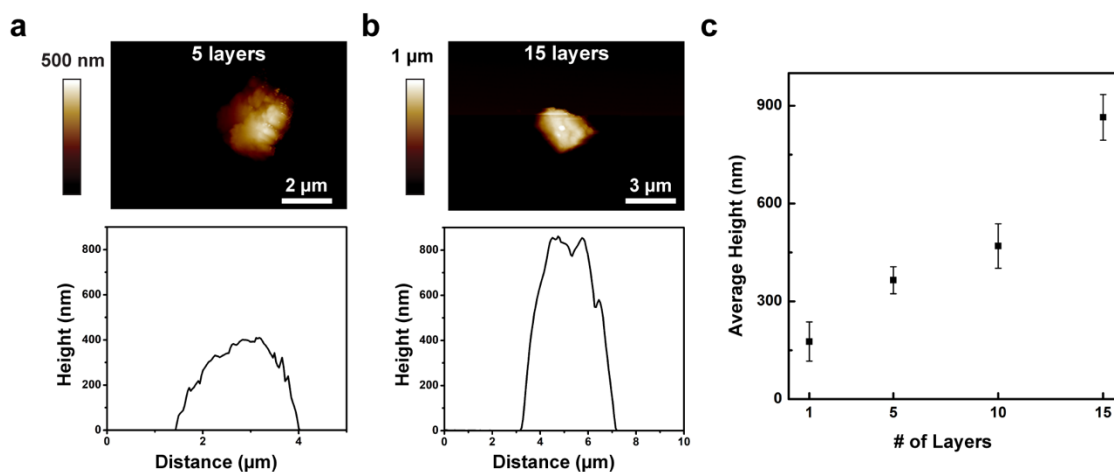


**Figure 2.16.** AFM height profile of the features with (a) 5 and (b) 15 layers. Each layer was printed at 60 s deposition time, and the pen array was lifted each time by 100 nm in z-direction. (c) A plot of average feature height versus number of printed layers. The height increases with increased number of layers, demonstrating the potential of ePPL technique towards 3D printing.

## 2.3. Experimental Details

### 2.3.1. Preparation of Metal Deposition Solutions

Electrolyte solution was prepared by combining  $\text{Ni}(\text{NO}_3)_2 \cdot 6\text{H}_2\text{O}$  (22 g, 76 mmol) and  $\text{Co}(\text{NO}_3)_2 \cdot 6\text{H}_2\text{O}$  (22 g, 7.6 mmol) in DI water (40 mL) for a 10:1 molar solution, and  $\text{Ni}(\text{NO}_3)_2 \cdot 6\text{H}_2\text{O}$  (22 g, 76 mmol) and  $\text{Co}(\text{NO}_3)_2 \cdot 6\text{H}_2\text{O}$  (22 g, 76 mmol) for a 1:1 molar solution.

### 2.3.2. *Fabrication of Pen Array Masters*

Masters were fabricated following procedures outlined in prior reports.<sup>7, 8</sup> In brief, a photoresist, Shipley S1805, was spin-coated on a silicon <100> wafer with a 5000 Å thermal oxide layer (NOVA Electronic Materials, LLC.). The wafer was soft baked at 115 °C for 80 s and cooled to room temperature. Using a mask aligner (Suss MJB4; Suss MicroTec), the wafer was UV-exposed to pattern  $15 \times 15 \mu\text{m}^2$  squares with a 30  $\mu\text{m}$  pitch; 30  $\mu\text{m}$  was used for all the data shown here, but arbitrary pitch distances up to 120  $\mu\text{m}$  have been successfully used as well. The patterns were developed in MF-319 developer for 60 s and rinsed with water. To remove the oxide layer before the etching step, the patterned Si wafer was immersed in a buffered HF solution. The patterns were then selectively etched in potassium hydroxide, which results in an array of inverted pyramids. Pyramids form due to an anisotropic etch which etches the <100> face of silicon ~74 times faster than the <111> face. The surface of the Si wafer was coated with fluorinated silane to facilitate the lift-off process of the hydrogels by making it superhydrophobic. Masters were cleaned periodically by sonicating for ~10 min in methanol, then rinsed with DI water and dried.

### 2.3.3. *Preparation of Polyacrylamide Hydrogel Pen Arrays*

A gel stock solution was prepared by dissolving acrylamide (2.38 g, 33 mmol) and bis-acrylamide (0.125 g, 0.811 mmol) powders in DI water (10 mL), which is enough to fabricate 1-2 pen arrays. The curing process was initiated by adding ammonium persulfate (91.8  $\mu\text{L}$ , 10 wt% in H<sub>2</sub>O) and tetramethylethylenediamine (9.18  $\mu\text{L}$ ) to the stock solution. All chemicals were purchased from Sigma-Aldrich, Inc.

#### 2.3.4. *Assembly of a Three Electrode Cell*

The setup of the three-electrode cell is shown in Figure 1b. The custom 3D electrochemical cell was designed using AutoCAD, and printed by Protolabs, Inc. In order to attach the acrylamide hydrogel to an indium tin oxide (ITO)-coated glass slide (Nanocs Inc.), the surface was functionalized with 3-(trimethoxysilyl)propyl acrylate (Sigma-Aldrich) in toluene (1:3 by volume) *via* vaporization in a sealed chamber. The functionalized ITO glass slide was attached to the top of the cell using double-sided tape. The cell was then placed directly onto a Si master, and the gel solution was poured into and around the cell through the reference electrode well at the corner of the cell. The gel was cured for no longer than 20 min at room temperature. The molded gel was removed from the master and soaked in a Ni, Pt, Ag, or Ni-Co metal deposition solution for at least 3 h or overnight in order for the metal salts to diffuse into the hydrogel. The entire cell was mounted to an AFM head for patterning, and the ITO substrate was clipped to a long wire, which served as the counter electrode. To create a functional working electrode (or a substrate), a long wire was connected *via* a flat alligator clip to a gold-coated glass slide. A Ag/AgCl electrode (BASi, Inc.) in NaCl (3.0 M) was used as a reference electrode and inserted gently into the well at the corner of the cell, along with additional metal deposition solution.

#### 2.3.5. *Patterning Procedure*

Before patterning, the pen arrays were aligned to the substrate using the optical alignment method described previously.<sup>7, 8</sup> In brief, the contact point of the pens at the four corners was compared, and the extent of contact area was used to determine the tilt angle of the stage. The stage was tilted until the array and the substrate were co-planar. Controlled potential electrolysis

(CPE) was performed to generate each feature. Once the tips were in contact with the substrate, a constant voltage was applied using a potentiostat (BASi EC Epsilon) for a given amount of time, depending on the metal used and thickness desired (**Table 2.2**). The speed of the piezo in the x-y and z directions was set to 0.1  $\mu\text{m/s}$ , allowing each pen tip to be replenished with metal ions before patterning the next feature.

**Table 2.2.** Applied voltages and minimum deposition times used for each metal deposition.

Metal	Applied Voltage (mV)	Minimum Deposition Time (s)
Ni	-950	20
Ag	-950	10
Pt	-500	10
Ni-Co	-550	60

### 2.3.6. Characterization of Patterns

The patterned images were observed using optical microscopy (Zeiss Axio Imager.M2m) and scanning electron microscopy (SEM; Hitachi SU8030). The height and surface roughness of the patterned features were analyzed using atomic force microscopy (AFM; Dimension Icon; Bruker). Using NCHR-50 cantilevers (Nanoworld), images were acquired in tapping mode at a scan rate between 0.10 – 0.99 Hz with a spring constant of 42 N/m. The imaging was performed at room temperature, and the collected data was analyzed using NanoScope Analysis software. Elemental analysis was performed *via* energy dispersive spectroscopy, fitted onto SEM (Hitachi SU8030) and X-ray photoelectron spectroscopy (XPS, Thermo Scientific EscaLab 250 Xi) to characterize the composition of the patterned features.

## 2.4. Conclusion

In summary, we reported a new massively parallel cantilever-free electrochemical patterning approach called ePPL. While we present the proof-of-concept ability to synthesize mono- and bi-metallic features, this approach should be extendable for patterning other single metal or alloy materials with control over size and composition across a single substrate. ePPL is promising due to its high-throughput, ease-of-use, and materials flexibility. Such a tool will be useful in creating combinatorial megalibraries of catalyst nanoparticles in order to systematically find an ideal catalyst for energy applications. In addition, ePPL may be used for precise deposition of conductive organic molecules, such as diazonium or conducting polymer structures for large-scale single-substrate bio-analytical studies. To the best of our knowledge, this is the first time that an electrochemical patterning approach has been developed in the framework of a cantilever-free system.

## Chapter 3

### Micropatterned Hydrogels for Controlled Cancer Cell Migration

Cancer cell migration is significantly influenced by the physical properties (e.g., mechanics, topography). In this chapter, a photo-responsive hydrogel is used as the substrate material to investigate how cells guide their movement in a complex, heterogeneous landscape while interpreting various physical factors, especially those with sizes on the sub-cellular length scale. Using a DMD system, the patterns of features on the sub-cellular to cellular length scale with different physical characteristics (i.e., stiffness, heights) are generated on the surface of the hydrogel, and the influence of the organization of these patterns on cellular migratory behavior is investigated. The size and spatial arrangement of hard (or stiff) and soft domains, more so than their topography, is found to have a significant impact on the migration speed. Using this approach, the maximum migration speed is observed on hydrogels with 10  $\mu\text{m}$  pattern sizes spaced 10  $\mu\text{m}$  apart. In this regime, the cells are confined and interact with both hard and soft regions at their periphery. Together, this study of cell-ECM interactions at the interface of hard and soft domains provides insights into how cancer cells sense and respond to their environment.

---

Materials in this chapter will appear in a subsequent publication:

**E. Oh**, B. Meckes, J. Chang, D. Shin, C. A. Mirkin. *In preparation*

### 3.1. Introduction

Cellular migration plays a fundamental role in numerous and diverse physiological and pathophysiological processes, including tissue homeostasis, tissue development and repair, immune defense, and tumor metastasis.<sup>52, 53</sup> As cells move, they probe and interact with the surrounding extracellular matrix (ECM), a complex network of proteins and polysaccharides organized hierarchically on the nano to macro length scales.<sup>10, 54</sup> It is well-established that the arrangement of chemical factors in the ECM regulates the rate and directionality of migration.<sup>10, 55-57</sup> Increasingly, however, the physical properties of the ECM, such as its stiffness and topography, have also been shown to be key external regulators of cell motility and migration.<sup>58-62</sup> Significantly, these external regulators have been found to promote cancer cell migration and infiltration into surrounding tissue, leading to metastasis.<sup>63-67</sup> Matrices with enhanced stiffness facilitate tumor growth and progression by elevating Rho-associated protein kinase activity and triggering the epithelial-mesenchymal transition.<sup>68</sup> During tumorigenesis, the ECM undergoes dynamic physical remodeling, which causes topographical changes that involve reorganizing and aligning collagen fibers to create passageways for cancer cell migration.<sup>69</sup>

Given the emerging understanding of ECM mechanics and topography in the context of cell behavior, novel experimental approaches and strategies have been developed to delineate the effects of the different physical properties of the ECM on cancer cell migration within controlled environments.<sup>70</sup> To understand how substrate rigidity impacts cell migration, polymeric materials with physiologically relevant stiffness (e.g., composed of polyacrylamide, collagen, polyethylene glycol, and gelatin) have been synthesized (matrix stiffnesses can be modulated by tuning cross-linking densities).<sup>71-77</sup> Using these hydrogel systems, it has been shown that cancer cell motility is

dependent on ECM stiffness and that there is an optimal stiffness that maximizes cell speed.<sup>71, 78</sup> Cancer cells also respond to stiffness gradients, displaying durotaxis and preferentially moving towards stiffer regions.<sup>79, 80</sup> In addition, polymers have also been used to fabricate topographical features, including micro-grooves, lines, and ridges, that mimic aligned ECM fibers known to polarize cell migration; these substrates were used to probe the physical mechanisms that govern directional migration, a key contributor to disease progression.<sup>81-83</sup> These topographical features facilitate cancer cell invasion by regulating the direction of migration *via* contact guidance, a phenomenon where cells orient and elongate along the aligned fibrillar structures.<sup>84, 85</sup>

Researchers have mainly investigated the independent contributions of stiffness and topographical variations on cancer cell migration, and studies were performed with mostly homogeneous systems or at macroscopic levels, failing to reflect the complexity of physiological tissues. The tumor microenvironment, in particular, is more mechanically heterogeneous compared to normal tissues due to localized ECM stiffening. Indeed, cancer cells exist in significantly more complex environments that are commonly reproduced artificially, and they are composed of biophysical cues in the form of mismatched mechanical and topographical features that are distributed across the sub-cellular to macroscopic size regimes. It is not known how cancer cells dynamically perceive and distinguish local sub-cellular differences in various physical cues to guide their movement or how stiffness and topography are related and affect migration pathway in a heterogeneous landscape. Therefore, developing a better understanding of how heterogeneous physical properties at the sub-cellular level impact cancer cell migration could permit the identification of key factors that contribute to metastasis.

Here, photo-responsive hydrogel matrices were synthesized bearing photo-defined mechanical and topographical heterogeneities. Using these photopatterned hydrogels, the ability of glioma derived U87-cells to recognize and differentiate the physical attributes of the underlying substrate and use such encoded cues to modulate their behavior was investigated. A nearly two-fold greater migration speed was observed when cells were seeded on hydrogels with 10  $\mu\text{m}$  soft features with 10  $\mu\text{m}$  spacings compared to the analogous unpatterned control substrates. Significantly, this effect was found to stem from self-selective confinement of the cells within the stiff areas between patterns. Importantly, mechanical features promoted greater motility in comparison to topographical features with sizes and spacings on the same length scale. The cells tended to migrate within the stiffer regions and so could be polarized in certain directions by controlling the arrangement of the soft domains (speed remained the same). These findings not only deepen our understanding of the fundamental role of cell-ECM interactions in cancer migration and confinement but can also be applied toward other cell lines to ultimately improve cellular scaffold designs useful in tissue engineering and regenerative medicine.

### 3.2. Fabrication and Characterization of Patterned Hydrogel Matrices

Hydrogels with spatially tunable physical properties were synthesized (**Figure 3.1a**). Briefly, a polyethylene glycol (PEG) photodegradable diacrylate (PEGdiPDA) cross-linker was prepared following previously reported protocols (**Figure 3.2**).<sup>72, 86, 87</sup> Then, the PEGdiPDA was mixed with a PEG monoacrylate (PEGA) at a 1:20 molar ratio. To promote cell adhesion, a peptide with the adhesion-promoting amino acid sequence, arginine-glycine-and aspartic acid (RGD), containing an acrylate group was added. Hydrogels with defined thickness were then polymerized by injecting

the polymer and initiator between glass slides separated by a rubber spacer. One of the glass slides was functionalized with an acrylate monolayer facilitating hydrogel adhesion during the curing process.

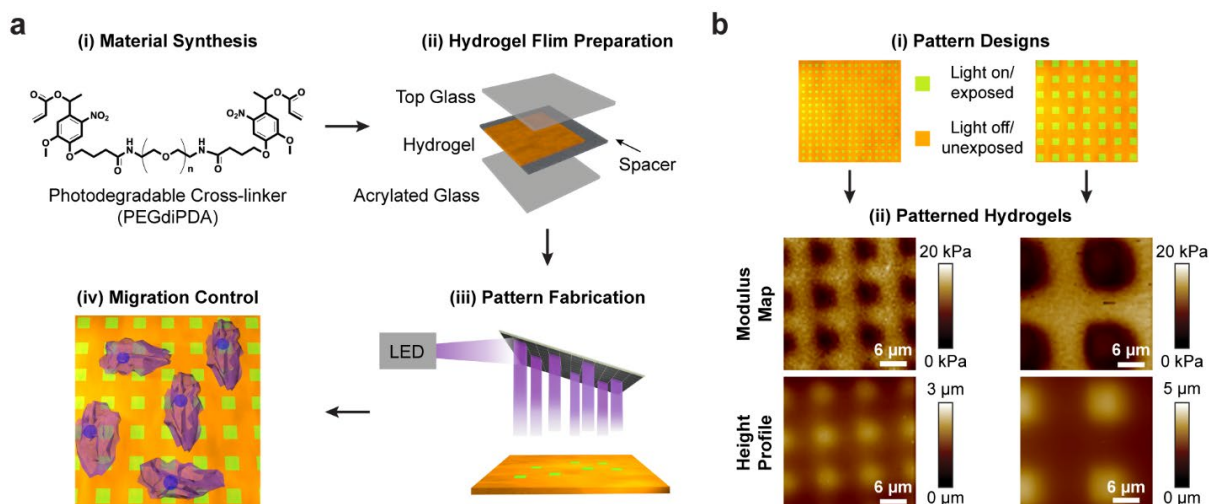


**Figure 3.1.** a) Illustration of the fabrication process of a cellular matrix with heterogeneous stiffness and topography at the sub-cellular to cellular level: (i) synthesis of photodegradable cross-linker, PEGdiPDA, (ii) hydrogel film formation using two glass slides spaced apart by a rubber spacer, (iii) pattern generation using the DMD system with 405-nm LED, and (iv) cellular analysis and control with patterned hydrogels. b) Schematic examples of pattern designs, where the green areas were locally exposed to light, (i) and representative AFM images of patterned hydrogels (ii) of 5  $\mu\text{m}$ -edge length square patterns with 5  $\mu\text{m}$  interpattern spacing (left) and 10  $\mu\text{m}$ -edge length square patterns with 10  $\mu\text{m}$  interpattern spacing (right).

To encode stiffness and topographic variances on and within these hydrogel matrices, the hydrogels were exposed to 405-nm light using a digital micromirror device (DMD). Upon exposure, the nitrobenzyl ether group of the PEGdiPDA was cleaved, decreasing the cross-linking density and softening the illuminated regions of the gel as a result. The illumination of the substrate was precisely controlled by actuating the individual mirrors, and the resulting patterned gels contained well-defined ‘soft’ and ‘hard’ (stiff) domains. Atomic force microscopy (AFM) revealed that the ‘soft’ areas exposed to light were taller than the ‘stiff’ areas, suggesting that increased

swelling occurred in regions with lower cross-linking density. Importantly, in this hydrogel system, only a minimal amount of RGD peptide ligand is likely cleaved upon exposure to light; a previous study reported that 95 % of RGD peptide ligands remain attached with irradiation.<sup>87</sup>

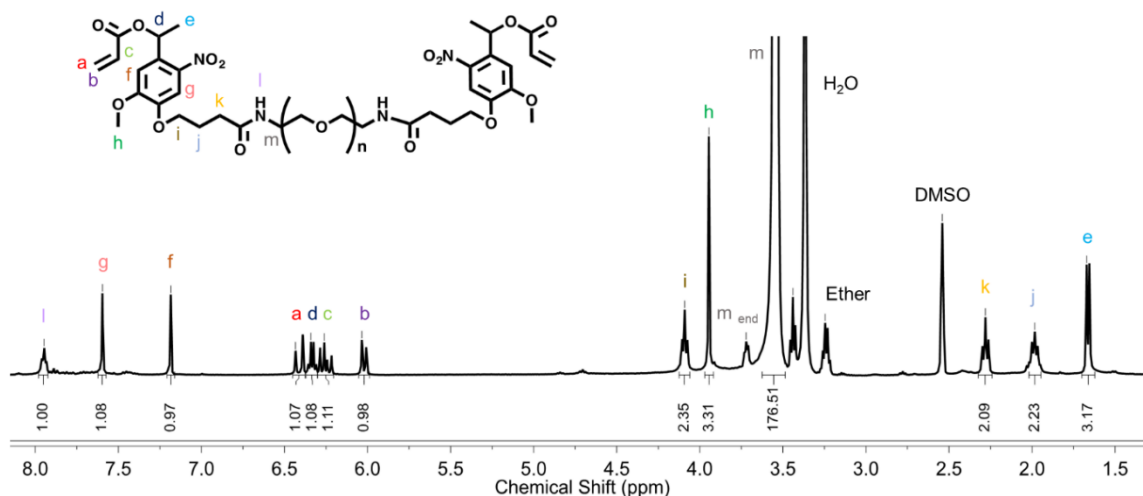


**Figure 3.2.** <sup>1</sup>H NMR spectrum of a photodegradable cross-linker (PEGdiPDA). The peaks are color-coded and labeled with letters a – m with the protons in the molecule as shown in the inset. Solvent impurities are also indicated where H<sub>2</sub>O and DMSO are used for water and dimethylsulfoxide, respectively. All the peaks matched those of the reported spectrum.

To study the influence of the size and spatial distribution of these physical features on cancer cell migration, patterns of squares ranging in edge length from 5 μm (sub-cellular) to 50 μm (larger than a single cell) were designed. These sizes were chosen because they are on the same length scale as the microgrooves or microchannel-like tracks that exist in the native microenvironment.<sup>67, 74, 88</sup> For each substrate, the inter-feature spacing was the same as the edge length of the features so that a constant ratio of the soft to stiff area was maintained from sample to sample (e.g., 5 × 5 μm<sup>2</sup> patterns spaced 5 μm apart, 10 × 10 μm<sup>2</sup> patterns spaced 10 μm apart, and so on). The stiffness of the domains was modulated by toggling the energy dose of the light

(Figure 3.3), and the values investigated, which range from 6 to 30 kPa, were designed to be within the range of the physiological stiffness of many soft tissues in the human body, like the brain (both normal and tumor).<sup>73, 89, 90</sup> The stiffness and topographic heterogeneity of these patterned substrates were confirmed and analyzed using AFM (Figure 3.1b and Figure 3.4).

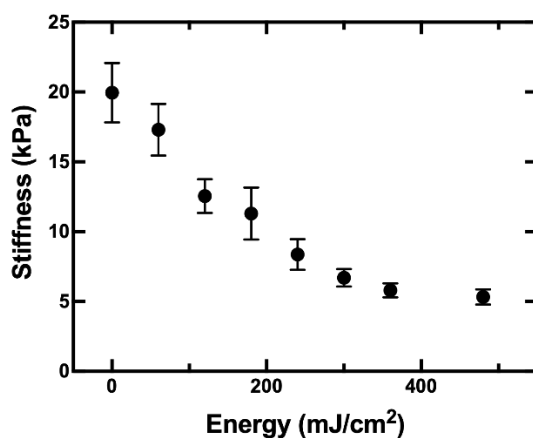


**Figure 3.3.** A plot of substrate stiffness versus input energy. As input energy increases, the substrate stiffness decreases.

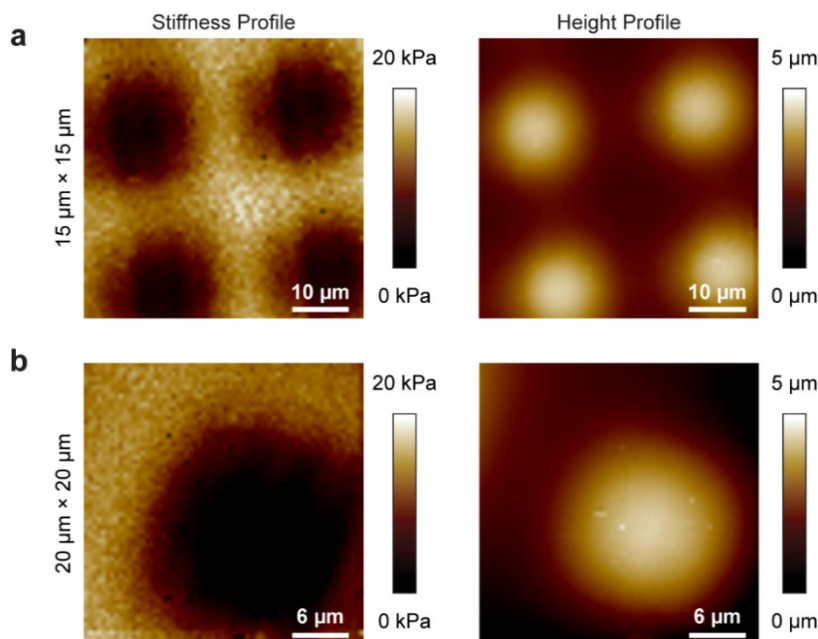


**Figure 3.4.** AFM images of the hydrogel films with  $15 \times 15 \mu\text{m}^2$  (a) and  $20 \times 20 \mu\text{m}^2$  (b) square patterns. Left: Elasticity map with mechanical variation encoded using DMD arrays. The dark

brown regions indicate an area that was exposed to light, degraded, and became softer as a result. Right: The height profiles of the respective substrates.

### 3.3. Cellular Migratory Behavior on the Patterned Hydrogels

In order to assess how mechanical heterogeneity modulates cancer cell migration, glioblastoma U87-MG cells were used. These cells are known to exhibit both durotaxis and contact guidance that contribute to disease progression. First, to determine if the hydrogels supported cell survival, the viability of the cells on hydrogels with  $15 \times 15 \mu\text{m}^2$  square patterns was examined using a live/dead fluorescence assay. After three days on the hydrogels, the cells were fixed, stained, and imaged with a confocal microscope. This analysis revealed that the cells on the substrate were viable (**Figure 3.5**).

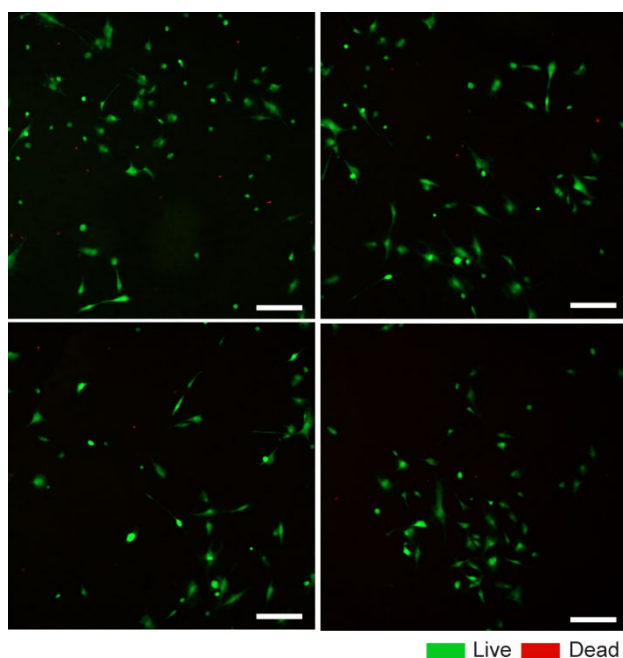


**Figure 3.5.** Live/dead fluorescence assay of U87 glioma cells seeded and grown on patterned hydrogels on day three. Live and dead cells are indicated in green and red, respectively. Scale bars = 200  $\mu\text{m}$ .

Next, to assess how the physical properties of the substrate affected cell migration, the cells were stained with Cell Tracker Orange and seeded onto the surface of patterned and unpatterned hydrogels (**Figure 3.6a**). Note that Cell Tracker Orange was used because it can be imaged using an excitation wavelength (548 nm), which does not cause hydrogel degradation during live-cell imaging; this excitation wavelength does not readily create reactive oxygen species (ROS) or damage DNA. To start, the behavior of the cells on the unpatterned, mechanically homogeneous hydrogels without programmed topographical features (controls) with a range of stiffnesses ( $\sim 6$  kPa,  $\sim 16$  kPa, and  $\sim 30$  kPa) were evaluated. After one day of incubation on the respective hydrogels, the movements of the cells were recorded using a confocal microscope for at least 2 h with 5 min intervals between each image frame. Here, the migration speed was defined as the average speed of the cells determined by the total distance traveled over the total time. The measured average speed of the cells on these substrates was the same within error ( $0.69 \pm 0.05$   $\mu\text{m}/\text{min}$  for  $\sim 16$  kPa and  $0.63 \pm 0.06$   $\mu\text{m}/\text{min}$  for both  $\sim 6$  kPa and  $\sim 30$  kPa). Thus, overall stiffnesses in this range did not impact the migration speed of the cells. Indeed, the measured values corresponded to the previously reported average speed of U87 cells, which typically range from 0.5 to 0.6  $\mu\text{m}/\text{min}$ .<sup>75, 79, 80</sup>

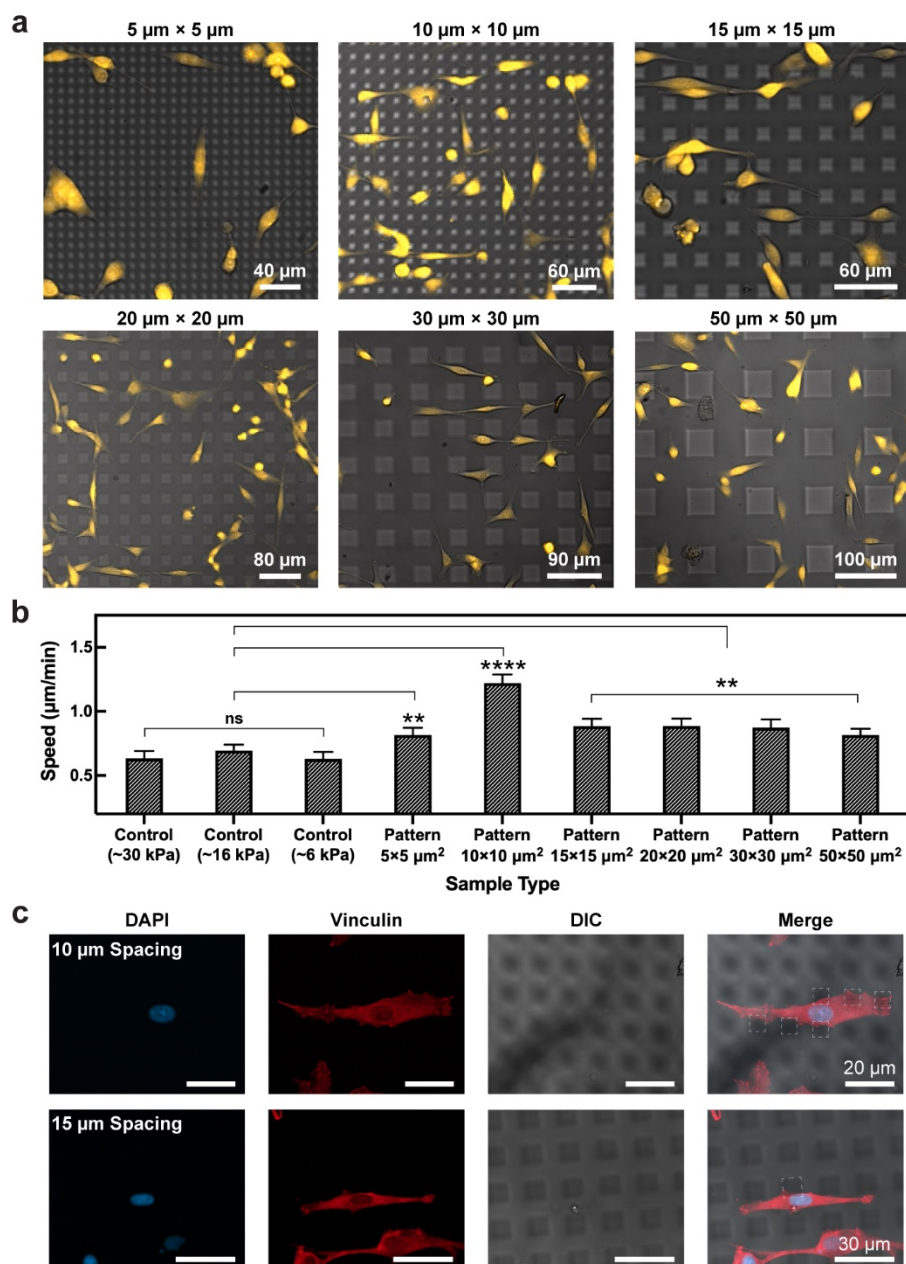


**Figure 3.6.** a) Bright-field images overlaid with fluorescence micrographs of U87 cells labeled with Cell Tracker Orange on patterned hydrogels. The edge length of the square patterns ranges from  $5\ \mu\text{m}$  to  $50\ \mu\text{m}$  with the same respective interpattern spacings. b) A plot delineating the effect of pattern size and spacing on the migration speed of cells, where controls are the bulk substrates without patterns (mean  $\pm$  SE; \*\*\*\* $p \leq 0.0001$ , \*\* $p \leq 0.01$ , ns  $p > 0.05$  based on one-way ANOVA;  $n \geq 3$  with over 30 cells analyzed for each sample). c) Confocal images of a single cell confined between  $10\ \mu\text{m} \times 10\ \mu\text{m}$  (top) and  $15\ \mu\text{m} \times 15\ \mu\text{m}$  (bottom) patterns. The nuclei (panel 1) and vinculin (panel 2) in the cells are fluorescently labeled, and their representative images are overlaid with differential interference contrast (DIC) images (panel 3), which are shown in panel 4.

Substrates bearing domains of a range of sizes ( $5 \times 5 \mu\text{m}^2$ ,  $10 \times 10 \mu\text{m}^2$ ,  $15 \times 15 \mu\text{m}^2$ ,  $20 \times 20 \mu\text{m}^2$ ,  $30 \times 30 \mu\text{m}^2$ , and  $50 \times 50 \mu\text{m}^2$ ) and spacings ( $5 \mu\text{m}$ ,  $10 \mu\text{m}$ ,  $15 \mu\text{m}$ ,  $20 \mu\text{m}$ ,  $30 \mu\text{m}$ , and  $50 \mu\text{m}$ , respectively) were also investigated; the patterns had average stiffnesses less than and heights taller than the unpatterned areas (stiffness =  $9 \pm 2 \text{ kPa}$  vs.  $17 \pm 4 \text{ kPa}$ ; height =  $2 \pm 1 \mu\text{m}$ ) (**Figure 3.1b** and **Figure 3.4**). Analysis of time-lapse images (**Figure 3.6a**) revealed that the U87 cells move faster when they are on the patterned substrates than when they are on any of the homogenous substrates ( $\sim 6$ ,  $\sim 16$ , or  $\sim 30 \text{ kPa}$ ) (**Figure 3.6b**), which supports the notion that cancer cells recognize and respond to matrix topography and stiffness heterogeneity presented at sub-cellular to cellular length scales since they encounter both soft and hard regimes that support spreading and movement. Indeed, this result is in line with the literature; the mechanical properties of the matrix are known to influence the assembly and disassembly of focal adhesions—these adhesions tend to be less stable on soft matrices as compared to hard matrices.<sup>71, 78, 91</sup> To test if cells were preferentially forming focal adhesions with the stiffer domains, a vinculin stain was performed (vinculin is a focal adhesion-associated protein). Vinculin was found to be located at the periphery and the leading edges of the cells (**Figure 3.6c**). For the  $5 \times 5 \mu\text{m}^2$  and  $10 \times 10 \mu\text{m}^2$  patterns, the cells interacted with the interfaces between the soft and hard regions (dotted lines, **Figure 3.6c**). For larger pattern sizes (i.e.,  $20 \times 20 \mu\text{m}^2$ ,  $30 \times 30 \mu\text{m}^2$ , and  $50 \times 50 \mu\text{m}^2$ ), the cells interacted primarily with the stiffer regions between the patterns, which leads to hyper-stabilized focal adhesions and restricts mobility.

As the pattern size increased, the cells moved within the stiffer regions surrounding the patterns, as expected based on durotaxis. The cells were confined between the patterns, especially on the  $10 \times 10 \mu\text{m}^2$  and  $15 \times 15 \mu\text{m}^2$  patterned substrates, where their interpattern spacings were

highly correlated with the length of the cell's nucleus ( $9.6 \pm 0.2 \mu\text{m}$ ) and minor axis ( $14.8 \pm 0.1 \mu\text{m}$ ). An increased cellular motility is expected with increasing confinement<sup>67, 71, 74</sup>, and the maximum speed was observed on the  $10 \times 10 \mu\text{m}^2$  patterned substrates with  $10 \mu\text{m}$  spacing ( $1.24 \pm 0.05 \mu\text{m}/\text{min}$ ). Slower speeds were observed when the spacing ( $5 \mu\text{m}$ ) was smaller than the nucleus of the cell, and the cells could span multiple soft domains and were less confined ( $0.82 \pm 0.06 \mu\text{m}/\text{min}$ ). Slower speeds were also observed for the cells on the substrates with the larger pattern sizes and interpattern spacings (feature edge length and spacing larger than  $10 \mu\text{m}$ ) because stable focal adhesions were formed (average speed of  $0.866 \pm 0.016 \mu\text{m}/\text{min}$ ). Based on these observations, the results suggest that the nearly two-fold increase in cell speed observed on the  $10 \times 10 \mu\text{m}^2$  patterned substrates compared to that on the unpatterned control substrates ( $0.652 \pm 0.005 \mu\text{m}/\text{min}$ ) is due to a synergistic effect of stiffness heterogeneity and confinement.

Next, cell migration was explored on the  $10 \times 10 \mu\text{m}^2$  patterns with similar patterned domain stiffness and increased unpatterned domain stiffness ( $\sim 26 \text{ kPa}$  vs.  $\sim 17 \text{ kPa}$ ;  $\sim 1.5$ -fold more than for the experiment above) (**Figure 3.7**). The cells seeded on these substrates with stiffer backgrounds moved at the same speed within error ( $1.17 \pm 0.11 \mu\text{m}/\text{min}$ ) as cells on the patterns with less stiff unpatterned areas ( $1.24 \pm 0.05 \mu\text{m}/\text{min}$ ). This observation indicates that the interpattern spacing affects cell motility more than the absolute difference in stiffness between the patterned and unpatterned areas.

Additionally, how various pattern sizes affect cell morphology (in terms of size, circularity, and aspect ratio) was examined (**Figure 3.8**). The pattern size did not affect the average area of the cells, which was similar across all samples (average value of  $332 \pm 3 \mu\text{m}^2$ ), including the unpatterned control substrates. However, cells on uniformly soft substrates ( $\sim 5 \text{ kPa}$ ) and those on

substrates with 5  $\mu\text{m}$  pattern sizes showed decreased aspect ratios (and increased circularity) compared to cells grown on substrates with pattern sizes 10  $\mu\text{m}$  or greater; cells on uniformly hard substrates ( $\sim 16$  and  $\sim 30$  kPa) were slightly more elongated. In particular, cells on 10  $\mu\text{m}$  square patterns (the most confined) were the most elongated as indicated by their aspect ratio ( $2.18 \pm 0.09$ ) and the circularity ( $0.700 \pm 0.016$ ) values, which was the highest and lowest observed, respectively (Figure 3.8c and d). This observation is also congruent with previous results where cells confined in narrower channels and grooves were much more elongated than those grown on wider spaces.<sup>71</sup>

74, 82

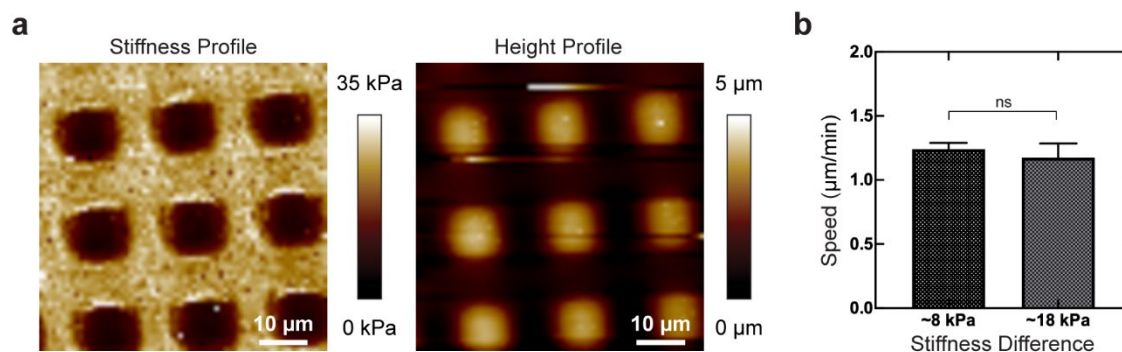


**Figure 3.7.** Patterned hydrogels with increased nominal background stiffness. a) Representative stiffness (left) and height (right) profiles of a  $10 \times 10 \mu\text{m}^2$  square patterned substrate. b) Comparison of the migration speed of cells on a substrate with stiffness difference of either 8 kPa or 18 kPa between the patterned and unpatterned areas (mean  $\pm$  SE; ns  $p > 0.05$  based on one-way ANOVA; over 30 cells analyzed).

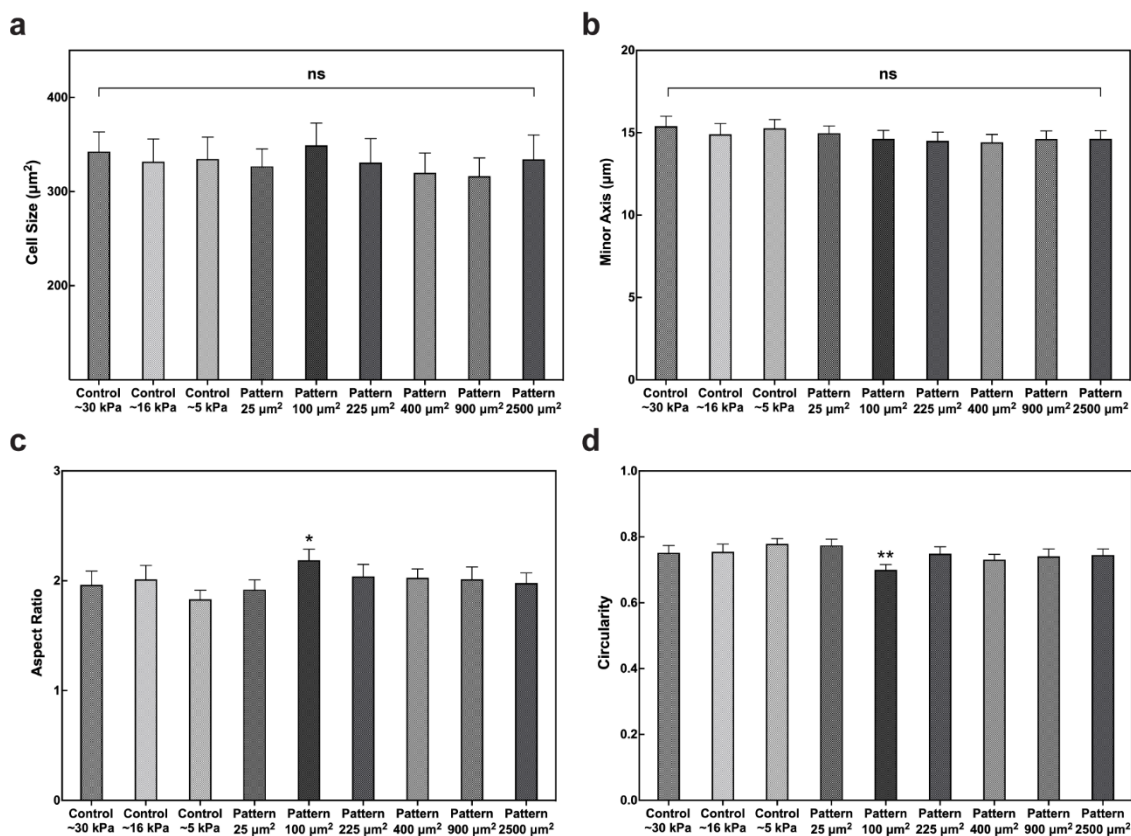


**Figure 3.8.** Impact of pattern size on cell morphology: a) cell sizes, b) minor axis, c) aspect ratio, and d) circularity (mean  $\pm$  SE; \*\* $p \leq 0.01$ , \* $p \leq 0.05$  and ns  $p > 0.05$  based on one-way ANOVA;  $n \geq 3$  with over 50 cells analyzed for each sample).

### 3.4. Deconvolution of Confinement and Stiffness

To confirm that the observed confinement in our system was due to mechanical and not topographical effects, hydrogel matrices with uniform stiffness containing topographical features with heights similar to those observed in our photopatterned samples were prepared as described (Experimental Section; **Figure 3.9**). Specifically, substrates with  $5 \times 5 \mu\text{m}^2$  and  $10 \times 10 \mu\text{m}^2$  square features with heights of  $1.93 \pm 0.23 \mu\text{m}$  and  $2.57 \pm 0.24 \mu\text{m}$ , respectively, were fabricated at various stiffnesses ranging from  $\sim 4$  to 35 kPa (**Figure 3.10** and **Figure 3.11**). To reiterate, on a given substrate, the taller square features have the same stiffness as the surrounding areas. A

significant increase in the migration speed of the cells was not observed on these substrates, where topography and not stiffness was encoded, compared to the control samples where neither topography nor stiffness was encoded. This result suggests that the height variation here is not a major factor in determining focal adhesion assembly and disassembly.

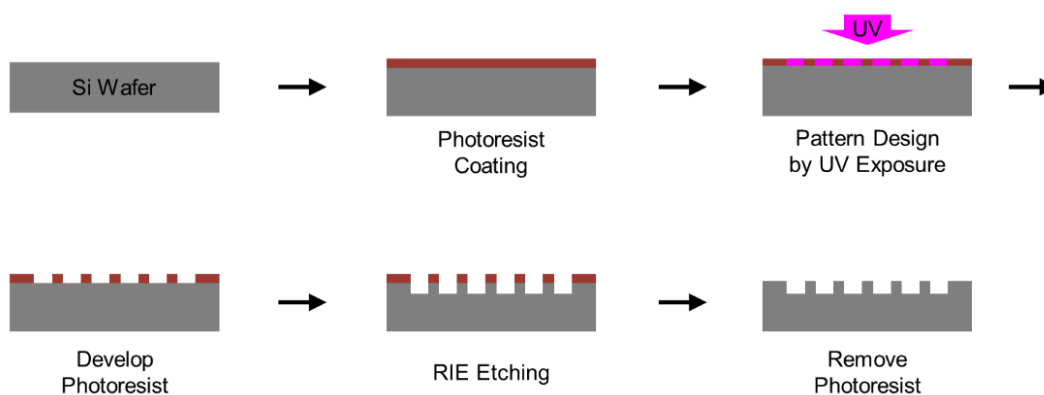


**Figure 3.9.** Steps for making topographical templates for hydrogel films. 1) S1805 photoresist (MicroChem Inc.) was spincast on a Si wafer with a 500-nm thermal oxide layer (Nova Electronic Materials) at a spin speed of 500 rpm for 5 s and at 4,000 rpm for 40 s. It was then baked at 115 °C for 80 s. 2) The photoresist-coated Si wafer was exposed with a 405-nm laser for 60 s using a maskless aligner (Heidelberg MLA150). The desired patterns were pre-designed *via* AutoCAD software. 3) The pattern was developed in MF-319 developer for 60 s. 4) Height differences were selectively defined by deep reactive ion etching (DRIE, STS LpX Pegasus) with a 3kW RF Generator. The topological mold was made by alternately flowing  $C_4F_8$  (deep) and  $SF_6$  and  $O_2$  (etch) gas. The templates were etched for 6-8 mins, cycling with a depth for 2 s and an etch for 3 s. 5) The residual photoresist layer was removed using acetone.

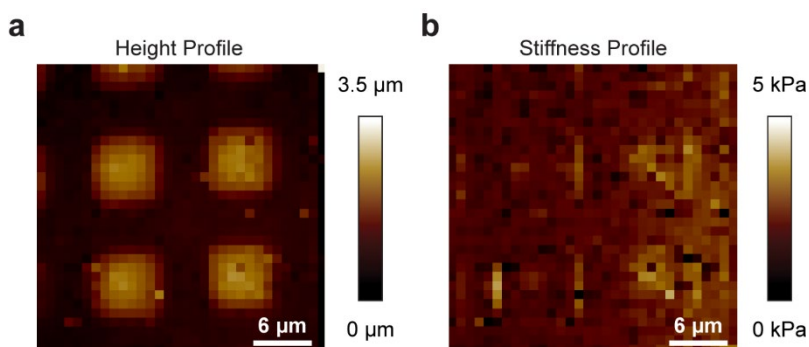


**Figure 3.10.** AFM analysis of a hydrogel film with topographical features of uniform stiffness. a) Height profile of  $5 \times 5 \mu m^2$  square patterns spaced 5  $\mu m$  apart, and b) Stiffness map of the respective sample.

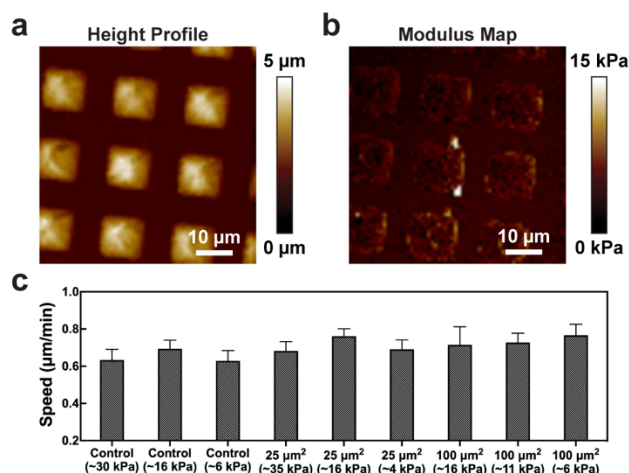


**Figure 3.11.** a) Height profile of the topographically patterned hydrogels. b) Representative Young's modulus map, depicting the uniform stiffness of the hydrogel. c) Effect of topographical variations on the migration speed of cells. Control samples are hydrogels without height features. Over 30 cells were analyzed for each condition.

To continue to quantify the effect of topography, the number of cells confined between the  $10 \times 10 \mu\text{m}^2$  square patterns were compared for samples with only topographical versus both topographical and stiffness heterogeneity. The percentage of cells residing between the patterns (vs. the total cell count in a given area) was less for the substrates with just topographical as compared to mechanical and topographical patterning (31 % vs. 50 %, respectively; **Figure 3.12**), indicating that the topographical features do not influence durotaxis and confinement as strongly as the mechanical features. The cells were more uniformly distributed across the substrate with only topographical patterns, and the cells showed a more rounded morphology, as confirmed by the higher circularity ratio ( $0.700 \pm 0.016$  (topography and stiffness) to  $0.735 \pm 0.016$  (topography only)). In other words, the cells interact more with the elevated domains when there is no stiffness mismatch compared to when there is. Based on these results, we concluded that mechanical properties have a greater impact on cellular confinement and motility in this system. The

confinement effect observed on photopatterned substrates is, therefore, mostly driven by durotaxis and the cells' strong tendency to move towards stiffer regions.

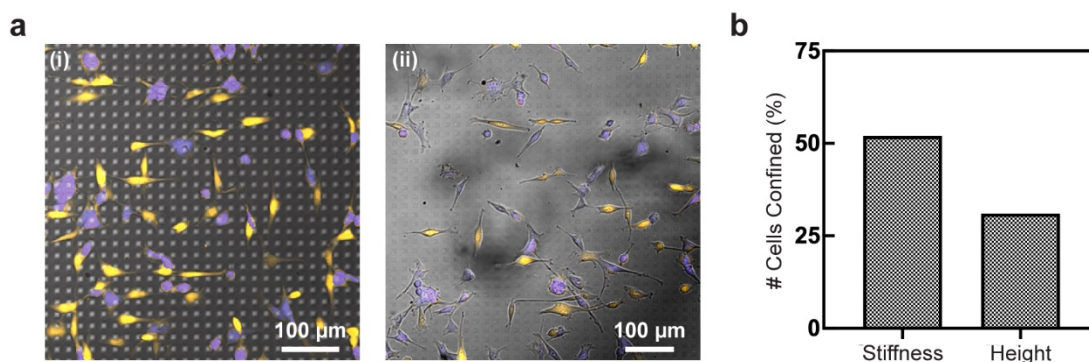


**Figure 3.12.** Durotactic migratory behavior of cells. a) U87 cells cultured on topographically encoded substrates with heterogeneous (i) and uniform stiffness (ii). Confined cells are indicated in yellow. b) A plot representing the percentage of cells confined between the patterns as a function of the total cell count at each sample type.

### 3.5. Cell Alignment Control *via* Stiffness Heterogeneity

Based on the durotaxis behavior of the U87 glioblastoma cells on the patterned substrates, we hypothesized that the spatial arrangement of the soft and hard regions could be used to polarize cells directionally. To test this hypothesis, an anisotropic pattern where  $10 \times 10 \mu\text{m}^2$  square patterns are packed closer together in only one direction was designed (**Figure 3.13**). Specifically, soft  $10 \mu\text{m}$ -square domains were spaced  $5 \mu\text{m}$  apart on the arbitrarily labeled x-axis and  $10 \mu\text{m}$  apart in the other direction (y-axis). In comparison to the isotropic sample where the  $10 \mu\text{m}$ -square patterns are distributed with equal spacing in both the x- and y-directions, the anisotropic substrate contained more soft spots along the x-axis (**Figure 3.14** and **Figure 3.15a**). When cells navigated through the anisotropic patterns, they expressed more rounded morphologies when they were interacting with the softer regions, as expected (**Figure 3.15b**). The retraction of the lamellipodia also was observed. On the other hand, when cells moved into the stiffer regions, the protrusions of

lamellipodia were observed that resulted in elongation of the cell bodies. Eventually, the cells were enriched in the stiffer areas, aligned against the boundary of the soft and stiff regions. Compared to those on isotropic substrates, cells on the anisotropic samples showed a strong biased elongation along the 10- $\mu\text{m}$  wide stiffer channels in the direction of the x-axis (**Figure 3.15d** and **Figure 3.16**) and had a higher aspect ratio of  $2.42 \pm 0.09$  (vs.  $2.18 \pm 0.09$ ) and lower circularity value of  $0.664 \pm 0.015$  (vs.  $0.700 \pm 0.016$ ) (**Table 3.1**). Their average speed of  $1.22 \pm 0.05 \mu\text{m}/\text{min}$ , however, did not significantly change from that of the isotropic substrate. It was nearly two-fold higher than that of the cells on control substrates with no patterns (**Figure 3.15c**).

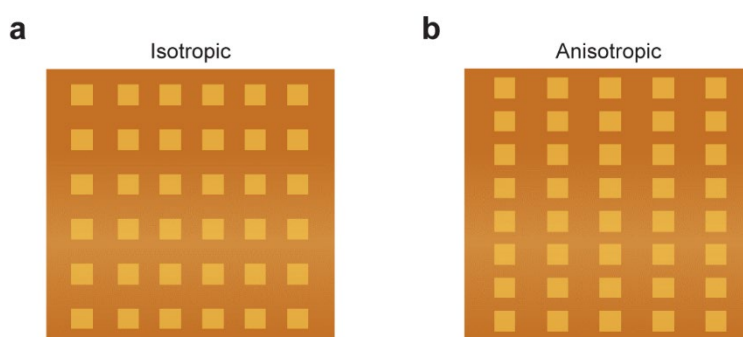


**Figure 3.13.** Schematic diagram of isotropically (a) and anisotropically (b) patterned substrates. For an isotropic sample, square patterns are equally distributed in both x and y directions whereas they are more closely spaced in one direction for an anisotropic sample.

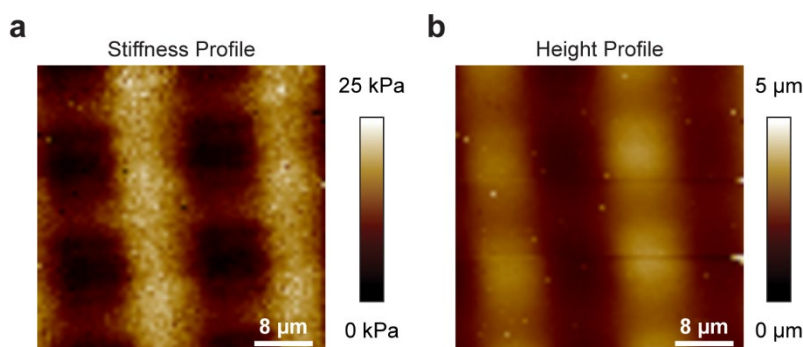


**Figure 3.14.** Characterization of the anisotropically patterned hydrogel using AFM. Darker brown regions in the stiffness profile (a) indicate soft spots where light has been exposed and caused swelling, which also correspond to lighter regions in the height profile (b).

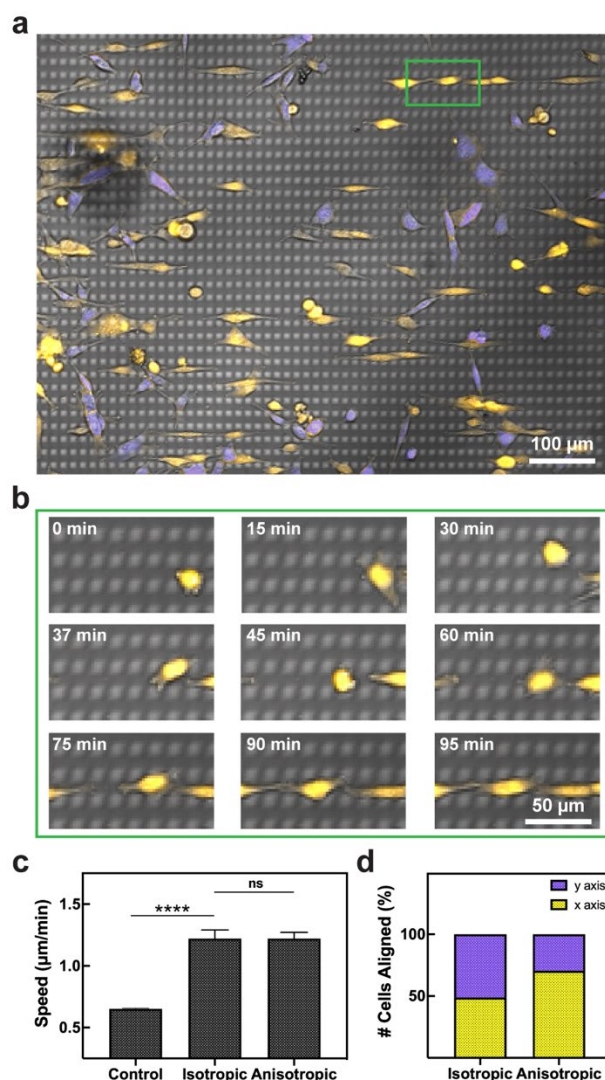


**Figure 3.15.** a) Fluorescence image of cells seeded on a hydrogel substrate patterned in an anisotropic manner ( $10 \times 10 \mu\text{m}^2$  patterns spaced  $5 \mu\text{m}$  and  $10 \mu\text{m}$  apart respectively in x- and y-direction). The image is overlaid with a bright-field micrograph. The cells aligned to the x-axis (horizontal direction) are indicated in yellow and those to the y-axis in purple. b) Magnified images of a cell indicated by the highlighted area in (a) at different time points, showing the cell alignment driven by durotaxis. c) The migration speed of cells grown on either control (no patterns), isotropic, or anisotropic substrates (mean  $\pm$  SE; \*\*\*\* $p \leq 0.0001$  and ns  $p > 0.05$  based on one-way ANOVA;  $n \geq 2$  with over 30 cells analyzed for each sample). d) The percentage of cells aligned in the x-axis and y-axis for isotropic and anisotropic patterns. The confocal image for the isotropic sample is shown in **Figure 3.16**.

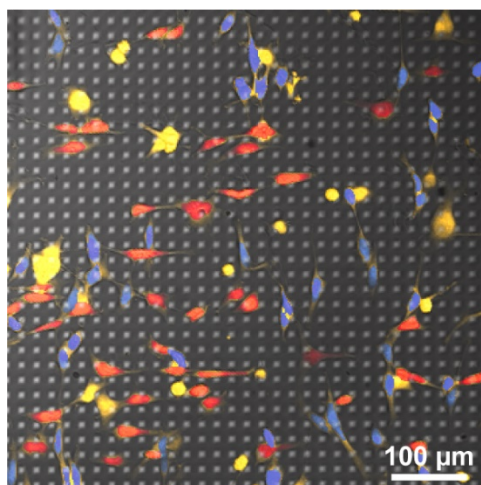


**Figure 3.16.** Fluorescence image of cells seeded and grown on an isotropically patterned hydrogel. The cells aligned in the x-axis are labeled in red and those aligned in the y-axis are blue, and the respective cell count is 45 and 47, respectively.

**Table 3.1.** Aspect ratio, circularity value, and directionality ratio of the cells seeded on control, isotropic, and anisotropic samples. Control samples are substrates with uniform stiffness ( $\sim 6$ ,  $\sim 16$ , and  $\sim 30$  kPa) without stiffness and height heterogeneities.

Sample	Aspect ratio	Circularity	Directionality ratio (r)
Control	$1.94 \pm 0.05$	$0.762 \pm 0.009$	$0.46 \pm 0.04$
Isotropic	$2.18 \pm 0.09$	$0.700 \pm 0.016$	$0.54 \pm 0.06$
Anisotropic	$2.42 \pm 0.09$	$0.664 \pm 0.015$	$0.61 \pm 0.05$

To understand the impact of this anisotropy on the directionality of the migration, the ratio of net displacement ( $r$ ) to the total migration trajectory was measured for isotropic, anisotropic, and control samples where a higher ratio indicates more directed movement (**Table 3.1**).<sup>74, 92</sup> Consistent with the previous data pertaining to the increased number of cells in the x-direction, cells on anisotropically patterned substrates expressed 13 % higher average directionality ratio than those on isotropic samples ( $0.61 \pm 0.05$  vs.  $0.54 \pm 0.06$ ), further confirming that the arrangement of these soft regions can affect the directionality of cellular movement. The movement of cells on the control samples ( $\sim 6$ ,  $\sim 16$ , and  $\sim 30$  kPa substrates) with no stiffness and

topographical heterogeneity is more random than on both anisotropic and isotropic samples, indicated by a lower ratio of net to total displacement value ( $r = 0.46 \pm 0.04$ ). These data suggest that the alignment of cells can be directed by controlling the arrangement of patterned areas without actual topographical barriers.

## 3.6. Methods

### 3.6.1. Photodegradable monomer synthesis

Poly(ethyleneglycol) di-photodegradable acrylate (PEGdiPDA) was synthesized according to a previously reported protocol.<sup>86</sup> In brief, 4-[4-(1-acrylethyl)-2-methoxy-5-nitrophenoxy]butanoic acid (PDA) was coupled to poly(ethylene glycol) bis-amine ( $M_n \sim 3400$  Da) *via* solid-phase peptide synthesis (SPPS). The resulting product was dialyzed against deionized water for three days at room temperature and lyophilized. The purity of the monomer was verified using proton nuclear magnetic resonance ( $^1\text{H}$  NMR) in hexadeuterodimethyl sulfoxide ( $(\text{CD}_3)_2\text{SO}$ ; **Figure 3.2**).

### 3.6.2. Hydrogel film formation

A thin film of photodegradable hydrogel was prepared by copolymerizing 6  $\mu\text{L}$  of PEGdiPDA (20 wt. % in  $\text{H}_2\text{O}$ ) with 4.5  $\mu\text{L}$  of PEG monoacrylate (40 wt. % in  $\text{H}_2\text{O}$ ) and 3  $\mu\text{L}$  of adhesive peptide diethylene glycol-diethylene glycol-glycine-arginine-glycine-aspartic acid-serine-glycine with an acrylate functional group at the N-terminal (0.1 M; GenScript, NJ). To initiate the polymerization, 4  $\mu\text{L}$  of phosphate buffered saline (PBS), 2  $\mu\text{L}$  of ammonium persulfate (0.2 M), and 1  $\mu\text{L}$  of tetramethylethylenediamine (0.1 M, TEMED) were added. Upon addition of TEMED, the solution was quickly pipetted into a coverslip mold, consisting of an acrylated glass

slide covered by a non-acrylated glass slide with a rubber spacer ( $\sim 250 \mu\text{m}$ ) in between. For studying topological effects, engraved Si-wafers (fabrication details in **Figure 3.9**), instead of a flat non-acrylated glass slide, with negative square patterns with  $\leq 5 \mu\text{m}$  heights were used for molds. In brief, square pattern designs were generated on a S1805 photoresist-coated silicon  $\langle 100 \rangle$  wafer with a 500-nm thermal oxide layer (NOVA Electronic Materials, LLC) using a maskless aligner (Heidelberg MLA150). The patterns were then isotropically etched via deep reactive ion etching (DRIE, STS LpX Pegasus) with a 3kW RF Generator.

### *3.6.3. Pattern design and generation*

To fabricate stiff and soft domains, hydrogel films were locally exposed to light using a digital micromirror device (DMD) in a TERA-fab E-series instrument (TERA-print, Skokie, IL). Feature sizes and shapes were programmed by the pattern designs uploaded to the E-series software. The stiffness values were controlled by modulating the exposure time to a 405-nm light-emitting diode (LED) with an intensity of  $12 \text{ mW/cm}^2$ . The patterned hydrogels were rinsed to remove unreacted monomers and reagents and stored in PBS overnight at  $4 \text{ }^\circ\text{C}$ .

### *3.6.4. Pattern imaging and stiffness characterization*

The stiffness values of the patterned and non-patterned areas of the hydrogels were measured using an atomic force microscope (Dimension Icon AFM, Bruker, MA) using the force volume modulus mode. The measurements were conducted in the fluid cell with PBS solution at room temperature. SNL-10b and MLCT-a probes (Bruker) were used, and the spring constant of each probe was measured by calibrating the tips via a thermal tune process. The resulting force-

displacement curves were fit to the Sneddon model with an assumed Poisson's ratio of 0.5, and an average half-angle of 19°. Image and force curve analysis was performed using Nanoscope Analysis 2.0 software (Bruker).

### *3.6.5. Cell culture and seeding*

U87 glioblastoma cells (ATCC) were cultured at 37 °C with 5 % CO<sub>2</sub> in Dulbecco's modified eagle medium (DMEM) with 10 % fetal bovine serum and 1 % penicillin/streptomycin. Cells from passages 5-10 were used in all experiments. Before cell seeding, all hydrogel substrates were sterilized with 40 % ethanol solution and gently rinsed three times in PBS. Cellular viability was examined using a LIVE/DEAD™ imaging kit (Invitrogen™, MA) following the manufacturer's protocol.

### *3.6.6. Immunofluorescence imaging*

To monitor movement, cells were first incubated in a fluorescent dye solution, CellTracker™ Orange CMRA (15 µM in cell medium, Invitrogen™) for 30 min at 37 °C with 5 % CO<sub>2</sub>. Next, stained cells were seeded on the hydrogel surface at a seeding density of  $2 \times 10^4$  cells/cm<sup>2</sup>. Cell images and time-lapse videos were obtained one day after seeding using a confocal microscope (Zeiss LSM 800, Germany) for 2-4 h with 5-min intervals between images. The cell locations and movements were analyzed using TrackMate software in ImageJ (NIH).<sup>93</sup>

For the immunostaining of vinculin, the samples were fixed in 3.7 % paraformaldehyde in PBS for 15 min and rinsed with PBS three times. The cells were then permeabilized using 0.3 % Triton X-100 in PBS for 1 min and blocked with a 0.1 % Triton X-100 in PBS solution with 5 %

bovine serum albumin for 1 h. Primary antibody labeling for vinculin (1:200, mouse; ab18058) was performed in 5 % bovine serum albumin (BSA) in PBS overnight at 4 °C. Primary antibody was removed and rinsed in PBST (PBS with 0.5 wt. % Tween-20) one time and with PBS two times. Secondary antibody labeling using anti-rabbit Alexa Fluor 647 donkey (1:500; Invitrogen™) and DAPI (1 µg/mL) in 5 % BSA was performed. After a 1 h incubation at room temperature, the secondary antibody solution was removed and rinsed twice with PBST and once with PBS. The samples were kept in PBS at 4 °C until they were imaged.

### *3.6.7. Statistical Analysis*

Statistical analyses of all data were performed using GraphPad Prism 9.0 (GraphPad Software, Inc.). For the speed and morphology data, one-way ANOVA with Tukey's honestly significant difference was used to assess the statistical significance. The pattern characterization data are presented as mean ± standard deviation (SD), and cell-related data are reported as mean ± standard error of the mean (SE) unless otherwise noted.

## **3.7. Summary and Outlook**

In conclusion, we have developed a way to control the stiffness heterogeneity and topographical features in hydrogel matrices. With this technique, the influence of these two characteristics was decoupled from one another, allowing one to probe relative contributions to cancer cell migration. Cells grown on patterned substrates with  $10 \times 10 \mu\text{m}^2$  square features showed nearly a two-fold increase in the migration speed compared to those on substrates with larger (and smaller) pattern sizes or unpatterned surfaces. Importantly, the soft domains limit stable

focal adhesion formation, and their size and interpattern spacings can be modified to control migration rate and confinement. From the experiments carried out, it is clear that the confinement effect is primarily driven by durotaxis and that topography is less effective than stiffness heterogeneity for enhancing and directing cellular migration. Looking forward, by designing the edge-length of a pattern to be smaller than the minor axis of the cell, in principle, matrix heterogeneity at a sub-cellular length scale for any cell type can be controlled for directing cell migration, which may be useful in tissue engineering and wound healing. Although this work focuses on mechanical and topographical changes, chemical modifications could be used in combination to explore more ways to tune complex biological behaviors.

## Chapter 4

### Nanoscale Patterning to Probe and Control Cell-Matrix Interactions

This chapter is a continuation of the previous chapter, describing the efforts to systematically generate and precisely control the physical cues as well as the chemical cues within a cellular environment towards programming cellular behavior. While there has been extensive work on studying parameters, such as substrate elasticity, on cellular dynamics, the majority of these studies have been on homogeneous substrates. Recognizing that a homogenous continuum does not well represent the natural ECM, researchers have worked to generate substrates that mimic the heterogeneity found within the natural ECM as described in chapter 3. However, generating and replicating features on the nanoscale—the length scale on which cells begin to interact with their surrounding environment—in a massively parallel and systematic manner is still a challenge. To address this need, we have investigated in this chapter how cantilever-free, scanning probe, nano-lithographic techniques can be utilized to encode and tailor nanopatterns that serve as physical and chemical cues on 2D biocompatible substrates across large domains. Preliminary evidence of nanopatterning with controlled feature dimensions using PPL and BPL has been demonstrated.

---

Materials in this chapter is unpublished:

**E. Oh, C. A. Mirkin.** *On-going work*

## 4.1. Introduction

The ECM is a complex and hierarchically organized network of proteins, soluble growth factors, polysaccharides, and other biomolecules.<sup>61</sup> This environment not only provides structural support for cells but also delivers cues that orchestrate signaling pathways and a wide range of cellular processes, including differentiation, migration, and proliferation.<sup>94, 95</sup> Upon interaction with transmembrane cell receptors, such as integrins, these chemical and physical cues are transduced into biochemical signals through a process termed as mechanotransduction.<sup>96</sup> While numerous studies have identified the physicochemical cues that promote downstream changes in cellular machinery using homogenous materials<sup>89, 97, 98</sup>, elucidating how cells actually recognize and translate different biological cues still remains as a significant challenge.<sup>99</sup> It is mainly due to the difficulty in mimicking the natural ECM down to the length scale of individual adhesion receptors. To accommodate the need for an advanced biomaterial platform that incorporates heterogeneous properties of ECM, a biocompatible fabrication method that can generate patterns over a wide range of length scales is essential. Among various techniques, cantilever-free scanning probe-based lithographic techniques such as BPL<sup>13</sup> and PPL<sup>7</sup> provide a robust platform to encode physical and chemical cues with precise control over size, location, and composition on a wide range of biocompatible materials.

Utilizing BPL, the matrix with mechanical heterogeneity in the nanoscale regime can be engineered to answer fundamental questions in cell biology, including how cells receive and coordinate physical cues. In a landmark paper, Engler et al. established that substrate elasticity can be utilized as physical cues that guide the differentiation of mesenchymal stem cells (MSCs).<sup>89</sup> By tuning the cross-linking density of a polyacrylamide gel coated with collagen I, Engler and

coworkers mimicked the elasticity of the brain, muscle, and collagenous bone and directed the fate of MSCs towards neurogenic, myogenic, or osteogenic, respectively. However, it is important to note that the gel itself does not entirely recapitulate the complexity and hierarchical structure of natural ECM and that the manipulation of the mechanical properties without deforming the gel remains challenging. In an effort to build biomaterial scaffolds that mimic the dynamic nature of the ECM, the Anseth group recently synthesized a biocompatible hydrogel with phototunable mechanical properties where the *o*-nitro-benzylether photolabile group of this macromolecule allows spatiotemporal manipulation of mechanical properties of the gel.<sup>86, 100</sup> In this work, standard photolithography and confocal laser scanning microscopy were utilized to modulate the bulk stiffness of the gel by tuning the cross-linking density at desired locations. These techniques, however, are serial methods, mask-dependent, limited in throughput, and difficult to create nano-patterns. Other high-resolution patterning methods such as electron beam lithography and ion beam lithography suffer from low throughput and have extremely limited compatibility with biomaterials due to harsh processing conditions. Consequently, the effects of varying mechanical properties of the ECM at the nanoscale on cellular behavior are poorly understood due to the limited tools available for study. On the other hand, BPL developed by the Mirkin group is a massively parallel, cantilever-free patterning technique that utilizes light to generate arbitrary patterns with feature size that span a dynamic range of scales from nanometers to micrometers over large areas (several square centimeters).<sup>13</sup> BPL will enable the fabrication of 2D cellular scaffolds with precisely encoded nanoscale biological cues that will allow for the systematic investigation of stem cell differentiations and other cellular behaviors.

Using PPL, chemical cues can be systematically generated and precisely arranged to

examine the change in cellular motility and the direction of cell migration. It is well established that the interactions between cells and chemical cues presented in their ECM play a key role in guiding cellular functions and activities.<sup>101</sup> Therefore, there has been a growing interest in developing a method to generate chemical cues that define and regulate the shape, size, position, and behavior of the cells.<sup>102</sup> A common patterning technique used to generate these cues is microcontact printing developed by the Whitesides group.<sup>103</sup> The adhesive islands of pre-designed size and shape are generated by stamping self-assembled monolayers (SAMs) of alkanethiols on a gold substrate, but features are often limited by the length scale of the stamp and are commensurate with the size of an individual cell (on the order of 1-10  $\mu\text{m}$ ). PPL, another parallel writing technique developed by the Mirkin group, can also be utilized to precisely and controllably deliver chemical cues to cells using two-dimensional pyramidal pen arrays that can be inked with a variety of materials.<sup>7</sup> Unlike microcontact printing, PPL can generate arbitrary patterns with feature sizes ranging from the nano- to microscale in a mask-free fashion. Recently, PPL has also been shown to generate the size gradient of features by tilting the polymer pen arrays and change the pen-substrate contact area in each point. This technique has the potential to generate gradients of not only the feature sizes, but also the concentrations and the compositions of materials being deposited. This ability to generate heterogeneous patterns in a precisely designed manner allows the systematic investigation of cellular responses to chemical cues such as proteins found in the ECM and small molecules, including hormones and soluble growth factors.

Therefore, we hypothesize that by using cantilever-free scanning- probe lithography techniques, nano to micron patterns of physicochemical cues can be delivered to cells in such a way as to systematically probe the factors that control cellular migration and stem cell

differentiation. The ability to regulate and control such cues allows one to elucidate many fundamental questions regarding the cellular mechanisms involved in mechanotransduction and chemotaxis. Such findings can also provide insights into designing biomaterials for tissue engineering and regenerative medicine.

#### 4.2. Using Beam Pen Lithography to Control Physical Cues

The nanoscale features patterned by BPL on soft materials (e.g., hydrogel) can be utilized as physicochemical cues to recapitulate the complex architecture of the natural matrix. These patterns of varying stiffness will effectively regulate and control cellular behavior, including stem cell differentiation. The heterogeneous stiffness matrix engineered by BPL will serve as a novel cell culture platform to thoroughly study cell-matrix interactions. Using these matrices, we will examine whether the length, size, and density of these mechanical nano-patterns bias stem cells towards a specific differentiation and if the cells will show a preferential selection of one factor over the other.

In order to scrutinize the effect of the mechanical heterogeneity of substrate on the fate of stem cells, a photodegradable polyethylene glycol (PEG) based hydrogel has been synthesized by following the reported procedure.<sup>72, 86, 87, 100</sup> This material was chosen as a model material because it is biocompatible, non-toxic, and has been successfully demonstrated a successful use in the previous chapter (**Chapter 3**) and other literatures. As described before, the gel contains a photolabile group consisting of a nitrobenzyl ether-derived moiety that allows real-time photo-manipulation of the gel's mechanical properties. The hydrogel is compatible with the light source of the beam pen array, which is a 405-nm light-emitting diode (LED) in the DMD system used in

Chapter 3. The nitrobenzyl moiety is cleaved upon exposure, and the local cross-linking density decreases, thus changing the stiffness of the gel. The goal of this chapter is to use beam pen arrays to encode matrix heterogeneity to this photodegradable hydrogel at a sub-micron length scale by locally tuning the cross-linking density.

In order to properly deliver the light, the beam pen array needs to be in contact and parallel with the surface of the hydrogel. Because the current beam pen array setup (or TERA-Fab E-Series instrument) uses the electrical contact to align the pen tips with the substrate, the boundaries of the substrate must be conductive. Due to the low conductivity of the hydrogel, however, a holder for loading the hydrogel into the TERA-print instrument was designed to enhance the electrical contact between the hydrogel and the pen array tips. The spacers used to mold the hydrogel were coated with gold and placed with the hydrogel to enable electronic leveling. Using this holder, we successfully patterned the hydrogel by BPL (**Figure 4.1**). This approach allows for the use of BPL as a tool for patterning soft and non-conductive materials.

With a BPL system, the feature size is controlled by the diameter of the aperture. Currently, the smallest feature size achieved was 1.4  $\mu\text{m}$  by using a pen array with an average 1  $\mu\text{m}$  aperture (**Figure 4.1a**). The hydrogel was exposed under light for 5 min at 100% intensity of 25  $\text{mW}/\text{cm}^2$ . While we were able to induce local stiffness changes with BPL, higher density patterns with smaller feature sizes are needed to mimic the heterogeneity of the ECM. We are also currently working towards moving pen arrays in the  $x$  and  $y$  directions using a precise piezo controller to increase the density of features patterned by BPL. The preliminary data for  $x$  and  $y$  control is shown in **Figure 4.1b**.

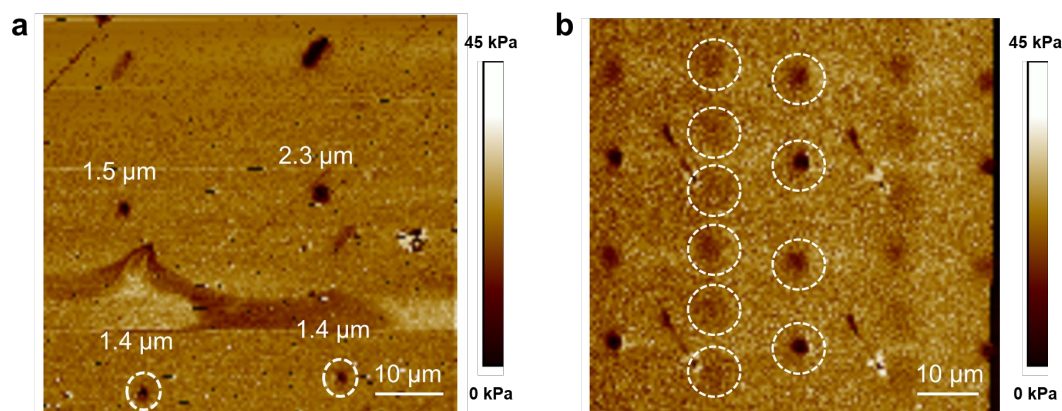


**Figure 4.1.** AFM elasticity map of patterned hydrogel's surface using BPL arrays. (a) The pens with an aperture size of  $1\ \mu\text{m}$  were used to locally expose hydrogel for 5 min. The sizes of the features are denoted, and the smallest features are indicated with dotted circles. (b) The capability of x and y patterning using BPL is demonstrated. Any changes in local stiffness are indicated with dotted circles.

During the electric leveling, some force is applied onto the surface of the hydrogel to make sure all pens are in contact. To test if the applied force caused any physical deformation and resulted in consequent height and stiffness changes, the patterning was performed at a range of forces (1000 mN and 2000 mN) without any light exposure. An applied force of 2000 mN is substantially higher than the average applied force during the patterning, which is  $\sim 1000\ \text{mN}$ . The pen array with  $1\ \mu\text{m}$  aperture size was used with  $30\ \mu\text{m}$  pitch distance, and the array was in contact with the hydrogel substrate for at least 5 min. AFM images were scanned to compare the hydrogel's surface and its mechanical properties before and after the patterning. As shown in **Figure 4.2**, there were no significant changes observed in both height profile and force volume modulus image after the patterning, indicating that the stiffness of the hydrogel was only modified by the exposed UV light. The beam pen array itself does not damage the hydrogel during the patterning and can be integrated with soft materials to perform localized photochemistry.

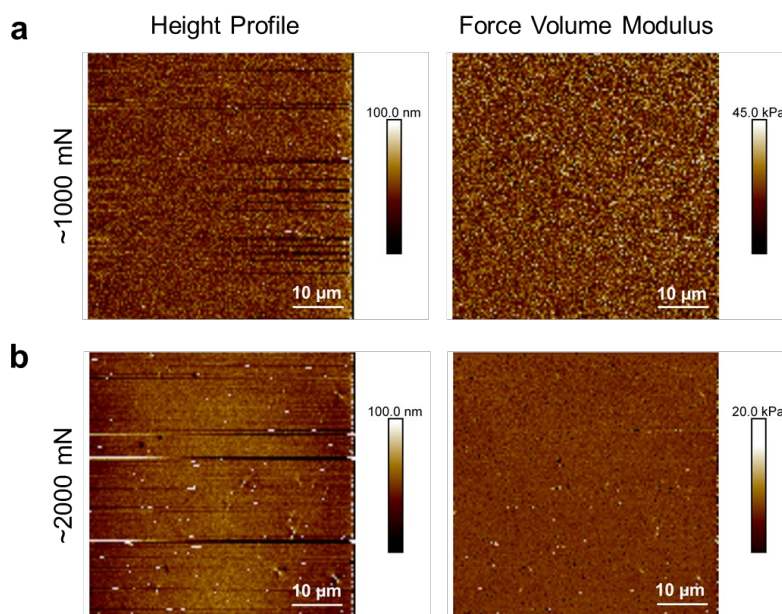


**Figure 4.2.** Height (left) and modulus (right) profiles of patterned hydrogels without light exposure with ~1000 mN (a) and ~2000 mN (b) applied forces.

As this study aims to investigate how stem cell differentiation is affected by local changes in the hydrogel, the cell-matrix interactions with the synthesized and photodegraded hydrogels must be understood. Consequently, human mesenchymal stem cells (hMSCs) were seeded onto photodegraded hydrogels, and cellular viability was studied (**Figure 4.3**) *via* live-dead cell imaging. The cells proliferated and the majority were live, indicating the non-toxicity and biocompatibility of the photodegraded hydrogel. In the future, a preferential response of stem cells to either hard or soft regions will be investigated while also exploring how the length, size, and density of the pattern hydrogels will bias stem cells towards a specific differentiation. The differentiated cells will be analyzed using quantitative real-time reverse transcriptase polymerase chain reaction (qRT-PCR) and immunofluorescence.

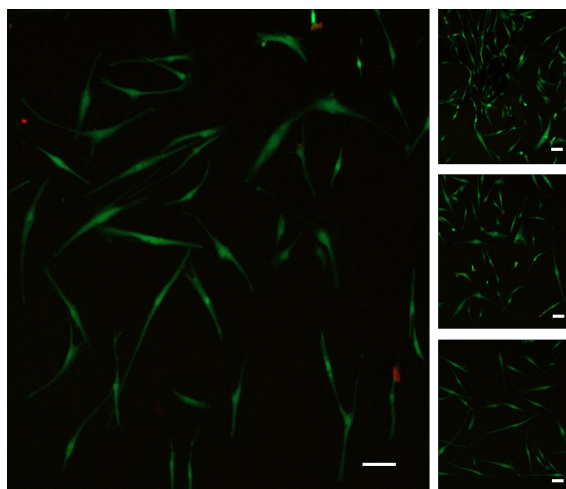


**Figure 4.3.** HMSCs seeded and grown on the surface of uniformly degraded PEGdiPEA hydrogel. Green and red colors indicate live and dead cells, respectively. Scale bar = 100  $\mu\text{m}$ .

### 4.3. Spatially Encoded Chemical Cues *via* Polymer Pen Lithography

#### 4.3.1. Patterns of Varying Sizes and Dimensions

The objective of this study is to examine the impact of the size, pitch distance, and density of patterned chemical cues at the nanoscale on cell migration and motility. In previous work by Frey *et al.*, it was reported that the speed of cell migration decreases exponentially as the size of nano-patterned adhesion sites increases.<sup>104</sup> In this work, however, the cell speed was measured without accounting for the interdependency between pitch distance and the density. Also, the shape of these patterns was different for each size. Therefore, we intend to extend this study in a more systematic and controlled way by varying the pitch distance or the size while keeping the density constant and varying the pitch distance while keeping the size constant.

The basic process for generating molecular patterns using PPL consists of two major parts: (i) deposition of alkanethiols such as 16-mercaptohexadecanoic acid (MHA) onto a gold surface and (ii) functionalization of these patterns with proteins like fibronectin, the ECM protein that

binds to the integrin or a transmembrane receptor responsible for cell-matrix adhesion. Cells only adhere to the patterns with fibronectin. The scheme for PPL patterning is shown in **Figure 4.4**.

In a proof-of-concept experiment, the polymer pen array was first inked with 10 mM ethanol solution of 16-mercaptohexadecanoic acid (MHA). Utilizing the inked pen array, MHA features with average diameters of  $1.14 \pm 0.09 \mu\text{m}$  and  $473 \pm 38 \text{ nm}$  were generated on gold substrates. The average areas are respectively,  $1.0 \pm 0.2 \mu\text{m}^2$  and  $0.18 \pm 0.03 \mu\text{m}^2$ . These two pattern's pitch distances were adjusted to  $5 \mu\text{m}$  and  $2 \mu\text{m}$ , respectively, to keep the 4% MHA coverage and the density of fibronectin constant. The sample with a  $0 \mu\text{m}$  pitch distance was also prepared by attaching fibronectin to a self-assembled monolayer of 100% MHA and utilized as a control (despite not having comparable coverages). Prior to fibronectin immobilization, regions between the patterned spots (area with no MHA) on the substrates were passivated with tri(ethylene glycol) (EG3) terminated thiol to reduce non-specific protein adsorption. Consequently, fibronectin only binds within the patterned regions. The substrates were characterized with lateral force microscopy (LFM) for pattern verification (**Figure 4.5**). Unlike AFM, LFM measures the deflection of the cantilever in the lateral direction, and the frictional coefficient determines the magnitude of this deflection. The bright yellow spots represent MHA domains, while the brown background consists of EG3. The backfilled MHA-patterned substrates were then functionalized with fibronectin. The human umbilical vein endothelial cells (HUVECs) were cultured on these substrates, and their responses were observed.

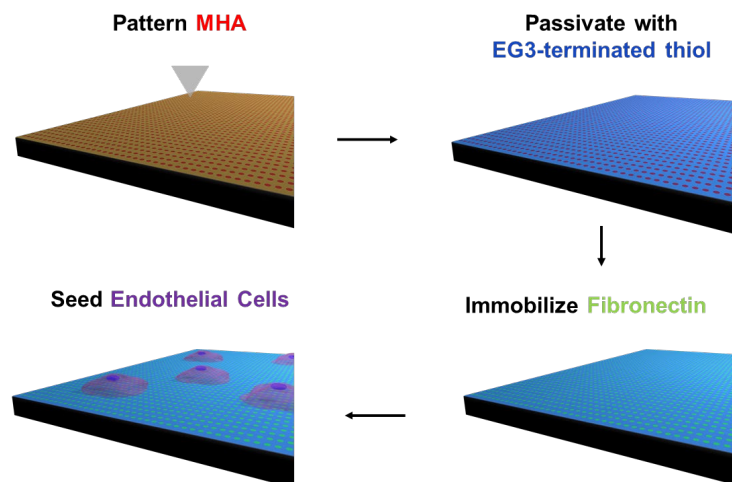


**Figure 4.4.** Schematic diagram of PPL patterning for making molecular patterns.

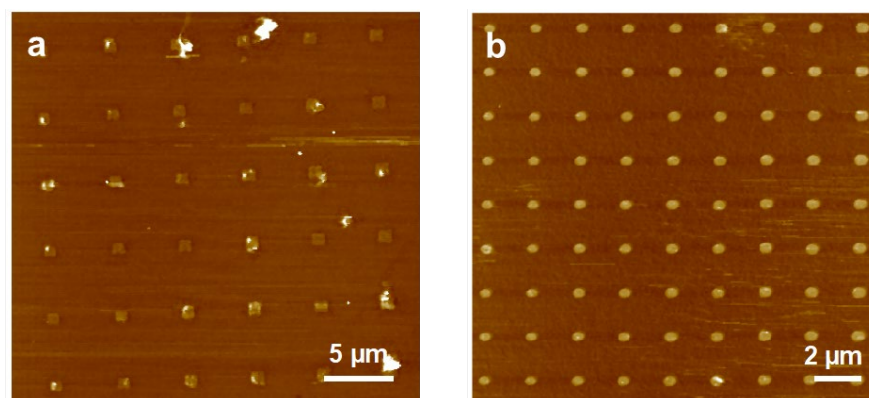


**Figure 4.5.** LFM friction images for MHA patterned Au substrates backfilled with EG3. The yellow dots represent MHA features, and the background is EG3. Samples with (a) 5  $\mu\text{m}$  and (b) 2  $\mu\text{m}$  pitch distance.

The movement of the cultured HUVEC cells was monitored using live-cell confocal microscopy (**Figure 4.6a**). The cells were stained with a tracker green, fluorescent indicator, and the images were taken at 5 min intervals for over 4 hours. Using these images, the average speed of the migration was calculated (**Figure 4.6b**). The initial results indicated that the rate of cellular migration was faster for 2  $\mu\text{m}$  pitched patterns than that of the control substrate and the 5  $\mu\text{m}$  spaced patterns. Furthermore, the migration speed for the control was very close to that of the 5

$\mu\text{m}$  sample. This indicates that there might exist an optimum pitch for focal adhesion that maximizes motility between a pitch of zero and a pitch of  $5\ \mu\text{m}$ . Further experiments need to be performed to verify this expected result. Overall, the preliminary data supports and corroborates similar conclusions from the past works that the spatial and geometric arrangements (i.e., size, pitch distance, and density) impact cell migration.<sup>55, 104-107</sup>

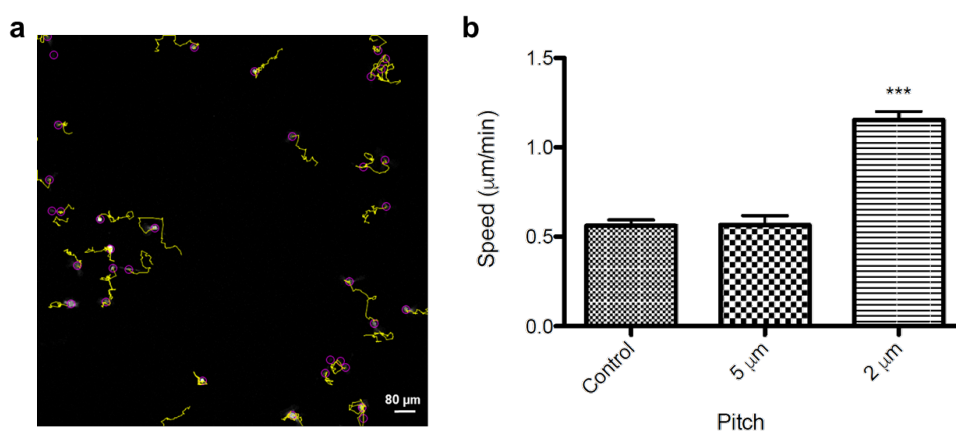


**Figure 4.6.** Movement of HUVEC cells on patterned surfaces. (a) Fluorescently labeled cells monitored were with confocal microscopy and analyzed with ImageJ software. The yellow line indicates the pathway of a cell, which is marked with a purple circle. (b) The plot of the average speed of cell migration for control,  $5\ \mu\text{m}$ , and  $2\ \mu\text{m}$  samples.

#### 4.3.2. Patterns with Compositional Gradients

Here, the goal is to utilize PPL to establish chemotactic gradients that can program and direct cell migration to specific regions. A chemical gradient of nano-patterns can be created using a dual spray coating technique developed by the Mirkin group.<sup>11</sup> Given the distance between the spray reservoir and the pen array, a uniform compositional gradient can be created over centimeter-scale areas, where each coated pen is essentially unique in composition and subsequently, pattern this gradient onto a surface. The expected composition gradients are shown in **Figure 4.7**.

To apply a bias to cell migration, EG3-disulfide and maleimide-disulfide were used as inks

because maleimide provides thiol chemistry to attach adhesion peptides covalently. Before generating the chemical gradient of these two molecules, we first examined if maleimides can be transferred from a pen array and encoded on a gold substrate across large areas. The fluorescently labeled thiolated-single stranded DNA was attached to patterned maleimide for visualization before peptide immobilization. The maleimide features were successfully patterned (**Figure 4.8**) and were then immobilized with cyclic Arginyglycylaspartic acid (RGD) peptide, a common peptide sequence used for cell adhesion. As a result, the maleimide gradient was used to form a gradient of cyclic RGD peptide. Adhesion receptors of cells, integrins, recognize and bind to RGD, which allow cells to attach to the surface of ECM. The cells were, therefore, expected to migrate towards an area with a higher density of RGD.

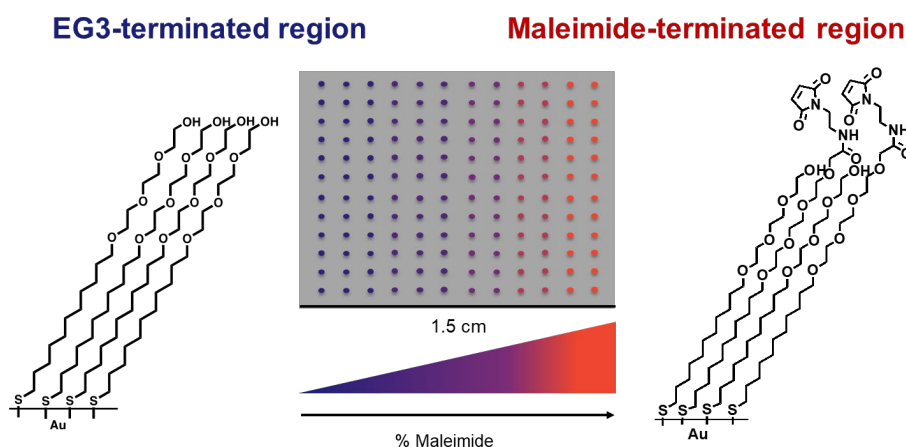


**Figure 4.7.** Expected gradient using the dual spray coating method. The compositional gradient is generated using two different inks, EG3-disulfide and maleimide-disulfide. More percentage of maleimide ink is expected in the horizontal direction as indicated here with an arrow. On the far left, only EG3 ink should be transferred to the substrate.

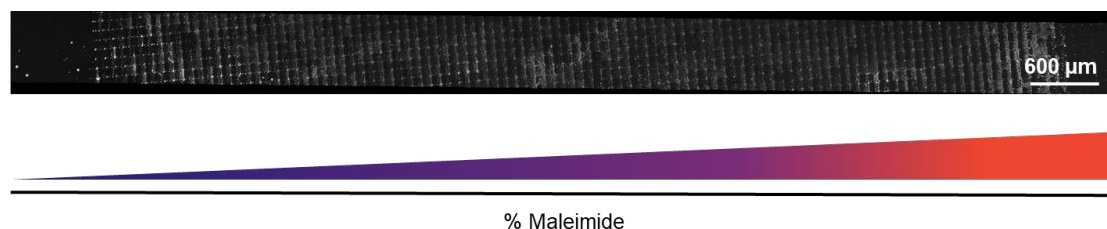


**Figure 4.8.** Stitched confocal images of patterned EG3 and maleimide over a large area. The maleimide groups are functionalized with fluorescently labeled thiolated-single stranded DNA for visualization.

In addition to substrates with compositional gradients, three uniformly coated maleimide-EG3 surfaces (non-patterned samples) were fabricated as controls and benchmarks. Each substrate contained either 50%, 25%, or 5% maleimide, which later was functionalized with RGD. As indicated in the chemical structure shown in **Figure 4.9**, 50% maleimide sample is expected to have an equal distribution of maleimide and EG3, and 1:3 ratio of maleimide to EG3 for 25% maleimide substrate. On the surfaces of these substrates, HUVEC cells were seeded and monitored using confocal microscopy. As expected, they moved in all directions and were not localized in any specific areas; their movement was random, and therefore, had no directions.

The migration speed of cells was also measured to examine the effect of % RGD (or maleimide) on cell migratory behavior. Interestingly, 25% maleimide showed the highest rate of migration, followed by a 5% sample. The slowest speed was observed for the substrate with 50% maleimide. The key in cellular motility is the rate of focal adhesion assembly and disassembly and how well these two steps are coordinated. Therefore, it is important to have a balance between the regions that promote or hinder adhesion formation. In this case, the regions with EG3 inhibit, whereas those functionalized with RGD promote focal adhesion formations. Based on this observation, we concluded that when there are numerous adhesion sites available, cells tend to form stronger adhesions on the surface of the matrix, which slows down the rate of focal adhesion

disassembly. If there are only a few sites with adhesion ligands or proteins, the substrate can no longer support cell attachment as cells cannot properly spread and form stable adhesions.

To conclude from these preliminary results, EG3-disulfide and maleimide-disulfide inks can be patterned onto an Au-coated substrate using PPL over a large area. The compositional gradients of EG3 and maleimides can be used to generate a gradient of adhesion ligand, which can then affect the direction of cellular movement. In addition, the amount of maleimide present on the substrate affects the speed of migration by controlling the adhesion formation of the cells. The ability to control cellular movement through control of the size and spacing of these adhesive sites provides a handle to tune cell migration, which is crucial in tissue engineering fields where fast and site-specific cell movement is necessary.

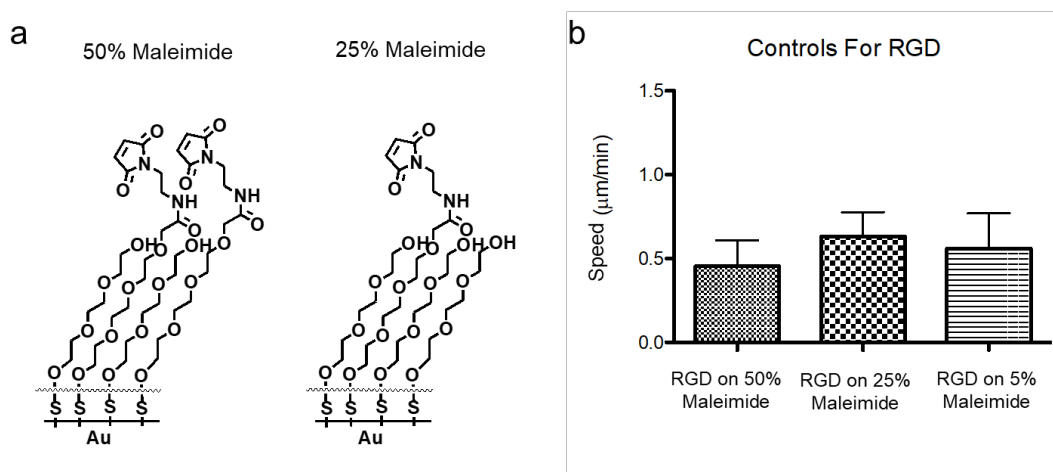


**Figure 4.9.** (a) Chemical structures of maleimides (50% and 25%) functionalized on Au surfaces *via* Au-S linkage. (b) The migration speed of HUVEC cells seeded on control samples where the surface of Au-coated substrates is functionalized with different percentages (50%, 25%, and 5%) of maleimides. These maleimides were coupled to the RGD peptides for cell attachment.

## 4.4. Experimental Details

### 4.4.1. Fabrication of Beam Pen Arrays

Beam pen arrays are fabricated by a method developed by the Mirkin group. First, a 200 nm layer of gold is deposited onto the PPL arrays with 5 nm of the titanium adhesion layer. For BPL, the pitch distance of 30  $\mu\text{m}$  is used with the pyramidal base edge-length of 15  $\mu\text{m}$ . The surface of the Au-coated pen array is functionalized with 10 mM 1H, 1H, 2H, 2H-Perfluorodecanethiol (97%) in methanol. To generate an aperture at each pen tip, the pen array is first spin-coated with fluorinated oil. Then, the pen array is placed on a pre-heated hot plate at 60  $^{\circ}\text{C}$  for 3 min to allow the viscous oil to flow and expose gold at the apex of the tip. The placement of the oil meniscus and the tip of the pen arrays can be examined using an optical microscope. When the meniscus is right on top of the pen tip, white edges converge into one bright point, and the wrinkling effect of lines around the center is observed. Once the gold at the tip of the pen arrays is exposed, it is chemically etched using an Au-etchant solution. The excess oil of the array is removed using a PFPE Re-move solution. The size of the apertures is confirmed by SEM images.

### 4.4.2. Fabrication of Polymer Pen Arrays

To fabricate polymer pen arrays, a Si-master containing pyramidal shaped wells need to be first designed. The protocols for making these Si-masters are reported in the previous literature<sup>8</sup> and the Experimental Details Section of Chapter 2 (2.3.2. Fabrication of Pen Array Masters).

#### 4.5. Summary and Outlook

Herein, the feasibility and the practicability of BPL and PPL to program desired cellular functions by encoding physical and chemical cues on the cell culture environment have been discussed and investigated. We have demonstrated that PPL can be used to pattern chemical cues with different size and pitch distances in a systematic fashion. Interestingly, we observed that the patterns on the substrate impacted the rates of cellular migration. Furthermore, PPL can be utilized to promote directional cell movement by applying a chemotactic bias towards a specific region or direction using nano-patterns that contain different concentrations and compositions of ligands that cells can recognize. Additionally, a hydrogel film with phototunable physical properties was synthesized. The initial degradation data verified that the stiffness of this hydrogel is phototunable *via* BPL. Such implications of programming cellular behavior in response to the physical and chemical cues are very beneficial for designing materials used in tissue regeneration and transplantation.

## Chapter 5

### Tip-assisted Synthesis of Covalent Organic Frameworks

This chapter reports a novel method for synthesizing covalent organic frameworks, crystalline porous polymers that can be designed in predictable structures using a PPL platform. This approach overcomes current major bottlenecks in COFs synthesis and enables the rapid and direct synthesis of COFs at room temperature without harsh post-processing steps. Using a 2D array of pyramidal-shaped pen tips, nanoreactors containing organic monomers can be deposited and patterned onto a variety of substrates with size and spatial control, demonstrating the site-selective growth of COF crystallites. In addition, by adding a modulator and a low vapor pressure solvent, the growth kinetics of COF polymers can be controlled. Our findings provide new insights into the formation of COF crystals and the development of new strategies to synthesize COFs.

---

Materials in this chapter will appear in a subsequent publication:

**E. Oh**, D. Shin, C. A. Mirkin. *In preparation*

## 5.1. Introduction

Covalent organic frameworks (COFs) are a new emerging class of polymers synthesized in highly ordered structures with well-defined geometries or topology and tunable chemical functionality.<sup>108-112</sup> The monomers or building units of COFs contain light elements, such as H, B, C, N, and O, that are known to form strong covalent bonds—hence the name COFs, and they are linked *via* a directional bonding approach to create crystalline organic structures. Several features of COFs, such as high thermal and chemical stability, permanent porosity, predictable design rules, and biocompatibility have attracted great attention in diverse applications, including but not limited to water purification<sup>113, 114</sup>, energy storage<sup>115, 116</sup>, catalysis<sup>117</sup>, and chemical sensing<sup>118, 119</sup>. Since their first report in 2005 by Yaghi and co-workers<sup>108</sup>, COFs have been predominantly synthesized *via* solvothermal and hydrothermal synthetic approaches, which usually require long reaction times on the order of days, high temperatures above 100 °C, and further post-processing steps. In addition, these current methods more often than not result in insoluble, multicrystalline polymer aggregates with poor processability, precluding many of the applications above.

In order to overcome these shortcomings, numerous synthetic routes have been recently developed and reported. Using microwave<sup>120</sup>, sonochemical techniques<sup>121</sup>, and UV light<sup>110</sup>, the reaction time was drastically reduced. The high crystalline COFs with structural precision were obtained by synthesizing them in thin films with precisely defined thickness.<sup>122, 123</sup> Despite these efforts, high temperatures and reprocessing steps are still required, and site-selective growth of COFs with size and morphology control remains a challenge, limiting their use in device

fabrication. Therefore, a new synthetic method that can address most, if not all, of the problems is necessary and required.

Here, we report a novel synthetic approach using PPL for synthesizing high quality COFs in a high-throughput manner at room temperature with controllability over size and placement. Previously, the synthesis of size-controlled halide perovskite nanocrystal arrays has been demonstrated using PPL, in which an ink solution containing the halide perovskite precursors was transferred onto the substrate in forms of more than 100,000 droplets.<sup>124</sup> These droplets were then served as nano-sized reactors for guiding nanocrystal synthesis. Similarly, the nanoreactors containing the monomers for the COF polymerization were precisely patterned and defined on silicon substrates using PPL. The preliminary patterning and growth of imine-linked COFs used as a model network were successfully demonstrated. By systematically controlling the amounts of inks loaded onto the substrates, the growth mechanisms of COFs were probed and further studied.

## 5.2. Results and Discussion

The overall fabrication steps for synthesizing COF nanocrystals using the PPL technique are summarized in **Figure 5.1**. To polymerize one of the types of imine-linked network, COF-1, 1,3,5-tris(4-aminophenyl)benzene (TAPB) and 1,3,5-benzenetricarbaldehyde (BTCA) were used respectively as base and linker monomers. These monomers were mixed in 1:1 ratio and dissolved in a dimethyl sulfoxide (DMSO) solution containing sulfolane. This precursor solution was then spin-coated onto the pen array consisting of more than 1000 pyramidal pen tips made of polydimethylsiloxane. To ensure uniform spreading of an ink solution, the pen array was plasma cleaned to increase its hydrophilicity.

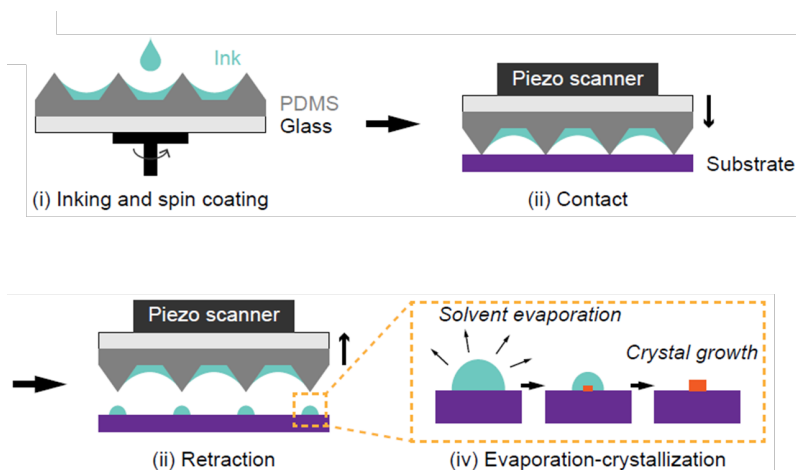


**Figure 5.1.** Schematic illustration of PPL patterning steps for synthesizing nanocrystals. Figure adapted from ref. 124. Reprinted with permission from AAAS.

As a proof-of-concept experiment, the  $4 \times 3$  dot matrix pattern was printed on a Si-wafer treated with a fluoropolymer, which prevents inks from spreading and keeps monomers inside the printed domes or nanoreactor. The patterned COF-1 features were confirmed and analyzed using SEM (**Figure 5.2a**). As a control experiment, the base monomer, TAPB, was also patterned without the linker units added to the precursor (**Figure 5.2b**). Compared to the monomer patterns where a single, large black aggregate was observed, several white flakes or nanoparticles were observed inside the COF-1 patterned regions. These nanoparticles had the same morphological characteristics as the previously reported COF-1 polymers.<sup>125</sup>

We hypothesize that the fast evaporation of the solvent in nanoreactors due to high surface-area-to-volume ratio triggers rapid polymerization of the monomers with multiple nucleation events and prevents further growth, resulting in the formation of several nanoparticles instead of a single-crystalline crystal. To control the evaporation speed of the nanoreactors, the ratio between sulfolane to DMSO was significantly increased (from 8:2 to 8:2). Sulfolane is a dipolar aprotic solvent with extremely low vapor pressure<sup>126</sup>, and therefore, can remarkably slow down the

evaporation of the solvent in the nanoreactors, which was clearly observed in the time-lapse images captured using recording software (**Figure 5.3**). As expected, the COF-1 polymers printed with a higher ratio of sulfolane were slightly larger in size, but more importantly, the number of particles observed in the patterned region was significantly reduced (**Figure 5.4**).

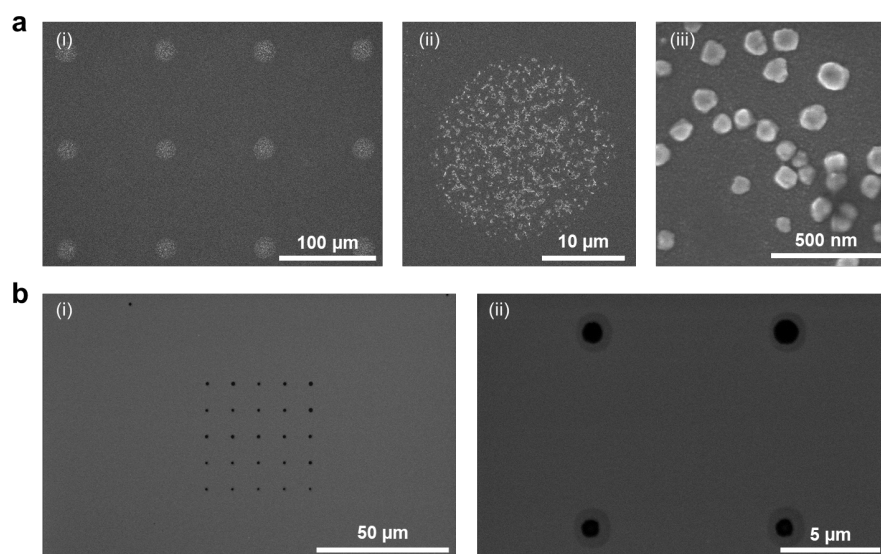


**Figure 5.2.** a) SEM images of COF-1 polymers synthesized using the PPL approach. (i) a  $4 \times 3$  dot pattern on a fluoropolymer treated Si-wafer, with magnified images (ii) and (iii), displaying the particle formation. b) TAPB monomers patterned in a  $5 \times 5$  matrix.

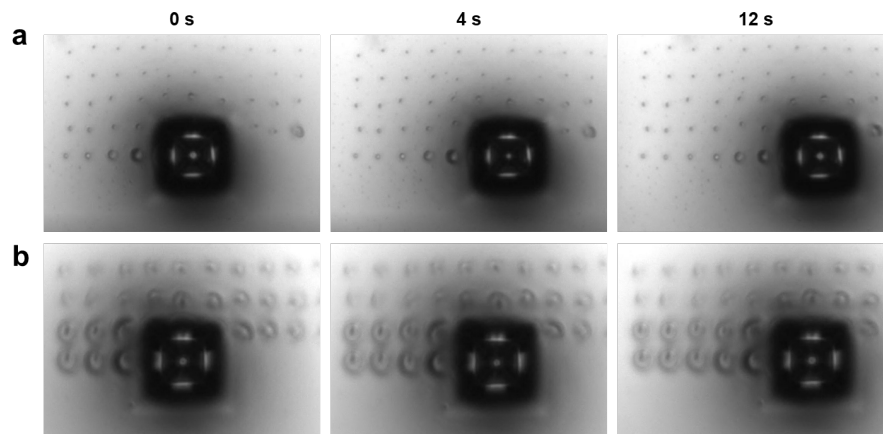


**Figure 5.3.** COF-1 monomers patterned on Si-wafer without (a) and with (b) sulfolane in the precursor inks. The nanoreactors containing sulfolane take a longer time to evaporate.

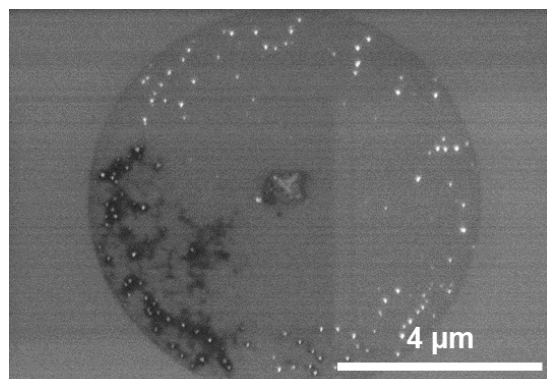


**Figure 5.4.** SEM image of COF-1 feature patterned using the precursor ink with the increased amount of sulfolane.

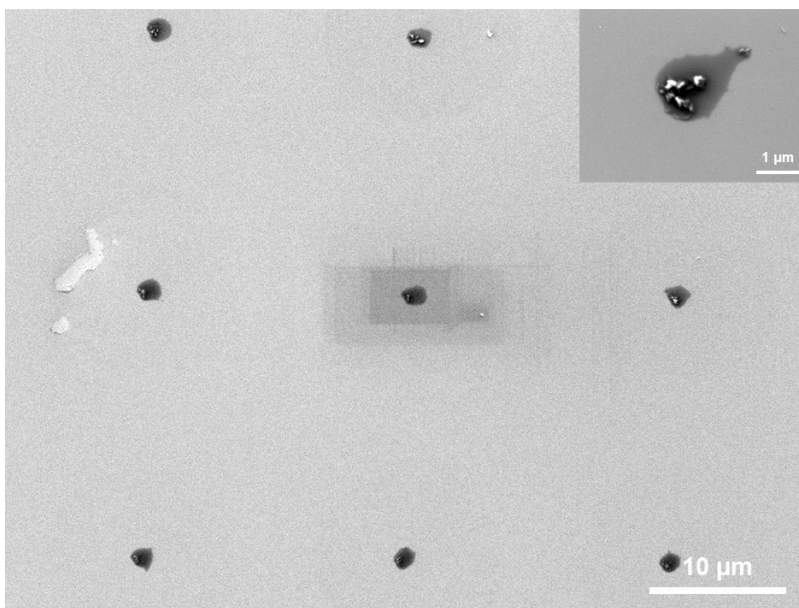


**Figure 5.5.** A  $3 \times 3$  dot matrix of COF-1 patterns synthesized with an aniline modulator. In each dot, large COF crystals were observed.

To control the nucleation and the growth of COFs, previous studies have reported the use of modulators, organic molecules that can bind to the monomers and change the polymerization process.<sup>127, 128</sup> The addition of a modulator to the polymer solution decreases the rate of nucleation without eliminating the seeded growth of existing particles. In addition, the modulator can bind

with the monomer and promote the exchange, allowing the particles to grow instead of forming new nuclei continuously. Here, we used aniline as a modulator to enhance the reversibility of imine bond formation and promote large crystal growth.<sup>127</sup> As shown in Figure 5.5, COF-1 features patterned using a precursor ink containing aniline showed the localized formation of crystallites with a significant increase in size compared to those printed without aniline, where small particles were dispersed throughout the patterned region. By controlling the concentration of aniline in the nanoreactors, we expect to be able to grow a single-crystalline COF per each dot in the pattern. The crystallinity of these patterned COFs can be examined using TEM.

### 5.3. Summary and Outlook

To summarize, we have developed a new synthetic method using PPL to synthesize COF crystals at room temperature without any further processing. Using this approach, imine-linked COFs were rapidly synthesized in high-throughput and patterned with precise spatial control. By adding sulfolane as the main solvent and aniline as a modulator, the nucleation and growth of COF-1 polymers were controlled. We concluded that the key to synthesizing a large single COF crystal using the PPL method is the slow evaporation of the nanoreactors with reversible imine bond formation. Because nanoreactors can be patterned with a size or compositional gradient across large areas, detailed kinetics studies can also be performed to understand the reaction conditions for synthesizing crystalline and high-quality COFs.

# **Chapter 6**

## **Conclusions and Outlook**

## 6.1. Summary and Future Opportunities

Here, the development of approaches to integrating soft materials in the CFSP platform as the pen tips, substrates, or inks for building multi-functional structures with high resolution is summarized below. The future directions and outlook for each chapter are also discussed and highlighted.

First, a novel cantilever-free electrochemical patterning approach, termed electrochemical polymer pen lithography (ePPL), was discussed. ePPL uses a hydrogel array of pyramidal pen tips to perform localized electrodeposition in a massively parallel manner. This technique has an unprecedented level of control over resolution, height, and spatial arrangement that allows one to rapidly deposit and generate spatially-encoded 2D/3D metallic structures using >10,000 hydrogel tips that act in parallel. Notably, the materials-versatility of ePPL enables the patterning of controlled-composition mono- and multi-metallic features on various conductive substrates. This technique, therefore, can be used as a combinatorial screening tool, allowing one to synthesize megalibraries of alloy materials with a size and compositional gradient across a single substrate and screen for the most active materials for various applications, including electrocatalysis, plasmonics, and magnetics. As such, the development of this technique is a significant step towards realizing rapid combinatorial screening of metal alloys and high-throughput metallic 3D nanoprinting.

Secondly, the fabrication of hydrogel-based substrates that contain sub-cellular to cell-scale ( $5\ \mu\text{m}$  to  $50\ \mu\text{m}$ ) stiffness and topographical cues encoded by photopatterning was reported. Using these patterned substrates, we found that the spatial organization of soft regions plays a critical role in the regulation of cellular migration. Specifically, cell migration speed increases when

features are spaced at critical dimensions dependent on cell size through self-selective confinement of cells to stiffer regions of the hydrogel. In addition, we show a preferential migration response to stiffness differences that is not observed with topographical variations. Our study of cancer cell-ECM interactions can give insights into how cells sense biophysical cues critical to metastasis as well as providing pathways to directing cells using local mechanical cues.

Thirdly, to further improve the resolution of the patterned features used in the cancer cell study, BPL was combined with a DMD system to locally tune the crosslinking chemistry of the photo-responsive hydrogel. Using a pen array with an aperture size of 1  $\mu\text{m}$ , the feature with a diameter of 1.4  $\mu\text{m}$  was successfully patterned, which is the smallest pattern size reported on this type of hydrogel. In addition, PPL was used to encode chemical cues on the scale of individual focal adhesions. A compositional gradient of two biomolecules was generated on a single substrate to guide the direction of cell movement. We expect to address using these nanopatterned substrates some unanswered biological questions, such as what length or size scale of stiff (or soft) patterns begin to promote osteogenic differentiation (or adipogenesis) or how deep cells need to reach through the material to sense the heterogeneity.

Lastly, crystalline porous polymers, or also known as covalent organic frameworks, were synthesized by PPL, primarily *via* the solvent evaporation method. The liquid containing organic molecules is transferred onto the substrate as nanodroplets, which are then served as nanoreactors for the polymerization process. As the solvent in these nanoreactors evaporates, it triggers the nucleation and growth of the COF crystals. This novel synthetic method does not require vacuum drying, reduces the long reaction time of conventional polymerizations of imine-linked COFs, and provides spatial controllability, which would be helpful in various applications.

## REFERENCES

1. Brown, K. A.; Hedrick, J. L.; Eichelsdoerfer, D. J.; Mirkin, C. A., Nanocombinatorics with Cantilever-Free Scanning Probe Arrays. *ACS Nano* **2019**, *13*, 8-17.
2. He, Q.; Tan, C.; Zhang, H., Recent Advances in Cantilever-Free Scanning Probe Lithography: High-Throughput, Space-Confined Synthesis of Nanostructures and Beyond. *ACS Nano* **2017**, *11*, 4381-4386.
3. Little, J. A.; Gallatin, G. M., Nanomanufacturing: A Perspective. *ACS Nano* **2016**, *10*, 2995-3014.
4. Laramy, C. R.; O'Brien, M. N.; Mirkin, C. A., Crystal engineering with DNA. *Nat. Rev. Mater.* **2019**, *4*, 201-224.
5. Piner, R. D.; Zhu, J.; Xu, F.; Hong, S.; Mirkin, C. A., Dip-Pen Nanolithography. *Science* **1999**, *283*, 661.
6. Salaita, K.; Wang, Y.; Mirkin, C. A., Applications of dip-pen nanolithography. *Nat. Nanotechnol.* **2007**, *2*, 145-155.
7. Huo, F.; Zheng, Z.; Zheng, G.; Giam, L. R.; Zhang, H.; Mirkin, C. A., Polymer Pen Lithography. *Science* **2008**, *321*, 1658.
8. Eichelsdoerfer, D. J.; Liao, X.; Cabezas, M. D.; Morris, W.; Radha, B.; Brown, K. A.; Giam, L. R.; Braunschweig, A. B.; Mirkin, C. A., Large-area molecular patterning with polymer pen lithography. *Nat. Protoc.* **2013**, *8*, 2548-2560.
9. Giam, L. R.; Massich, M. D.; Hao, L.; Shin Wong, L.; Mader, C. C.; Mirkin, C. A., Scanning probe-enabled nanocombinatorics define the relationship between fibronectin feature size and stem cell fate. *Proc. Natl. Acad. Sci.* **2012**, *109*, 4377.
10. Cabezas, M. D.; Meckes, B.; Mirkin, C. A.; Mrksich, M., Subcellular Control over Focal Adhesion Anisotropy, Independent of Cell Morphology, Dictates Stem Cell Fate. *ACS Nano* **2019**, *13*, 11144-11152.
11. Kluender, E. J.; Hedrick, J. L.; Brown, K. A.; Rao, R.; Meckes, B.; Du, J. S.; Moreau, L. M.; Maruyama, B.; Mirkin, C. A., Catalyst discovery through megalibraries of nanomaterials. *Proc. Natl. Acad. Sci.* **2019**, *116*, 40.
12. Kim, K.-H.; Moldovan, N.; Espinosa, H. D., A Nanofountain Probe with Sub-100 nm Molecular Writing Resolution. *Small* **2005**, *1*, 632-635.

13. Huo, F.; Zheng, G.; Liao, X.; Giam, L. R.; Chai, J.; Chen, X.; Shim, W.; Mirkin, C. A., Beam pen lithography. *Nat. Nanotechnol.* **2010**, *5*, 637-640.
14. Liao, X.; Brown, K. A.; Schmucker, A. L.; Liu, G.; He, S.; Shim, W.; Mirkin, C. A., Desktop nanofabrication with massively multiplexed beam pen lithography. *Nat. Commun.* **2013**, *4*, 2103.
15. Vazquez-Mena, O.; Sannomiya, T.; Villanueva, L. G.; Voros, J.; Brugger, J., Metallic Nanodot Arrays by Stencil Lithography for Plasmonic Biosensing Applications. *ACS Nano* **2011**, *5*, 844-853.
16. Neiva, E. G. C.; Oliveira, M. M.; Marcolino, L. H.; Zarbin, A. J. G., Nickel nanoparticles with hcp structure: Preparation, deposition as thin films and application as electrochemical sensor. *J. Colloid Interface Sci.* **2016**, *468*, 34-41.
17. Boken, J.; Khurana, P.; Thatai, S.; Kumar, D.; Prasad, S., Plasmonic nanoparticles and their analytical applications: A review. *Appl. Spectrosc. Rev.* **2017**, *52*, 774-820.
18. Zhu, J.; Hu, L.; Zhao, P.; Lee, L. Y. S.; Wong, K.-Y., Recent Advances in Electrocatalytic Hydrogen Evolution Using Nanoparticles. *Chem. Rev.* **2020**, *120*, 851-918.
19. Xiang, X. D.; Sun, X.; Briceño, G.; Lou, Y.; Wang, K.-A.; Chang, H.; Wallace-Freedman, W. G.; Chen, S.-W.; Schultz, P. G., A Combinatorial Approach to Materials Discovery. *Science* **1995**, *268*, 1738.
20. Huang, L.; Chen, P.-C.; Liu, M.; Fu, X.; Gordiichuk, P.; Yu, Y.; Wolverson, C.; Kang, Y.; Mirkin, C. A., Catalyst design by scanning probe block copolymer lithography. *Proc. Natl. Acad. Sci.* **2018**, *115*, 3764.
21. Seol, S. K.; Kim, D.; Lee, S.; Kim, J. H.; Chang, W. S.; Kim, J. T., Electrodeposition-based 3D Printing of Metallic Microarchitectures with Controlled Internal Structures. *Small* **2015**, *11*, 3896-3902.
22. Buchanan, C.; Gardner, L., Metal 3D printing in construction: A review of methods, research, applications, opportunities and challenges. *Eng. Struct.* **2019**, *180*, 332-348.
23. Sui, Y.; Zorman, C. A., Review—Inkjet Printing of Metal Structures for Electrochemical Sensor Applications. *J. Electrochem. Soc.* **2020**, *167*, 037571.
24. Therese, G. H. A.; Kamath, P. V., Electrochemical Synthesis of Metal Oxides and Hydroxides. *Chem. Mater.* **2000**, *12*, 1195-1204.
25. Mahenderkar, N. K.; Chen, Q.; Liu, Y.-C.; Duchild, A. R.; Hofheins, S.; Chason, E.; Switzer, J. A., Epitaxial lift-off of electrodeposited single-crystal gold foils for flexible electronics. *Science* **2017**, *355*, 1203.

26. Yan, Z.; Sun, H.; Chen, X.; Liu, H.; Zhao, Y.; Li, H.; Xie, W.; Cheng, F.; Chen, J., Anion insertion enhanced electrodeposition of robust metal hydroxide/oxide electrodes for oxygen evolution. *Nat. Commun.* **2018**, *9*, 2373.
27. Itaya, K.; Tomita, E., Scanning tunneling microscope for electrochemistry - a new concept for the in situ scanning tunneling microscope in electrolyte solutions. *Surf. Sci.* **1988**, *201*, L507-L512.
28. Li, Y.; Maynor, B. W.; Liu, J., Electrochemical AFM “Dip-Pen” Nanolithography. *J. Am. Chem. Soc.* **2001**, *123*, 2105-2106.
29. Penner, R. M., Mesoscopic Metal Particles and Wires by Electrodeposition. *J. Phys. Chem. B* **2002**, *106*, 3339-3353.
30. Lai, Y.-H.; Park, H. S.; Zhang, J. Z.; Matthews, P. D.; Wright, D. S.; Reisner, E., A Si Photocathode Protected and Activated with a Ti and Ni Composite Film for Solar Hydrogen Production. *Chem. Eur. J.* **2015**, *21*, 3919-3923.
31. Ozel, T.; Bourret, G. R.; Mirkin, C. A., Coaxial lithography. *Nat. Nanotechnol.* **2015**, *10*, 319-324.
32. Hirt, L.; Ihle, S.; Pan, Z.; Dorwling-Carter, L.; Reiser, A.; Wheeler, J. M.; Spolenak, R.; Vörös, J.; Zambelli, T., Template-Free 3D Microprinting of Metals Using a Force-Controlled Nanopipette for Layer-by-Layer Electrodeposition. *Adv. Mater.* **2016**, *28*, 2311-2315.
33. Ozel, T.; Zhang, B. A.; Gao, R.; Day, R. W.; Lieber, C. M.; Nocera, D. G., Electrochemical Deposition of Conformal and Functional Layers on High Aspect Ratio Silicon Micro/Nanowires. *Nano Lett.* **2017**, *17*, 4502-4507.
34. Xu, J.; Ren, W.; Lian, Z.; Yu, P.; Yu, H., A review: development of the maskless localized electrochemical deposition technology. *Int. J. Adv. Manuf. Technol.* **2020**, *110*, 1731-1757.
35. Nyffenegger, R. M.; Penner, R. M., Nanometer-Scale Surface Modification Using the Scanning Probe Microscope: Progress since 1991. *Chem. Rev.* **1997**, *97*, 1195-1230.
36. Seol, S. K.; Pyun, A. R.; Hwu, Y.; Margaritondo, G.; Je, J. H., Localized Electrochemical Deposition of Copper Monitored Using Real-Time X-ray Microradiography. *Adv. Funct. Mater.* **2005**, *15*, 934-937.
37. Hu, J.; Yu, M.-F., Meniscus-Confined Three-Dimensional Electrodeposition for Direct Writing of Wire Bonds. *Science* **2010**, *329*, 313.
38. Hirt, L.; Grüter, R. R.; Berthelot, T.; Cornut, R.; Vörös, J.; Zambelli, T., Local surface modification via confined electrochemical deposition with FluidFM. *RSC Adv.* **2015**, *5*, 84517-84522.

39. Kang, H.; Hwang, S.; Kwak, J., A hydrogel pen for electrochemical reaction and its applications for 3D printing. *Nanoscale* **2015**, *7*, 994-1001.
40. Yun, C.; Kang, H.; Kwak, J.; Hwang, S., Do-It-Yourself Pyramidal Mold for Nanotechnology. *ACS Omega* **2019**, *4*, 14599-14604.
41. Chen, X.; Liu, X.; Ouyang, M.; Chen, J.; Taiwo, O.; Xia, Y.; Childs, P. R. N.; Brandon, N. P.; Wu, B., Multi-metal 4D printing with a desktop electrochemical 3D printer. *Sci. Rep.* **2019**, *9*, 3973.
42. Reiser, A.; Lindén, M.; Rohner, P.; Marchand, A.; Galinski, H.; Sologubenko, A. S.; Wheeler, J. M.; Zenobi, R.; Poulidakos, D.; Spolenak, R., Multi-metal electrohydrodynamic redox 3D printing at the submicron scale. *Nat. Commun.* **2019**, *10*, 1853.
43. Eliyahu, D.; Gileadi, E.; Galun, E.; Eliaz, N., Atomic Force Microscope-Based Meniscus-Confined Three-Dimensional Electrodeposition. *Adv. Mater. Technol.* **2020**, *5*, 1900827.
44. Chen, M.; Lee, H.; Yang, J.; Xu, Z.; Huang, N.; Chan, B. P.; Kim, J. T., Parallel, Multi-Material Electrohydrodynamic 3D Nanoprinting. *Small* **2020**, *16*, 1906402.
45. McCrory, C. C. L.; Jung, S.; Ferrer, I. M.; Chatman, S. M.; Peters, J. C.; Jaramillo, T. F., Benchmarking Hydrogen Evolving Reaction and Oxygen Evolving Reaction Electrocatalysts for Solar Water Splitting Devices. *J. Am. Chem. Soc.* **2015**, *137*, 4347-4357.
46. Ovshinsky, S. R.; Fetcenko, M. A.; Ross, J., A Nickel Metal Hydride Battery for Electric Vehicles. *Science* **1993**, *260*, 176.
47. Jana, M.; Sivakumar, P.; Kota, M.; Jung, M. G.; Park, H. S., Phase- and interlayer spacing-controlled cobalt hydroxides for high performance asymmetric supercapacitor applications. *J. Power Sources* **2019**, *422*, 9-17.
48. Yabuki, A.; Arriffin, N., Electrical conductivity of copper nanoparticle thin films annealed at low temperature. *Thin Solid Films* **2010**, *518*, 7033-7037.
49. Chen, P.-C.; Liu, X.; Hedrick, J. L.; Xie, Z.; Wang, S.; Lin, Q.-Y.; Hersam, M. C.; Dravid, V. P.; Mirkin, C. A., Polyelemental nanoparticle libraries. *Science* **2016**, *352*, 1565.
50. Brown, K. A.; Eichelsdoerfer, D. J.; Liao, X.; He, S.; Mirkin, C. A., Material transport in dip-pen nanolithography. *Front. Phys.* **2014**, *9*, 385-397.
51. Rozhok, S.; Piner, R.; Mirkin, C. A., Dip-Pen Nanolithography: What Controls Ink Transport? *J. Phys. Chem. B* **2003**, *107*, 751-757.
52. Charras, G.; Sahai, E., Physical influences of the extracellular environment on cell migration. *Nat. Rev. Mol. Cell Biol.* **2014**, *15*, 813-824.

53. Yamada, K. M.; Sixt, M., Mechanisms of 3D cell migration. *Nat. Rev. Mol. Cell Biol.* **2019**, *20*, 738-752.
54. Engler, A. J.; Humbert, P. O.; Wehrle-Haller, B.; Weaver, V. M., Multiscale Modeling of Form and Function. *Science* **2009**, *324*, 208.
55. Arnold, M.; Cavalcanti-Adam, E. A.; Glass, R.; Blümmel, J.; Eck, W.; Kantelehner, M.; Kessler, H.; Spatz, J. P., Activation of Integrin Function by Nanopatterned Adhesive Interfaces. *ChemPhysChem* **2004**, *5*, 383-388.
56. Arnold, M.; Hirschfeld-Warneken, V. C.; Lohmüller, T.; Heil, P.; Blümmel, J.; Cavalcanti-Adam, E. A.; López-García, M.; Walther, P.; Kessler, H.; Geiger, B.; Spatz, J. P., Induction of Cell Polarization and Migration by a Gradient of Nanoscale Variations in Adhesive Ligand Spacing. *Nano Lett.* **2008**, *8*, 2063-2069.
57. Deng, J.; Zhao, C.; Spatz, J. P.; Wei, Q., Nanopatterned Adhesive, Stretchable Hydrogel to Control Ligand Spacing and Regulate Cell Spreading and Migration. *ACS Nano* **2017**, *11*, 8282-8291.
58. Lo, C.-M.; Wang, H.-B.; Dembo, M.; Wang, Y.-l., Cell Movement Is Guided by the Rigidity of the Substrate. *Biophys. J.* **2000**, *79*, 144-152.
59. Discher, D. E.; Janmey, P.; Wang, Y.-l., Tissue Cells Feel and Respond to the Stiffness of Their Substrate. *Science* **2005**, *310*, 1139.
60. Peyton, S. R.; Putnam, A. J., Extracellular matrix rigidity governs smooth muscle cell motility in a biphasic fashion. *J. Cell. Physiol.* **2005**, *204*, 198-209.
61. Janson, I. A.; Putnam, A. J., Extracellular matrix elasticity and topography: Material-based cues that affect cell function via conserved mechanisms. *J. Biomed. Mater. Res. A* **2015**, *103*, 1246-1258.
62. Chaudhuri, O.; Gu, L.; Darnell, M.; Klumpers, D.; Bencherif, S. A.; Weaver, J. C.; Huebsch, N.; Mooney, D. J., Substrate stress relaxation regulates cell spreading. *Nat. Commun.* **2015**, *6*, 6365.
63. Zaman, M. H.; Trapani, L. M.; Sieminski, A. L.; MacKellar, D.; Gong, H.; Kamm, R. D.; Wells, A.; Lauffenburger, D. A.; Matsudaira, P., Migration of tumor cells in 3D matrices is governed by matrix stiffness along with cell-matrix adhesion and proteolysis. *Proc. Natl. Acad. Sci.* **2006**, *103*, 10889.
64. Ulrich, T. A.; de Juan Pardo, E. M.; Kumar, S., The Mechanical Rigidity of the Extracellular Matrix Regulates the Structure, Motility, and Proliferation of Glioma Cells. *Cancer Res.* **2009**, *69*, 4167.

65. Levental, K. R.; Yu, H.; Kass, L.; Lakins, J. N.; Egeblad, M.; Erler, J. T.; Fong, S. F. T.; Csiszar, K.; Giaccia, A.; Wenginger, W.; Yamauchi, M.; Gasser, D. L.; Weaver, V. M., Matrix Crosslinking Forces Tumor Progression by Enhancing Integrin Signaling. *Cell* **2009**, *139*, 891-906.
66. Umesh, V.; Rape, A. D.; Ulrich, T. A.; Kumar, S., Microenvironmental Stiffness Enhances Glioma Cell Proliferation by Stimulating Epidermal Growth Factor Receptor Signaling. *PLOS ONE* **2014**, *9*, e101771.
67. Paul, C. D.; Mistriotis, P.; Konstantopoulos, K., Cancer cell motility: lessons from migration in confined spaces. *Nat. Rev. Cancer* **2017**, *17*, 131-140.
68. Wei, S. C.; Fattet, L.; Tsai, J. H.; Guo, Y.; Pai, V. H.; Majeski, H. E.; Chen, A. C.; Sah, R. L.; Taylor, S. S.; Engler, A. J.; Yang, J., Matrix stiffness drives epithelial–mesenchymal transition and tumour metastasis through a TWIST1–G3BP2 mechanotransduction pathway. *Nat. Cell Biol.* **2015**, *17*, 678-688.
69. Winkler, J.; Abisoye-Ogunniyan, A.; Metcalf, K. J.; Werb, Z., Concepts of extracellular matrix remodelling in tumour progression and metastasis. *Nat. Commun.* **2020**, *11*, 5120.
70. Cha, J.; Kim, P., Biomimetic Strategies for the Glioblastoma Microenvironment. *Front. Mater. Sci.* **2017**, *4*.
71. Pathak, A.; Kumar, S., Independent regulation of tumor cell migration by matrix stiffness and confinement. *Proc. Natl. Acad. Sci.* **2012**, *109*, 10334.
72. Singh, S. P.; Schwartz, M. P.; Lee, J. Y.; Fairbanks, B. D.; Anseth, K. S., A peptide functionalized poly(ethylene glycol) (PEG) hydrogel for investigating the influence of biochemical and biophysical matrix properties on tumor cell migration. *Biomater. Sci.* **2014**, *2*, 1024-1034.
73. Wang, C.; Tong, X.; Yang, F., Bioengineered 3D Brain Tumor Model To Elucidate the Effects of Matrix Stiffness on Glioblastoma Cell Behavior Using PEG-Based Hydrogels. *Mol. Pharm.* **2014**, *11*, 2115-2125.
74. Wang, M.; Cheng, B.; Yang, Y.; Liu, H.; Huang, G.; Han, L.; Li, F.; Xu, F., Microchannel Stiffness and Confinement Jointly Induce the Mesenchymal-Amoeboid Transition of Cancer Cell Migration. *Nano Lett.* **2019**, *19*, 5949-5958.
75. Diao, W.; Tong, X.; Yang, C.; Zhang, F.; Bao, C.; Chen, H.; Liu, L.; Li, M.; Ye, F.; Fan, Q.; Wang, J.; Ou-Yang, Z.-C., Behaviors of Glioblastoma Cells in in Vitro Microenvironments. *Sci. Rep.* **2019**, *9*, 85.

76. Zhang, H.; Lin, F.; Huang, J.; Xiong, C., Anisotropic stiffness gradient-regulated mechanical guidance drives directional migration of cancer cells. *Acta Biomater.* **2020**, *106*, 181-192.
77. Vasudevan, J.; Lim, C. T.; Fernandez, J. G., Cell Migration and Breast Cancer Metastasis in Biomimetic Extracellular Matrices with Independently Tunable Stiffness. *Adv. Funct. Mater.* **2020**, *30*, 2005383.
78. Bangasser, B. L.; Shamsan, G. A.; Chan, C. E.; Opoku, K. N.; Tüzel, E.; Schlichtmann, B. W.; Kasim, J. A.; Fuller, B. J.; McCullough, B. R.; Rosenfeld, S. S.; Odde, D. J., Shifting the optimal stiffness for cell migration. *Nat. Commun.* **2017**, *8*, 15313.
79. DuChez, B. J.; Doyle, A. D.; Dimitriadis, E. K.; Yamada, K. M., Durotaxis by Human Cancer Cells. *Biophys. J.* **2019**, *116*, 670-683.
80. Dou, J.; Mao, S.; Li, H.; Lin, J.-M., Combination Stiffness Gradient with Chemical Stimulation Directs Glioma Cell Migration on a Microfluidic Chip. *Anal. Chem.* **2020**, *92*, 892-898.
81. Conklin, M. W.; Eickhoff, J. C.; Riching, K. M.; Pehlke, C. A.; Eliceiri, K. W.; Provenzano, P. P.; Friedl, A.; Keely, P. J., Aligned Collagen Is a Prognostic Signature for Survival in Human Breast Carcinoma. *Am. J. Pathol.* **2011**, *178*, 1221-1232.
82. Ray, A.; Lee, O.; Win, Z.; Edwards, R. M.; Alford, P. W.; Kim, D.-H.; Provenzano, P. P., Anisotropic forces from spatially constrained focal adhesions mediate contact guidance directed cell migration. *Nat. Commun.* **2017**, *8*, 14923.
83. Yaginuma, T.; Kushiro, K.; Takai, M., Unique Cancer Migratory Behaviors in Confined Spaces of Microgroove Topography with Acute Wall Angles. *Sci. Rep.* **2020**, *10*, 6110.
84. Sander, L. M., Modeling Contact Guidance and Invasion by Cancer Cells. *Cancer Res.* **2014**, *74*, 4588.
85. Kubow, K. E.; Shuklis, V. D.; Sales, D. J.; Horwitz, A. R., Contact guidance persists under myosin inhibition due to the local alignment of adhesions and individual protrusions. *Sci. Rep.* **2017**, *7*, 14380.
86. Kloxin, A. M.; Tibbitt, M. W.; Anseth, K. S., Synthesis of photodegradable hydrogels as dynamically tunable cell culture platforms. *Nat. Protoc.* **2010**, *5*, 1867-1887.
87. Yang, C.; DelRio, F. W.; Ma, H.; Killaars, A. R.; Basta, L. P.; Kyburz, K. A.; Anseth, K. S., Spatially patterned matrix elasticity directs stem cell fate. *Proc. Natl. Acad. Sci.* **2016**, *113*, E4439.

88. Ebata, H.; Moriyama, K.; Kuboki, T.; Kidoaki, S., General cellular durotaxis induced with cell-scale heterogeneity of matrix-elasticity. *Biomaterials* **2020**, *230*, 119647.
89. Engler, A. J.; Sen, S.; Sweeney, H. L.; Discher, D. E., Matrix Elasticity Directs Stem Cell Lineage Specification. *Cell* **2006**, *126*, 677-689.
90. Polacheck, W. J.; Zervantonakis, I. K.; Kamm, R. D., Tumor cell migration in complex microenvironments. *Cell. Mol. Life Sci.* **2013**, *70*, 1335-1356.
91. Pathak, A.; Kumar, S., From Molecular Signal Activation to Locomotion: An Integrated, Multiscale Analysis of Cell Motility on Defined Matrices. *PLOS ONE* **2011**, *6*, e18423.
92. Petrie, R. J.; Doyle, A. D.; Yamada, K. M., Random versus directionally persistent cell migration. *Nat. Rev. Mol. Cell Biol.* **2009**, *10*, 538-549.
93. Tinevez, J.-Y.; Perry, N.; Schindelin, J.; Hoopes, G. M.; Reynolds, G. D.; Laplantine, E.; Bednarek, S. Y.; Shorte, S. L.; Eliceiri, K. W., TrackMate: An open and extensible platform for single-particle tracking. *Methods* **2017**, *115*, 80-90.
94. Taipale, J.; Keski-Oja, J., Growth factors in the extracellular matrix. *FASEB J.* **1997**, *11*, 51-59.
95. Dvir, T.; Timko, B. P.; Kohane, D. S.; Langer, R., Nanotechnological strategies for engineering complex tissues. *Nat. Nanotechnol.* **2011**, *6*, 13-22.
96. Strzyz, P., May the force be with you. *Nat. Rev. Mol. Cell Biol.* **2016**, *17*, 533-533.
97. Guilak, F.; Cohen, D. M.; Estes, B. T.; Gimble, J. M.; Liedtke, W.; Chen, C. S., Control of Stem Cell Fate by Physical Interactions with the Extracellular Matrix. *Cell Stem Cell* **2009**, *5*, 17-26.
98. Pittenger, M. F.; Mackay, A. M.; Beck, S. C.; Jaiswal, R. K.; Douglas, R.; Mosca, J. D.; Moorman, M. A.; Simonetti, D. W.; Craig, S.; Marshak, D. R., Multilineage Potential of Adult Human Mesenchymal Stem Cells. *Science* **1999**, *284*, 143.
99. Magin, C. M.; Alge, D. L.; Anseth, K. S., Bio-inspired 3D microenvironments: a new dimension in tissue engineering. *Biomed. Mater.* **2016**, *11*, 022001.
100. Kloxin, A. M.; Kasko, A. M.; Salinas, C. N.; Anseth, K. S., Photodegradable Hydrogels for Dynamic Tuning of Physical and Chemical Properties. *Science* **2009**, *324*, 59.
101. Higuchi, A.; Ling, Q.-D.; Chang, Y.; Hsu, S.-T.; Umezawa, A., Physical Cues of Biomaterials Guide Stem Cell Differentiation Fate. *Chem. Rev.* **2013**, *113*, 3297-3328.

102. Chen, C. S.; Mrksich, M.; Huang, S.; Whitesides, G. M.; Ingber, D. E., Micropatterned Surfaces for Control of Cell Shape, Position, and Function. *Biotechnol. Prog.* **1998**, *14*, 356-363.
103. Jackman, R. J.; Wilbur, J. L.; Whitesides, G. M., Fabrication of submicrometer features on curved substrates by microcontact printing. *Science* **1995**, *269*, 664.
104. Slater, J. H.; Boyce, P. J.; Jancaitis, M. P.; Gaubert, H. E.; Chang, A. L.; Markey, M. K.; Frey, W., Modulation of Endothelial Cell Migration via Manipulation of Adhesion Site Growth Using Nanopatterned Surfaces. *ACS Appl. Mater. Interfaces* **2015**, *7*, 4390-4400.
105. Arnold, M.; Schwieder, M.; Blümmel, J.; Cavalcanti-Adam, E. A.; López-García, M.; Kessler, H.; Geiger, B.; Spatz, J. P., Cell interactions with hierarchically structured nano-patterned adhesive surfaces. *Soft Matter* **2009**, *5*, 72-77.
106. Kim, D.-J.; Seol, J.-K.; Lee, G.; Kim, G.-S.; Lee, S.-K., Cell adhesion and migration on nanopatterned substrates and their effects on cell-capture yield. *Nanotechnology* **2012**, *23*, 395102.
107. Selhuber-Unkel, C.; Erdmann, T.; López-García, M.; Kessler, H.; Schwarz, U. S.; Spatz, J. P., Cell Adhesion Strength Is Controlled by Intermolecular Spacing of Adhesion Receptors. *Biophys. J.* **2010**, *98*, 543-551.
108. Côté, A. P.; Benin, A. I.; Ockwig, N. W.; Keeffe, M.; Matzger, A. J.; Yaghi, O. M., Porous, Crystalline, Covalent Organic Frameworks. *Science* **2005**, *310*, 1166.
109. Smith, B. J.; Parent, L. R.; Overholts, A. C.; Beaucage, P. A.; Bisbey, R. P.; Chavez, A. D.; Hwang, N.; Park, C.; Evans, A. M.; Gianneschi, N. C.; Dichtel, W. R., Colloidal Covalent Organic Frameworks. *ACS Central Science* **2017**, *3*, 58-65.
110. Kim, S.; Park, C.; Lee, M.; Song, I.; Kim, J.; Lee, M.; Jung, J.; Kim, Y.; Lim, H.; Choi, H. C., Rapid Photochemical Synthesis of Sea-Urchin-Shaped Hierarchical Porous COF-5 and Its Lithography-Free Patterned Growth. *Adv. Funct. Mater.* **2017**, *27*, 1700925.
111. Li, Rebecca L.; Flanders, N. C.; Evans, A. M.; Ji, W.; Castano, I.; Chen, L. X.; Gianneschi, N. C.; Dichtel, W. R., Controlled growth of imine-linked two-dimensional covalent organic framework nanoparticles. *Chem. Sci.* **2019**, *10*, 3796-3801.
112. Feriante, C. H.; Jhulki, S.; Evans, A. M.; Dasari, R. R.; Slicker, K.; Dichtel, W. R.; Marder, S. R., Rapid Synthesis of High Surface Area Imine-Linked 2D Covalent Organic Frameworks by Avoiding Pore Collapse During Isolation. *Adv. Mater.* **2020**, *32*, 1905776.
113. Ji, W.; Xiao, L.; Ling, Y.; Ching, C.; Matsumoto, M.; Bisbey, R. P.; Helbling, D. E.; Dichtel, W. R., Removal of GenX and Perfluorinated Alkyl Substances from Water by Amine-Functionalized Covalent Organic Frameworks. *J. Am. Chem. Soc.* **2018**, *140*, 12677-12681.

114. Sun, Q.; Aguila, B.; Perman, J.; Earl, L. D.; Abney, C. W.; Cheng, Y.; Wei, H.; Nguyen, N.; Wojtas, L.; Ma, S., Postsynthetically Modified Covalent Organic Frameworks for Efficient and Effective Mercury Removal. *J. Am. Chem. Soc.* **2017**, *139*, 2786-2793.
115. DeBlase, C. R.; Silberstein, K. E.; Truong, T.-T.; Abruña, H. D.; Dichtel, W. R.,  $\beta$ -Ketoenamine-Linked Covalent Organic Frameworks Capable of Pseudocapacitive Energy Storage. *J. Am. Chem. Soc.* **2013**, *135*, 16821-16824.
116. Mulzer, C. R.; Shen, L.; Bisbey, R. P.; McKone, J. R.; Zhang, N.; Abruña, H. D.; Dichtel, W. R., Superior Charge Storage and Power Density of a Conducting Polymer-Modified Covalent Organic Framework. *ACS Central Science* **2016**, *2*, 667-673.
117. Xu, H.; Gao, J.; Jiang, D., Stable, crystalline, porous, covalent organic frameworks as a platform for chiral organocatalysts. *Nat. Chem.* **2015**, *7*, 905-912.
118. Kaleeswaran, D.; Vishnoi, P.; Murugavel, R., [3+3] Imine and  $\beta$ -ketoenamine tethered fluorescent covalent-organic frameworks for CO<sub>2</sub> uptake and nitroaromatic sensing. *Journal of Materials Chemistry C* **2015**, *3*, 7159-7171.
119. Ma, H.; Ren, H.; Meng, S.; Yan, Z.; Zhao, H.; Sun, F.; Zhu, G., A 3D microporous covalent organic framework with exceedingly high C<sub>3</sub>H<sub>8</sub>/CH<sub>4</sub> and C<sub>2</sub> hydrocarbon/CH<sub>4</sub> selectivity. *Chemical Communications* **2013**, *49*, 9773-9775.
120. Campbell, N. L.; Clowes, R.; Ritchie, L. K.; Cooper, A. I., Rapid Microwave Synthesis and Purification of Porous Covalent Organic Frameworks. *Chem. Mater.* **2009**, *21*, 204-206.
121. Yang, S.-T.; Kim, J.; Cho, H.-Y.; Kim, S.; Ahn, W.-S., Facile synthesis of covalent organic frameworks COF-1 and COF-5 by sonochemical method. *RSC Adv.* **2012**, *2*, 10179-10181.
122. Diercks, C. S.; Lin, S.; Kornienko, N.; Kapustin, E. A.; Nichols, E. M.; Zhu, C.; Zhao, Y.; Chang, C. J.; Yaghi, O. M., Reticular Electronic Tuning of Porphyrin Active Sites in Covalent Organic Frameworks for Electrocatalytic Carbon Dioxide Reduction. *J. Am. Chem. Soc.* **2018**, *140*, 1116-1122.
123. Dey, K.; Pal, M.; Rout, K. C.; Kunjattu H, S.; Das, A.; Mukherjee, R.; Kharul, U. K.; Banerjee, R., Selective Molecular Separation by Interfacially Crystallized Covalent Organic Framework Thin Films. *J. Am. Chem. Soc.* **2017**, *139*, 13083-13091.
124. Du, J. S.; Shin, D.; Stanev, T. K.; Musumeci, C.; Xie, Z.; Huang, Z.; Lai, M.; Sun, L.; Zhou, W.; Stern, N. P.; Dravid, V. P.; Mirkin, C. A., Halide perovskite nanocrystal arrays: Multiplexed synthesis and size-dependent emission. *Science Advances* **2020**, *6*, eabc4959.
125. de la Peña Ruigómez, A.; Rodríguez-San-Miguel, D.; Stylianou, K. C.; Cavallini, M.; Gentili, D.; Liscio, F.; Milita, S.; Roscioni, O. M.; Ruiz-González, M. L.; Carbonell, C.; MasPOCH, D.; Mas-Ballesté, R.; Segura, J. L.; Zamora, F., Direct On-Surface Patterning of a

Crystalline Lamellar Covalent Organic Framework Synthesized at Room Temperature. *Chem. Eur. J.* **2015**, *21*, 10666-10670.

126. Tilstam, U., Sulfolane: A Versatile Dipolar Aprotic Solvent. *Organic Process Research & Development* **2012**, *16*, 1273-1278.

127. Ma, T.; Kapustin, E. A.; Yin, S. X.; Liang, L.; Zhou, Z.; Niu, J.; Li, L.-H.; Wang, Y.; Su, J.; Li, J.; Wang, X.; Wang, W. D.; Wang, W.; Sun, J.; Yaghi, O. M., Single-crystal x-ray diffraction structures of covalent organic frameworks. *Science* **2018**, *361*, 48.

128. Wang, S.; Zhang, Z.; Zhang, H.; Rajan, A. G.; Xu, N.; Yang, Y.; Zeng, Y.; Liu, P.; Zhang, X.; Mao, Q.; He, Y.; Zhao, J.; Li, B.-G.; Strano, M. S.; Wang, W.-J., Reversible Polycondensation-Termination Growth of Covalent-Organic-Framework Spheres, Fibers, and Films. *Matter* **2019**, *1*, 1592-1605.

## CURRICULUM VITAE

# EunBi Oh

2190 Campus Drive, Evanston, IL 60208 | 847-977-3820 | eunoh2019@u.northwestern.edu

## EDUCATION

---

### Northwestern University

*Doctor of Philosophy in Chemistry*

Advisor and Committee Members: Chad A. Mirkin, Milan Mrksich, and Emily A. Weiss

*Evanston, Illinois*

*Expected: August 2021*

### University of North Carolina at Chapel Hill

*Honors Bachelor of Science in Chemistry*

Advisor: James F. Cahoon

*Chapel Hill, North Carolina*

*May 2015*

## RESEARCH EXPERIENCE

---

### Research Assistant

*Mirkin Research Lab, Northwestern University*

*Fall 2015-Current*

- Developed a new lithographic architecture for fabricating 3D metallic structures at multiple length scales in high throughput
- Investigated a platform for programming cellular behavior *via* bio-responsive patterns generated on soft materials
- Analyzed the mechanical characteristics of DNA assembled nanocrystals
- Mentored and trained 5 graduate and undergraduate students, guiding in experimental design, scientific writing and presentations, and general laboratory work
- Authored annual reports and presentations for multimillion-dollar research grants from the U.S. Department of Defense
- Managed 2 group instruments (Atomic Force Microscope and Confocal Microscope), training group members, troubleshooting technical errors, and developing operating procedures

*Cahoon Research Lab, University of North Carolina at Chapel Hill*

*Fall 2012-Summer 2015*

- Analyzed the structure-function relationships of nanoparticles
- Fabricated p-type Dye-Sensitized Solar Cells (DSSCs) and examined their electrical properties

## PUBLICATIONS AND PRESENTATIONS

---

### Publications

*Published*

- **E. Oh**, R. Golnabi, D. Walker, C. A. Mirkin. "Electrochemical Polymer Pen Lithography." *Small Accepted (2021)*
- P. A. Gabrys, S. E. Seo, M. X. Wang, **E. Oh**, R. J. Macfarlane, C. A. Mirkin. "Lattice Mismatch in Crystalline Nanoparticle Thin Films." *Nano Lett.* 18, 579-585 (2017)
- C. J. Flynn, S. M. McCullough, **E. Oh**, L. Li, C. C. Mercado, B. H. Farnum, W. Li, C. L. Donley, W. You, A. J. Nozik, J. R. McBride, T. J. Meyer, Y. Kanai, J. F. Cahoon. "Site-Selective

Passivation of Defects in NiO Solar Photocathodes by Targeted Atomic Deposition." *ACS Appl. Mater. Interfaces* 8, 4754–4761 (2016)

- C. J. Flynn, **E. Oh**, S. M. McCullough, R. W. Call, C. L. Donley, R. Lopez, J. F. Cahoon. "Hierarchically-Structured NiO Nanoplatelets as Mesoscale p-Type Photocathodes for Dye-Sensitized Solar Cells. *J. Phys. Chem. C* 118,14177-14184 (2014)

#### *Submission Pending*

- **E. Oh**, B. Meckes, J. Chang, D. Shin, C. A. Mirkin. "Controlled Cancer Cell Confinement and Migration Using Biomimetic Patterned Hydrogels."
- S. Lee, H. Calcaterra, S. Lee, B. Lee, **E. Oh**, C. A. Mirkin. "Hyper-elastic Crystalline-amorphous Transitions of Colloidal Crystals Engineered with DNA."
- N. Ramani, C. A. Figg, **E. Oh**, C. A. Mirkin. "Patterning DNA in Hydrogels using Post-polymerization Functionalization."
- D. Shin, M. Shin, J. S. Du, M. Lai, **E. Oh**, V. P. Dravid, B. Shin, C. A. Mirkin. "High Efficiency of Single-Crystalline Halide Perovskite."

#### **Patents**

- C.A. Mirkin, R. Golnabi, **E. Oh**, D. Walker. "Electrochemical Polymer Pen Lithography" Application Number: 63/142829. Filed January 28, 2021.

#### **Presentations**

- "Mesoscale NiO Platelets as Wide Bandgap Metal Oxide Films for p-Type Dye Sensitized Solar Cells," American Chemical Society-North Carolina Section's 128th Local Section Conference, Poster Presentation, November 7, 2014.

## **SKILLS**

---

#### **Technical skills:**

- **Analytical Techniques:** High-performance Liquid Chromatography, Inductively Coupled Plasma, Potentiostat, Profilometer, Solar Simulator, Source Measure Unit
- **Fabrication Techniques:** Atomic Layer Deposition, Clean Room, E-Beam and Thermal Evaporator, Maskless and Mask Aligner, Photolithography, Scanning Probe Lithography
- **Microscopy:** Atomic Force Microscopy, Confocal and Optical Microscopy, Scanning Electron Microscopy, Transmission Electron Microscopy
- **Spectroscopy:** Infrared Spectroscopy, Nuclear Magnetic Resonance Spectroscopy, Ultraviolet-visible Spectroscopy
- **Synthetic and Other Techniques:** Wet-Chemical Nanoparticle Synthesis, Cell Culture, Quantitative Polymerase Chain Reaction (qPCR)

**Software:** Adobe Illustrator, Adobe Photoshop, AutoCAD, ChemDraw, Cinema 4D, Image J, Microsoft Office, Origin, Prism

## **TEACHING**

---

#### **Teaching Assistant**

*Kellogg MBA Course: Leadership in Organizations, Northwestern University*

*Summer 2019*

- Led a recitation class where students learned essential elements of high performing teams
- Evaluated and provided feedback to students' midterm/final exams and assignments
- Designed and implemented a gradebook model for departmental use in Excel

*Chemistry Organic Labs and Courses, Northwestern University* *Fall 2015-Winter 2016*

- Instructed lab sessions of 10-12 students and taught basic laboratory skills and chemistry concepts
- Advised students in one-on-one meetings and provided evaluations on their progress and lab reports

### **Tutor**

*Chemistry Course: Special Problems, University of North Carolina at Chapel Hill* *Fall 2013-Winter 2015*

- Taught general chemistry topics to non-chemistry major students

## **AWARDS AND HONORS**

---

- KOFST Net Seminar Grant— Korean Federation of Science & Technology Societies, 2018
- James Maguire Memorial Award— University of North Carolina at Chapel Hill, 2014
- Thurman Freeze Research Scholarship— University of North Carolina at Chapel Hill, 2013
- Dean's List— University of North Carolina at Chapel Hill, 2012-2015

## **LEADERSHIP AND COMMUNITY ENGAGEMENT**

---

**Women in Science and Engineering Research (WISER), Northwestern University** *Evanston, Illinois*  
*Treasurer* *Fall 2018-Summer 2019*

- Managed annual budget of \$2-3K and created expense reports for a group of over 500 members
- Communicated with Northwestern finance office to administer transactions and maintain the group's account
- Collaborated with 6 executives and 8 board members to plan and organize faculty seminars and symposiums

**Memorial Hospital, Northwestern University** *Evanston, Illinois*  
*Volunteer (~ 85 hr)* *May 2018-December 2018*

- Supported service to patients and emergency department (ED) nurses; addressed patients' non-medical needs and status, assisted with transportation, and provided directions to rooms and departments

**Korean Student Association (KSA), Northwestern University** *Evanston, Illinois*  
*President* *Fall 2016-Summer 2017*  
*Secretary* *Fall 2015-Summer 2016*

- Raised \$2K to fund networking events and seminars for over 200 Korean graduate students and postdocs at Northwestern
- Developed relationships with chemical, pharmaceutical, and consulting companies in Korea to organize recruiting events
- Facilitated establishment of KSA as an official Northwestern organization; served as a contact point between KSA and school officials

**ORIGINAL RESEARCH PROPOSAL**

Full Original Research Proposal

**Proposal Title: Water Oxidation at Neutral pH Using Bioinspired Mn-based Polypeptides**

**I. ABSTRACT**

The development of active catalysts that are inexpensive and abundant yet best performing has been a long-standing goal of the energy communities, especially for water splitting towards hydrogen evolution. Manganese (Mn)-based catalysts have attracted significant attention in the past decades due to the outstanding performance of naturally occurring  $Mn_4CaO$  clusters in the oxygen-evolving complex (OEC) in photosystem II of the chloroplast. This Ca-containing tetrameric Mn complex is surrounded by polypeptides, which allow it to efficiently catalyze water oxidation at neutral pH with a low electrochemical overpotential ( $\sim 160$  meV). Due to its structural complexity, however, only a few synthetic Mn catalysts have biomimetic structures, and they often require extremely basic conditions, which are not available in a natural system. Therefore, to develop a bioinspired catalyst that can effectively reduce the overpotential and function at pH-neutral conditions—moreover, at room temperature, it is important to understand the role of polypeptides in OEC system and explore the full range of structure-activity relationships for catalyst constructs. This proposal aims to overcome the current major limitations in designing and screening effective electrocatalysts for water oxidation. We propose to build a megalibrary of Mn-based polypeptide clusters based on the sequences found in natural OEC complex in conjunction with a high-throughput screening method coupled with a supervised machine learning algorithm. This screening platform will rapidly determine the sequence and composition of the peptides with high activity and help elucidate the mechanistic role of peptides in water oxidation, providing new design rules toward high-performance catalysts for artificial photosynthetic systems.

## II. INTRODUCTION, BACKGROUND, AND SIGNIFICANCE

As we face the dawn of the 4<sup>th</sup> industrial revolution with cutting-edge technologies that significantly improved the quality of our lives, the global energy demand is exponentially increasing.<sup>2</sup> The traditional sources that dominate the current market, including oil, coal, and natural gas, however, cause major environmental issues and deplete within 150 years or so.<sup>3</sup> To address the environmental problems and the need for the ever-growing consumption of energy sources, the development of renewable energy sources is indispensable and inevitable; accordingly, many researchers have investigated and explored novel materials and engineering processes for green renewable energy.<sup>2-5</sup>

One of the promising renewable energy sources is sunlight; nature has survived and thrived for approximately 3.5 billion years, harvesting most of its energy from the Sun.<sup>2, 5</sup> Through a process called photosynthesis, most plants capture the light energy, store it in the form of chemical bonds, and produce carbon-based energy molecules such as glucose.<sup>2</sup> To convert solar energy into chemical energy, a fuel-forming reaction is needed especially using the abundant and cheap feedstock. In natural photosynthesis, water is utilized and split to produce hydrogen and oxygen gases, as shown by the reaction in equation 1.<sup>3, 6</sup>



The reaction process above is called water splitting and can be described by two half-reactions below:



The first equation is known as the oxygen evolution reaction (OER)—often described as the water oxidation process as well, and the second one is called the hydrogen evolution reaction (HER).

The process for splitting water is thermodynamically unfavorable and challenging, requiring high potentials. Although the theoretical minimum energy required is 1.23 V at room temperature, in order to perform the reaction in timely manner, additional input energy, also known

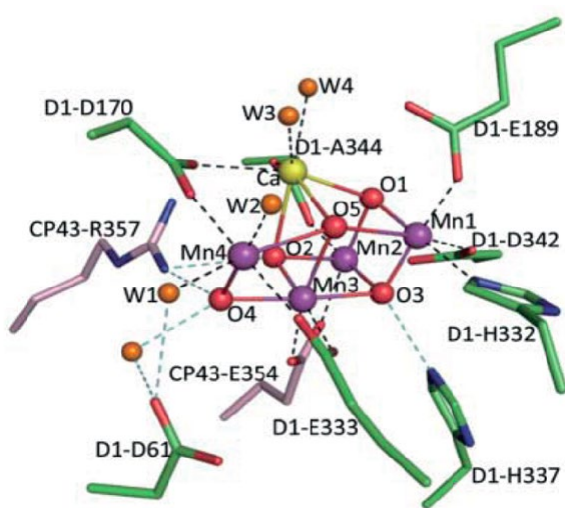


**Figure 1.** The structure of a  $\text{Mn}_4\text{CaO}_x$  cluster based on X-ray diffraction data.<sup>1</sup>

as overpotential, is necessary.<sup>2</sup> To reduce this overpotential, the nature uses a Ca-containing tetranuclear manganese (Mn) cluster ( $\text{Mn}_4\text{CaO}_5$ ) in the oxygen-evolving complex (OEC) of photosystem II to efficiently catalyze the water oxidation process.<sup>5</sup> This Mn complex (**Figure 1**) is capable of oxidizing water with a low electrochemical overpotential of ~160 mV and a high turnover frequency of  $100 \text{ s}^{-1}$  at pH 5-6.5.<sup>1, 7-9</sup> In addition to its high efficiency, manganese is also earth-abundant, inexpensive, and environmentally friendly, which motivates the development and investigation of biomimetic Mn-based catalysts for water oxidation.<sup>2, 5</sup>

Due to its complex structures, however, it is very difficult to design water-oxidizing catalysts that not only mimic the structure and function of the natural Mn cluster, but also are efficacious at neutral conditions. Most synthetic water oxidation catalysts require strongly basic conditions (pH 12-14) for efficient catalysis.<sup>2, 10</sup> However, a moderate pH is safer and results in a slow decomposition rate or degradation of semiconductor materials used in artificial

as overpotential, is necessary.<sup>2</sup> To reduce this overpotential, the nature uses a Ca-containing tetranuclear manganese (Mn) cluster ( $\text{Mn}_4\text{CaO}_5$ ) in the oxygen-evolving complex (OEC) of photosystem II to efficiently catalyze the water oxidation process.<sup>5</sup> This Mn complex (**Figure 1**) is capable of oxidizing water with a low electrochemical overpotential of ~160 mV and a high turnover frequency of  $100 \text{ s}^{-1}$  at pH 5-

photosynthetic devices, which is crucial for long-term performance. The current record Mn-based catalyst that can operate at neutral pH has an electrochemical overpotential around 350 mV, still higher than the natural OEC by a factor of two.<sup>2, 6, 11, 12</sup>

### III. SCIENTIFIC OBJECTIVES

#### AIM 1:

- Design and synthesize a megalibrary of Mn complexes with peptide ligands of varying amino acid sequences, length, and size. The initial peptide sequences will include the ones found in the natural Mn cluster.

#### AIM 2:

- Develop a high-throughput screening platform and measure the catalytic activities of the synthesized Mn-based polypeptide clusters to determine the best working peptide sequences and structures at neutral pH.

#### AIM 3:

- Incorporate supervised machine learning models to predict the activities of the catalysts with possible combinations of key design parameters of the peptide ligands, including hydrophilicity, charge, Hammett constant, and folding.
- Based on the prediction, analyze the redox properties, coordination chemistry, and proton-electron transfer process between the metal center and the peptide ligands of the most active catalyst.

## IV. PREVIOUS WORK

### Previous studies on the structure-function relationship of polypeptides in OEC

The efficient and high catalytic activity of the Mn cluster can be explained by the stabilization of high valent intermediate Mn species through the oxo-bridged cubane structure and nearby peptide ligands.<sup>6</sup> The catalytically relevant peptide sequences in the natural OEC have been identified as Alanine (Ala), Aspartic acid (Asp), Glutamic acid (Glu), Tyrosine (Tyr), Histidine (His), and Serine (Ser).<sup>1, 3, 13, 14</sup> One His residue is known to be directly coordinated to Mn. According to 1.9 Å XRD structure, all Mn ions are hexacoordinated, and bidentate coordination exists between Mn and the carboxylate groups from Asp, Glu, and Ala.<sup>1</sup>

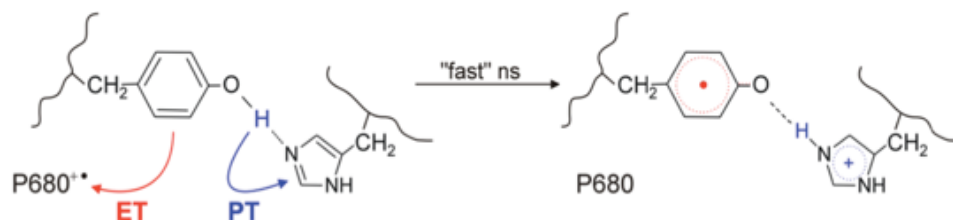


**Figure 2.** Proposed mechanism of proton-coupled electron transfer *via* peptide ligands. Figure adapted from ref. 15.

These surrounding polypeptides are known to play a significant role in proton-coupled electron transfer. The proposed mechanism is briefly outlined in **Figure 2**. The Mn cluster, during the water oxidation process, transfers four electrons from water to a Tyr 161 peptide in  $Y_z$  protein complex, which then transfers those electrons to P680, a type of chlorophyll *a* in photosystem II.<sup>15</sup> Although the Tyr 161 residue from the  $Y_z$  protein complex (one of the redox-active proteins) captures electrons from Mn, it is not directly coordinated to the metal. D1-His residue plays a role in proton transfer. Tyr in  $Y_D$  core protein (adjacent to  $Y_z$ ) has been reported to provide electrostatic

stabilization and facilitate the  $Y_z$  redox process. Carboxylate groups of Asp, Glu, and Ala are known to play a role in buffering, chelating, and electron transfer.<sup>16, 17</sup>

### **Ligand designs and its water oxidation chemistry at neutral pH**

Some relevant variables crucial to efficient water oxidation include protein hydrophilicity, charge, and size, all of which can modulate the coordination and structural flexibility of Mn complexes at neutral pH.<sup>17</sup> Specifically, as the rate-limiting step in water oxidation at neutral pH is reportedly the unfavorable transition from Mn(II) to Mn(III), designing the ligand chemistry to stabilize the Mn(III) oxidation state can improve the rate of reaction.<sup>9</sup>

Recently, the synthesis of a  $Mn_{12}$  cluster that is soluble (and stable) in water and operating at pH 6 with a low overpotential of 334 mV was reported. Using a bulky and hydrophilic ligand, 3,5-dihydroxybenzoic acid, the Christou group was able to dissolve the  $Mn_{12}$  complex in water and stabilize it under neutral pH conditions.<sup>6</sup> The overpotential of this catalyst, however, is still higher than the natural OEC by a factor of 2, which motivates further investigations.

Past research typically involved designing and synthesizing a single Mn polypeptide complex at a time, and a high-throughput screening method has been rarely used to investigate the structure-function relationship of the catalyst complexes in a library platform. There is currently only one example where a library of 14 Zn-polypeptide complexes was synthesized, and their properties as esterification catalysts were investigated (**Figure 3**).<sup>18</sup>

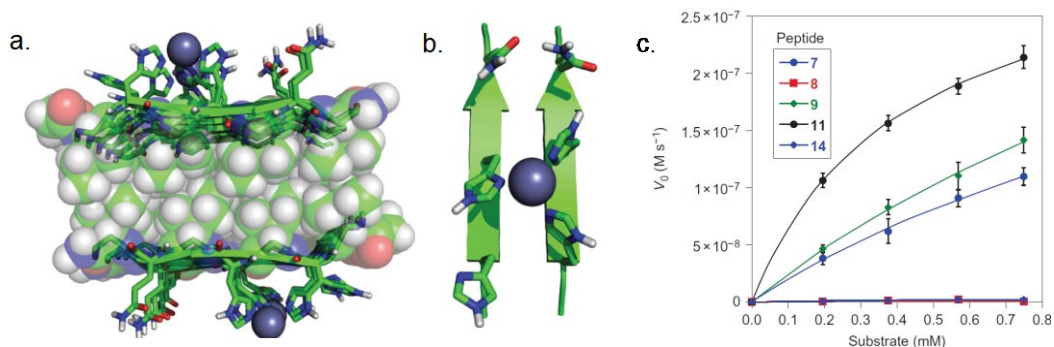


**Figure 3.** The library of Zn-polypeptide complexes and their esterase activities at pH 8. (a) the overall folding of the Z-polypeptide complex, (b) primary zinc coordination, and (c) increasing esterase activity of several representative peptides. The most active peptide is labeled 11 from the library. Entire figure adapted from ref. 18.

## V. PROPOSED RESEARCH

### Mn-peptide complex libraries: a new platform for studying the water oxidation mechanism

By changing the amino acid sequences in a systematic manner, the peptide chain folding, oxidation state, coordination number, and flexibility of Mn complexes can be modulated (**Figure 4**).<sup>4, 8, 11, 19, 20</sup> Upon development, this library of peptide-based Mn complexes will help to determine which factors are dominant in the catalytic process and elucidate the mechanistic role of peptides in water oxidation catalysis. The following questions will be posed and answered: (1) how the peptide ligand chemistry contributes to the geometry of Mn complexes (2) how do the electronic structures and redox properties of Mn change in response to different amino acid sequences.

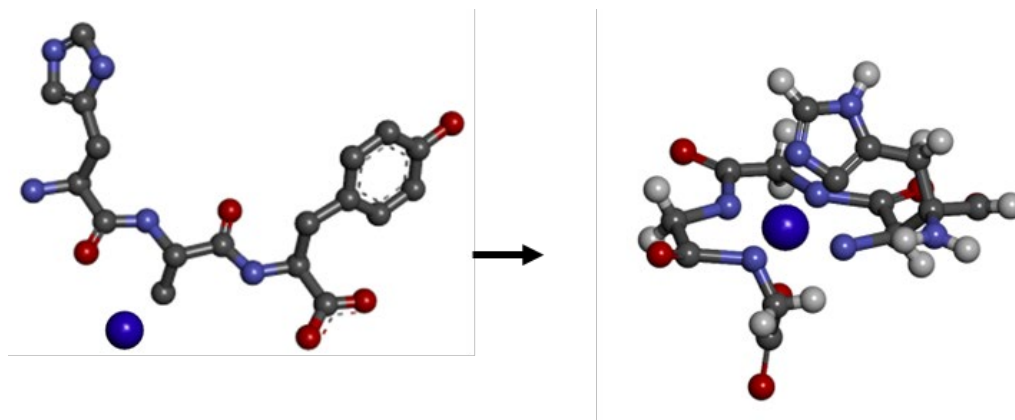


**Figure 4.** Example of the peptide folding induced by the interaction between the metal ion core and the residues of the surrounding polypeptide chains. Using various peptide ligands, the functional properties of Mn complexes can be modified.

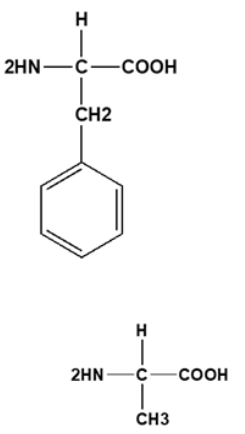
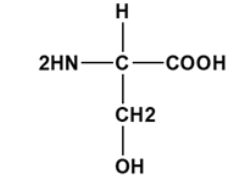
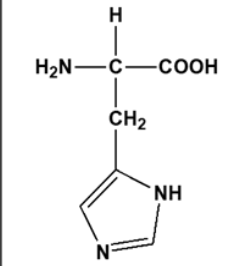
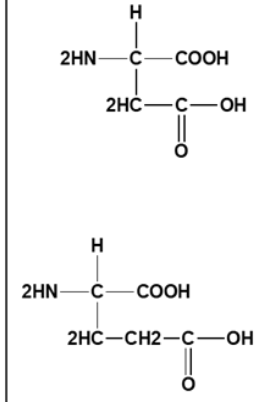
### **Aim 1: Development of a peptide-based Mn (II) complex library**

For the metal ion source, water-soluble  $\text{MnCl}_2$  or  $\text{MnSO}_4$  solids will be used to synthesize the mononuclear Mn (II) complex. Using the amino sequences found in the natural OEC (Ala, Asp, Glu, Tyr, Ser, and His), the initial peptide ligands will be developed. As the initial benchmark, the His- $X_{aa}$ -His ( $X_{aa}$  = amino acid) motif—the previously reported sequence for copper peptide structure<sup>3</sup>—will be used.<sup>4</sup> The side chain of histidine, imidazole with pKa around 6.04, will be deprotonated at neutral pH and readily coordinate with metal ion. The library will be expanded systematically by modulating the number of histidine residues and  $X_{aa}$ ; they will be arranged in a variety of configurations (i.e., His- $X_{aa}$ -His vs. His- $X_{aa}$ - $X_{aa}$ -His, etc.).

In addition, the type of  $X_{aa}$  amino acid will be varied based on the screening result and machine learning predictions. To outline some of the characteristics of each amino acid that will be used as  $X_{aa}$  amino acid, the side chain of Ala can promote hydrophobic interaction within the peptide ligands where Ser and Tyr amino acids will form a hydrogen bond. Both Ser and Tyr carry a hydroxyl group and are therefore considered polar amino acids. The interactions between the

positively and negatively charged side chains of amino acids will form salt bridges, which can have an impact on the stabilization of the catalyst structure. At neutral pH, Asp and Glu amino acids are negatively charged. The properties of amino acids that will be used as design parameters for polypeptide-based Mn complexes are categorized in **Table 1**. In addition to these six amino acids in the table, other remaining 14 amino acids can be systematically added to the peptide ligands to enhance the catalytic activity. The arrangement of these amino acids in His-(X<sub>aa</sub>)<sub>n</sub>-His

**Table 1.** Classification of amino acid residues by the properties of their functional groups. Amino acids can be classified into four major groups, containing either hydrophobic, polar, positive charge, or negative charge side chains.

Hydrophobic	Polar	Positive Charge	Negative Charge
			

motif is expected to modify the hydrophilicity, charge, and size of the metal complex, all of which can modulate the coordination and structural flexibility of Mn complexes. The synthesized Mn (II) complexes will be classified into either water soluble or insoluble complexes, and the best working catalyst will be selected from each category. The peptides will be synthesized using either a peptide synthesizer or standard solid-phase peptide synthesis (SPPS) procedures. For SPPS, Fmoc/tBu strategy will be utilized with p-alkoxybenzyl alcohol as the resin.

When manganese ions are interacting with the synthesized peptide ligands, not only the N-terminus and the carboxyl group, but also the side chains can coordinate with the metal ion and have an impact on the electrochemical properties of the Mn complexes. Therefore, after screening the catalyst with the highest activity (the most O<sub>2</sub> formation), it is important to delineate the structure and scrutinize the coordination chemistry between the peptide ligands and metal center—the structural analysis methods are covered in **Aim 3** below.

### **Aim 2: High-throughput screening of catalytic activities**

In order to rapidly screen the catalytic activities of the synthesized polypeptide-based Mn complexes in a library, it is essential to develop a high-throughput method or assay that can measure and quantify the responses of the catalysts at neutral pH. A large well plate<sup>21</sup> (96, 384, or 1536) will be first fabricated as shown in **Figure 5a**. To each well containing the electrolyte

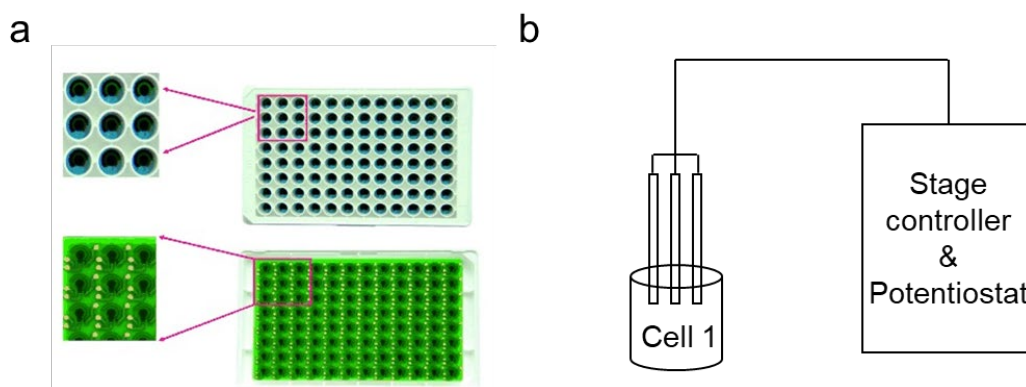


**Figure 5.** Schematic of high-throughput screening approach. (a) 3D printed 96 well plate that can be used to perform electrochemical reactions. (b) A three-electrode cell connected to a stage controller and potentiostat. Panel **a** adapted from ref. 21.

solution, manganese ion precursors with different numbers or types of polypeptide ligands will be added. Some examples of electrolyte solutions include aqueous acetate buffer at pH 6, HEPES buffer, MOPS buffer, and phosphate buffer. All electrochemical analyses will be performed using

a conventional three-electrode system with a glassy carbon electrode as the working electrode, a Pt wire as counter electrode, and a Ag/AgCl as a reference electrode. In order to perform electrolysis in a systematic manner, the electrode cell needs to be coupled to a piezo or stage controller that can move the cell in all x, y, and z directions (**Figure 5b**).

To analyze the catalytic activity at the neutral pH range, cyclic voltammetry experiments will be performed. Before each measurement, a stream of either N<sub>2</sub> or Ar gases will be bubbled into the electrolyte solution containing Mn ions and peptides. Using the controlled potential electrolysis and scan rate experiments, the turnover number (TON), faradic efficiency, and redox properties will be determined and analyzed. The electrochemical stability of the catalysts will be evaluated based on the chronoamperometry data. Using this screening method, the structure-function relationship between the metal ion core and polypeptide ligands can be investigated in conjunction with the machine learning process.

In a natural OEC system, only two water molecules can coordinate to the Mn ion center, although Mn complexes are surrounded by the vast amount of water molecules. These coordinated water molecules are known to be the primary source of O<sub>2</sub> during the water oxidation process.<sup>3</sup> In this study, we also hope to increase the number of binding sites for water molecules using the side chains of the polypeptide ligands. In order to measure how much O<sub>2</sub> has been released per well, an optic fiber O<sub>2</sub> sensor will be used during controlled potential electrolysis. The fiber sensor can be integrated into a needle which then can be inserted into a three-electrode cell at the anode part. Calibration of the sensor with the known oxygen level is important to measure the exact amount of O<sub>2</sub> being released during water oxidation. A fluorescence-based O<sub>2</sub> sensor, or gas chromatography can also be utilized to measure and detect oxygen levels in the system.

**Aim 3:****Integration of machine learning**

Machine learning is a type of data analysis that uses algorithms to make classifications and predictions from input data. There are two types of machine learning methods: supervised learning vs. unsupervised learning. The main difference is whether the input data is labeled or not. Because our screening data is labeled, we will be utilizing the supervised learning model to classify the results and predict the outcome. The noisy target-based system will be used to further control the weight of each factor to precisely optimize the peptide design we would like to pursue.

Recently, there has been extensive work to predict chemical reactivity and reactions using machine learning.<sup>22, 23</sup> For example, the Cronin group fabricated an organic synthesis robot that can autonomously perform chemical reactions and combined the robot with machine learning for decision-making purposes, assessing the reaction, and predicting more than 1,000 reaction

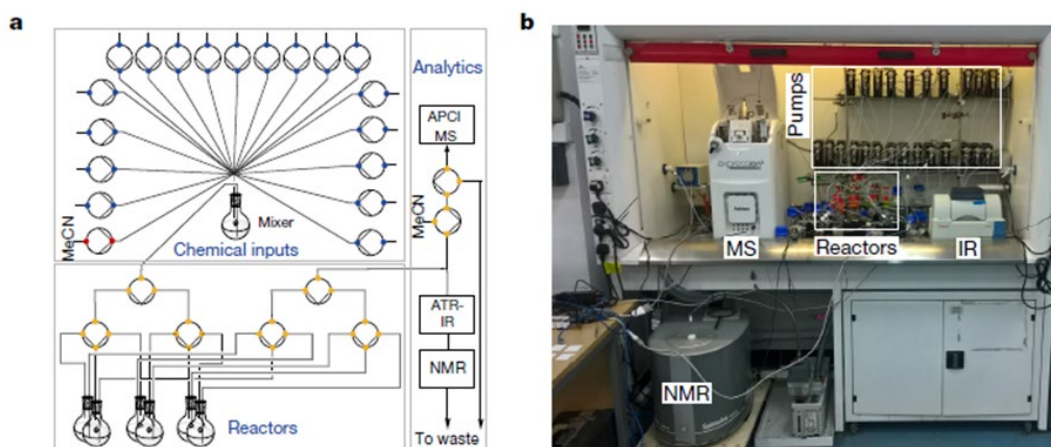


**Figure 6.** (a) Schematic diagram of the robot that can autonomously perform organic synthesis. (b) Image of the actual setup of the chemical robot with labeled compartments. Entire figure adapted from ref. 23.

combinations.<sup>23</sup> To evaluate the reaction outcome in real time, the robot has been integrated with nuclear magnetic resonance and infrared spectroscopy (**Figure 6**). Using a similar platform, we

plan to develop a workstation that is coupled to some of the real-time sensors, including potentiostat, electrochemical in-situ Raman and UV-Vis, and a gas probe. From the resulting dataset, the catalysts can be initially classified as reactive and non-reactive, and the best performing one can be selected from the reactive group. Based on this result, a new set of reaction conditions can be predicted and tested for performance. The cycle will be repeated until all the design parameters have been tested.

### **Characterization of the redox mechanism and coordination chemistry**

The kinetics and catalytic activity of the complex can be measured with electrochemical in-situ Raman in a three-electrode cell setup. The in-situ Raman can provide information about the bonding nature between the water intermediate species (e.g, oxo-bridge) and manganese ion, which can be used to effectively control the weight function in machine learning for the gradient descent optimization process. The oxidation state of the Mn ion in the intermediate species is also important in water oxidation, and it can be analyzed using X-ray absorption spectroscopy (XAS), and X-ray emission spectroscopy (XES). The most common oxidation states of manganese ions found in natural OEC are II, III, and IV. As mentioned in the background section, the stabilization of Mn (III) species during the water oxidation process can enhance the rate of reaction. Those techniques can be used to probe the structure and the valency change in the manganese ions and the coupled protons. In addition, the crystal structure of the product can be examined by single crystal X-ray powder diffraction (XRD), Electrospray ionization-mass spectrometry (ESI-MS), Fourier-transform infrared spectroscopy (FTIR), and Electron paramagnetic resonance (EPR).

## VI. SUMMARY AND CONCLUSIONS

In order to synthesize a biomimicking Mn-based catalyst, it is important to elucidate the underlying mechanism of the natural Mn cluster in the OEC system. By building a library of polypeptide-based Mn molecules and systematically screening their catalytic activities, the key factors influencing the performance of the catalyst will be determined. The peptide sequences, coordination chemistry, and structural organizations will be probed to delineate any structure-activity correlations that will be helpful in designing the catalysts for artificial photosynthetic devices.

## VII. REFERENCES

1. Umena, Y.; Kawakami, K.; Shen, J.-R.; Kamiya, N., Crystal structure of oxygen-evolving photosystem II at a resolution of 1.9 Å. *Nature* **2011**, *473*, 55-60.
2. Roger, I.; Shipman, M. A.; Symes, M. D., Earth-abundant catalysts for electrochemical and photoelectrochemical water splitting. *Nat. Rev. Chem.* **2017**, *1*, 0003.
3. Najafpour, M. M.; Renger, G.; Holyńska, M.; Moghaddam, A. N.; Aro, E.-M.; Carpentier, R.; Nishihara, H.; Eaton-Rye, J. J.; Shen, J.-R.; Allakhverdiev, S. I., Manganese Compounds as Water-Oxidizing Catalysts: From the Natural Water-Oxidizing Complex to Nanosized Manganese Oxide Structures. *Chem. Rev.* **2016**, *116*, 2886-2936.
4. Park, G. Y.; Lee, J. Y.; Himes, R. A.; Thomas, G. S.; Blackburn, N. J.; Karlin, K. D., Copper–Peptide Complex Structure and Reactivity When Found in Conserved His-Xaa-His Sequences. *J. Am. Chem. Soc.* **2014**, *136*, 12532-12535.
5. Brudvig, G. W., Catalysing water oxidation using nature's metal. *Nat. Catal.* **2018**, *1*, 10-11.
6. Maayan, G.; Gluz, N.; Christou, G., A bioinspired soluble manganese cluster as a water oxidation electrocatalyst with low overpotential. *Nat. Catal.* **2018**, *1*, 48-54.
7. Loll, B.; Kern, J.; Saenger, W.; Zouni, A.; Biesiadka, J., Towards complete cofactor arrangement in the 3.0 Å resolution structure of photosystem II. *Nature* **2005**, *438*, 1040-1044.
8. Yano, J.; Kern, J.; Sauer, K.; Latimer, M. J.; Pushkar, Y.; Biesiadka, J.; Loll, B.; Saenger, W.; Messinger, J.; Zouni, A.; Yachandra, V. K., Where Water Is Oxidized to Dioxygen: Structure of the Photosynthetic Mn<sub>4</sub>Ca Cluster. *Science* **2006**, *314*, 821.
9. Jin, K.; Park, J.; Lee, J.; Yang, K. D.; Pradhan, G. K.; Sim, U.; Jeong, D.; Jang, H. L.; Park, S.; Kim, D.; Sung, N.-E.; Kim, S. H.; Han, S.; Nam, K. T., Hydrated Manganese(II) Phosphate (Mn<sub>3</sub>(PO<sub>4</sub>)<sub>2</sub>·3H<sub>2</sub>O) as a Water Oxidation Catalyst. *J. Am. Chem. Soc.* **2014**, *136*, 7435-7443.
10. Nocera, D. G., The Artificial Leaf. *Acc. Chem. Res.* **2012**, *45*, 767-776.

11. Kanan, M. W.; Nocera, D. G., In Situ Formation of an Oxygen-Evolving Catalyst in Neutral Water Containing Phosphate and Co  $2+$ . *Science* **2008**, *321*, 1072.
12. Guan, J.; Duan, Z.; Zhang, F.; Kelly, S. D.; Si, R.; Dupuis, M.; Huang, Q.; Chen, J. Q.; Tang, C.; Li, C., Water oxidation on a mononuclear manganese heterogeneous catalyst. *Nat. Catal.* **2018**, *1*, 870-877.
13. Mukhopadhyay, S.; Mandal, S. K.; Bhaduri, S.; Armstrong, W. H., Manganese Clusters with Relevance to Photosystem II. *Chem. Rev.* **2004**, *104*, 3981-4026.
14. Yano, J.; Walker, L. M.; Strickler, M. A.; Service, R. J.; Yachandra, V. K.; Debus, R. J., Altered Structure of the Mn<sub>4</sub>Ca Cluster in the Oxygen-evolving Complex of Photosystem II by a Histidine Ligand Mutation. *J. Biol. Chem.* **2011**, *286*, 9257-9267.
15. Renger, G., Mechanism of light induced water splitting in Photosystem II of oxygen evolving photosynthetic organisms. *Biochim. Biophys. Acta. Bioenerg.* **2012**, *1817*, 1164-1176.
16. Ferreira, K. N.; Iverson, T. M.; Maghlaoui, K.; Barber, J.; Iwata, S., Architecture of the Photosynthetic Oxygen-Evolving Center. *Science* **2004**, *303*, 1831.
17. McCrory, C. C. L.; Jung, S.; Ferrer, I. M.; Chatman, S. M.; Peters, J. C.; Jaramillo, T. F., Benchmarking Hydrogen Evolving Reaction and Oxygen Evolving Reaction Electrocatalysts for Solar Water Splitting Devices. *J. Am. Chem. Soc.* **2015**, *137*, 4347-4357.
18. Rufo, C. M.; Moroz, Y. S.; Moroz, O. V.; Stöhr, J.; Smith, T. A.; Hu, X.; DeGrado, W. F.; Korendovych, I. V., Short peptides self-assemble to produce catalytic amyloids. *Nat. Chem.* **2014**, *6*, 303-309.
19. Najafpour, M. M.; Ghobadi, M. Z.; Sarvi, B.; Haghighi, B., An engineered polypeptide around nano-sized manganese–calcium oxide: copying plants for water oxidation. *Dalton Trans.* **2015**, *44*, 15271-15278.
20. Zhang, M.-T.; Chen, Z.; Kang, P.; Meyer, T. J., Electrocatalytic Water Oxidation with a Copper(II) Polypeptide Complex. *J. Am. Chem. Soc.* **2013**, *135*, 2048-2051.
21. Neves, M. M. P. S.; González-García, M. B.; Hernández-Santos, D.; Fanjul-Bolado, P., Screen-Printed Electrochemical 96-Well Plate: a High-Throughput Platform for Multiple Analytical Applications. *Electroanalysis* **2014**, *26*, 2764-2772.
22. Yamankurt, G.; Berns, E. J.; Xue, A.; Lee, A.; Bagheri, N.; Mrksich, M.; Mirkin, C. A., Exploration of the nanomedicine-design space with high-throughput screening and machine learning. *Nat. Biomed. Eng.* **2019**, *3*, 318-327.
23. Granda, J. M.; Donina, L.; Dragone, V.; Long, D.-L.; Cronin, L., Controlling an organic synthesis robot with machine learning to search for new reactivity. *Nature* **2018**, *559*, 377-381.